Metal Halide Perovskite Light-Emitting Materials and Devices

Chen Zou

A dissertation

submitted in partial fulfillment of the

requirements for the degree of

Doctor of Philosophy

University of Washington

2020

Reading Committee:

Lih Y. Lin, Chair

Mo Li

Arka Majumdar

Program Authorized to Offer Degree:

Electrical and Computer Engineering

University of Washington

Abstract

Metal Halide Perovskite Light-Emitting Materials and Devices

Chen Zou

Chair of the Supervisory Committee:
Professor Lih Y. Lin
Electrical and Computer Engineering

Metal halide perovskites were first rediscovered for photovoltaic applications in 2009. The performance of perovskite solar cells has undergone a rapid advancement with power conversion efficiency (PCE) increasing from 3.8% to over 25%, comparable to state-of-art commercial solar cells. Recent findings on excellent optoelectronic properties of perovskites like high photoluminescence quantum yield (PLQY), good charge transport and bandgap tunability motivate researchers to explore their applications in light-emitting devices such as light-emitting diodes (LEDs), multicolor displays and laser diodes. In this dissertation, I first introduce the development of perovskite LEDs (PeLEDs) and analyze key factors affecting the external quantum efficiency (EQE). The high refractive index of perovskites limits the light outcoupling efficiency to 20-25%. The next step to further increase EQEs should be focused on enhancing

light extraction. Through an optical simulation, I found the emitter dipole orientation plays an important role. This finding may provide guidance on further performance boost of PeLEDs. $CsPbI_3$ is the lowest bandgap all-inorganic perovskite, targeted for covering the red corner of CIE chromaticity diagram. However, $CsPbI_3$ bulk films transition to undesirable orthorhombic phase at room temperature. $CsPbI_3$ QDs are much more phase stable due to the reduced surface energy. Based on $CsPbI_3$ QDs, I demonstrate a stable red-emission PeLED. To push perovskite materials towards commercialized display applications, I developed a high-resolution photolithographic approach to pattern multicolor perovskite thin films. This approach is based on a dry lift-off process, addressing the incompatibility of perovskites to common polar solvents. Using this approach, we fabricated a multicolor pixel array for liquid crystal displays (LCDs) and a prototype perovskite mirco-LED display. Besides great potential in display applications, perovskites have renewed people's hope for achieving the long-standing goal of solution-processable electrically pumped laser diodes. I first demonstrate perovskite lasers integrated with distributed Bragg (DBR) and distributed feedback (DFB) cavities under optical pumping. Towards electrically pumped laser diodes, I suppressed the efficiency roll-off (droop) of perovskite LEDs by applying combined strategies. Finally, devices could be operated at high current densities up to 1 kA/cm^2. Future work will be integrating DFB cavities with perovskite LEDs to approach the ultimate goal.

TABLE OF CONTENTS

LIST OF FIGURES

LIST OF TABLES

ACKNOWLEDGEMENTS

When I came to University of Washington to start my PhD program in 2015, I have never thought about how I will go through my PhD life. It turns out I experienced a lot of things which I never expect. There are many people I would like to acknowledge, without their help and guidance, I couldn't imagine how I can complete my PhD study. Prof. Lih Lin is my supervisory, I would like to thank you for kind instructions and funding supports. I appreciate the relaxed atmosphere provided by your photonics group, so I can pursue research topics that I am most interested in. Prof. Lin not only gave me a lot of instruction and enlightenment on my research projects, but also introduced me to internship opportunities in industry. The experience in both academy and industry is of importance for me to decide my future career path. I would also like to thank our group members: Chun-Ying Huang, Congyang Zhang, Lin Wang, Mark Odendahl, Jingda Wu, Peifeng Jing, Ethan Keeler for their selfless helps. I obtained a lot of knowledge from discussion on my research with them.

I would also like to thank my collaborators for supporting my research. Without them, I can't complete many research challenges. Dr. Joey Luther host me as a vising student in NREL for six months in 2020. Although this research internship is interrupted by unexpected COVID-19, I learned a lot from your group on how to synthesize perovskite nanocrystals. Thank you for letting me experience research activities in a renowned national lab. Prof. Arka Majumdar's is very generous to share the measurement facilities in his group. I sincerely thank you and your group members for frequent discussion and help on mold fabrication, device mechanism and so on. I am also particularly appreciative of Professor Cody Schlenker, David Ginger, Lillo Pozzo, Karl

Böhringer and Mo Li. With their help and guidance, I have opportunities to learn multi-disciplinary knowledge and enrich my research data. At last, I want to appreciate all members in my dissertation committee, thank you for serving on my committee and your interests in my PhD research.

I feel very lucky and grateful that I could meet a lot of friends during my study at University of Washington. With them, I will not feel I am fighting alone. I would like to specially thank my friends Ruoming Peng, Changming Wu, Huan Li, Di Sun, Jiajiu Zheng and Yueyang Chen. They really helped me a lot not only in life but also in research. DUuring my first three years of PhD career, I didn't have much experience working in clean room, especially on electron-beam lithography. I learned a lot from them while working with them in UW WNF, without them, I couldn't pick up skills to fabricate nanodevices quickly.

Finally, I would like to thank University of Washington for providing excellent facilities. Part of my work was conducted at the Molecular Analysis Facility, a National Nanotechnology Coordinated Infrastructure site at the University of Washington; UW NNCI Washington Nanofabrication Facility (WNF), The largest public access fabrication center in the Pacific Northwest; Photonic Research Center (PRC), a multi-user shared research facility in Department of Chemistry; and Washington Clean Energy Testbed (WCET), operated by the Clean Energy Institute at the University of Washington.

Chapter 1. INTRODUCTION

1.1 MOTIVATION

Metal halide perovskite materials have emerged as a highly promising newcomer among semiconductor materials, first for photovoltaic applications.[1, 2] The perovskite family has a general formula of AMX_3, which was originally associated with $CaTiO_3$. The schematic crystal structure of perovskite material is shown in **Figure 1.1**. In metal halide perovskites, monovalent cations of primary interest at the A-site are methylammonium ($CH_3NH_3^+$, MA^+), formamidinium ($CH_5N_2^+$, FA^+) and cesium (Cs^+), divalent metal cations at the M site can be Pb^{2+}, Sn^{2+}, Ge^{2+}, Cu^{2+}, Eu^{2+}, Co^{2+} etc., and halide anion (I^-, Br^-, and Cl^-) are at the X-site. Unless specified, perovskites mentioned in this work refer to the category of metal halide perovskites. The AMX_3 hybrid perovskite structure is formed by a three-dimensional (3D) network, with the monovalent A-site cations occupying the cavity between four adjacent corner-sharing MX_6 metal halide octahedra.[3]

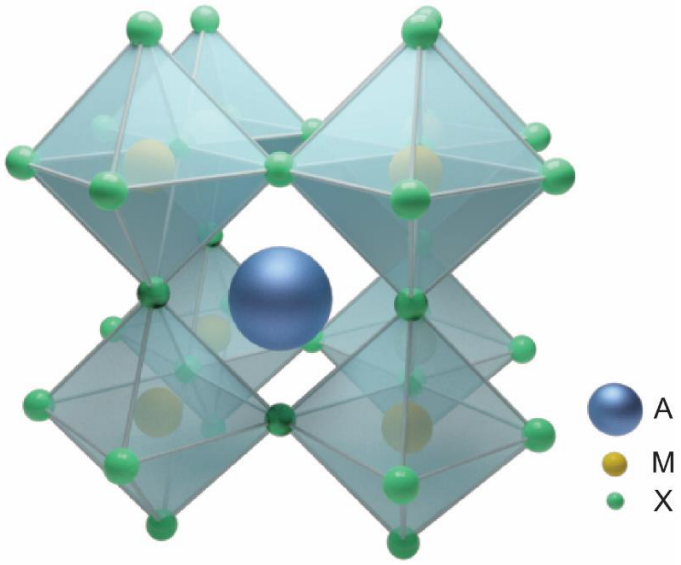

Figure 1.1. Schematic illustration of perovskite crystal structure. The blue, yellow, and green spheres represent the A-, M-, and X-site atoms, respectively.

These perovskite materials exhibit high carrier mobility, sharp optical absorption edges and high absorption coefficients comparable to GaAs, as well as unusual defect tolerance. These have led to record certified research solar cell power conversion efficiencies over 25%,[4] outdistancing that of the highest performing organic polymer solar cell and approaching that of Si solar cells. In addition, metal halide perovskites are also widely used in photodetection application covering a wide range of wavelength from ultraviolet (UV) to near infrared (NIR) wavelengths.

According to the detailed balance in the Shockley-Queisser limit formulation, an efficient solar cell material should also be a good light emitter. Indeed, in the past few years metal halide perovskite has emerged as a promising material for next-generation light-emitting applications.[5, 6] By appropriate defect passivation and quantum confinement, the photoluminescence quantum yields (PLQYs) of perovskite films have been approaching 100%.[7-10] Correspondingly, the performance of PeLEDs has gone through a rapid progress with EQE reaching over 20% for green and red PeLEDs, and over 10% for blue cousins. Besides efficient luminescence, hybrid perovskites also present excellent coherent light emission properties, which can be exploited in conventional lasing based on population inversion and low-threshold exciton-polariton lasing. A mass of short-pulse optically pumped perovskite lasers based on various resonant cavities have been demonstrated at room temperature in last several years.[11-16] Furthermore, continuous wave (CW) lasing of perovskites have also been achieved at low temperature, such rapid progress is very encouraging.[17-19] Very recently, several groups have reported CW lasing at room temperature, however, more evidence and analysis are still required to support these findings.[20-22]

Although these recent results show great promise of perovskite materials for light-emitting applications, perovskite laser diodes under electrical pumping has not been demonstrated, a requirement for photonic integrated circuits. Traditional lasers integrated on silicon platform use

inorganic semiconductors like GaAs and GaN, which requires expensive and high temperature fabrication procedures. In contrast, solution processed lasers are expected to reduce the cost and simplify the fabrication process. Therefore, solution processed electrically driven lasers have been pursued by a lot of researchers in last several decades. Leading contenders among solution-processed emitters include organic semiconductors, inorganic colloidal nanocrystals and now hybrid perovskites.[23] Achieving optically CW-pumped lasing is considered as a vital step towards electrically pumped lasing. However, it has never been achieved for the organic semiconductor family, presumably due to triplet accumulation that is difficult to avoid in organic semiconductors.[24] Colloidal nanocrystals only made this step recently, about two decades after initial investigations.[25-27] Nevertheless, further progress towards electrically pumped lasing is deemed to be highly challenging for colloidal nanocrystals because of their limited charge mobilities due to insulating ligands.

In view of the outstanding optoelectronic properties, perovskite materials open a new expectation to achieve this long-standing goal. At current stage, one key challenge is how to inject intense current (over several hundreds of A/cm^2) into perovskite layers with suppression of efficiency droop at such high current densities, aimed for enough exciton density for lasing. In addition, a major concern for these hybrid organic-inorganic perovskite materials is their poor stability upon exposure to moisture, thermal stress and ion migration, which presents another major barrier for lasers under electrical pumping. To achieve electrically driven perovskite laser diodes, a highly efficient LED structure and a well-designed resonant cavity are both required. This motivates us to optimize materials and structures of PeLEDs, and dedicatedly design optical cavities to achieve low-threshold optically pumped perovskite lasers. Finally, by integrating the optical cavity inside PeLEDs, we can target for an electrically driven perovskite laser device. In

this dissertation, I will introduce the progress we have made towards electrically pumped perovskite laser diodes.

1.2 VARIOUS TYPES OF PEROVSKITE EMITTERS

The simple preparation processability of metal halide perovskites facilitates their applications in a great variety of optoelectronic devices. Solution-processed methods, including drop-casting, spin-coating, inkjet-printing are widely used in producing perovskite films. Spin-coating, one of the cheapest film production approaches, is most commonly used in fabricating high-quality perovskite films. For solution-processed perovskites, there are polycrystalline bulk perovskites, Ruddlesden–Popper (RP) perovskites and perovskite quantum dots (QDs).

Hybrid perovskites are typically formed from the reaction between metal halide and organic halide, and then self-organized into 0D, 1D, 2D or 3D structure depending on the connection of metal halide octahedra.[28] For example, Perovskite QDs belongs to 0D structure and perovskite nanowires belongs to 1D structure. The reaction between a small organic molecule such as methylammonium iodide (CH_3NH_3I, MAI) and PbI_2 will result in 3D methylammonium lead iodide ($MAPbI_3$) perovskite where the PbI_6 octahedron connects three-dimensionally with each other by corner-sharing ($n = \infty$ phase in **Figure 1.2**). Replacing MAI with larger organic molecules, such as phenylethylammonium iodide ($C_8H_9NH_3I$, PEAI), interrupts the connection in one direction, forming a layered structure with inorganic and organic components stacking alternately and hence reducing the structural dimensionality ($n = 1$ in **Figure 1.2**). In this case, each inorganic octahedra layer is separated by two layers of organic moiety. They can be regarded as “bulk 2D” materials comprising of sheet-like inorganic blocks with 2D characteristics. When n exceeds 1, there are more than one inorganic octahedra layers between two organic moiety layers, such

structures are named quasi-2D perovskites. The generic chemical formula for these layered hybrid perovskites is $(PEA)_2MA_{n-1}Pb_nI_{3n+1}$, where n represents the number of octahedra layers within each quantum well. In addition, this type of perovskite possesses so-called RP phases and can be also named RP perovskites. When n is infinite, the incorporation of PEA can be neglected, and conventional 3D perovskites are formed.

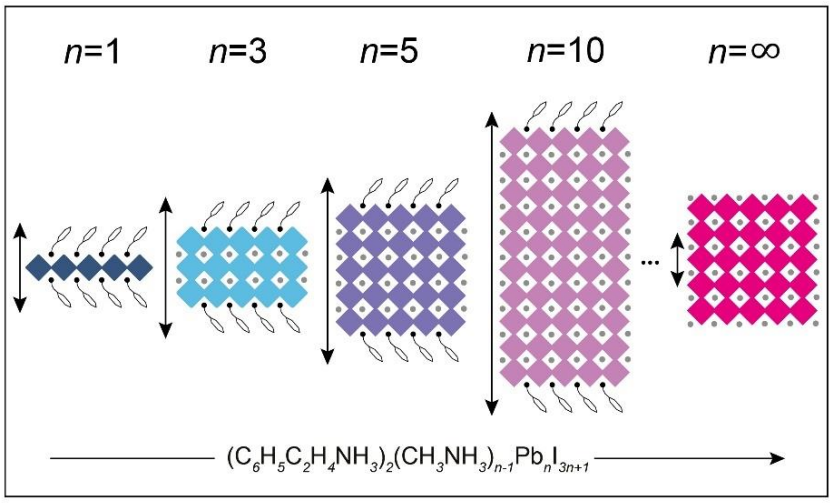

Figure 1.2. Representative crystal structure of RP perovskites. The figure is reprinted with permission from ref.6. Copyright 2016 Springer Nature.

1.2.1 *Polycrystalline bulk perovskites (3D perovskites)*

For polycrystalline bulk perovskites, organic (or cesium) halide and lead halide are mixed in DMSO, DMF or GBL solvent to form perovskite precursors. The precursors can be spin-coated onto substrates to form polycrystalline perovskite films. The polycrystalline 3D perovskite films are previously reported to have poor PLQY due to small exciton binding energy, free electrons and holes dominate recombination mechanisms. Free electron-hole pairs are beneficial for charge separation in solar cells, however, the situation become opposite in LEDs. In LED operation regime where the carrier density is typically less than 10^{15} cm^{-3}, non-radiative monomolecular

recombination because of trap states dominates in carrier decay dynamics, leading to non-radiative loss and low PLQY.[29] When 3D PeLEDs are first reported in 2014, their EQEs are less than 1%.[30] However, recent works have found methods to passivate the defects in 3D perovskites by a small amount of additives, which result in extremely high PLQYs approaching 100% and high EQEs over 20%.[8, 9, 31] In 3D perovskites where the free-carrier bimolecular recombination dominates in radiative processes, the PLQY (η_{3D}) can be described as the ratio of the radiative to total recombination rates.[32]

$$\eta_{3D} = \frac{k_2 n}{k_1 + k_2 n + k_3 n^2} \quad (1.1)$$

Where n is the carrier density. k_1 is trap-assisted monomolecular recombination rate, k_2 is the radiative bimolecular recombination rate and k_3 is Auger recombination rate. Through reducing k_1 value by defect passivation, the value of η_{3D} can be significantly improved. After overcoming the issue of poor PLQYs, currently, 3D perovskites become widely used in highly efficient PeLEDs.

1.2.2 *Ruddlesden–Popper (RP) perovskites (quasi-2D perovskites)*

In 2016, quasi-2D Ruddlesden–Popper (RP) perovskites were founded by Huang and Sargent's groups.[6, 33] Due to the smaller band gap (E_g) of the inorganic layers compared to that of the organic layers, quantum wells are formed in these layered perovskites with organic layers acting as barriers confining the inorganic wells. The combination of organic moieties with different sizes (e.g. PEA and butylammonium (BA)) allows further fine-tuning of the structure as well as the thickness of the quantum well in double octahedra stacking (n = 2), triple octahedra stacking (n = 3), and so on.

Different from 3D perovskites, the quasi-2D perovskites exhibit high PLQY due to exciton confinement provided by multiple quantum wells (MQWs) structures. The monomolecular

recombination in quasi-2D perovskites is 'excitonic' and radiative, totally different from non-radiative trap-assisted monomolecular recombination in 3D perovskites. PeLEDs based on quasi-2D perovskite have already achieved over 20% EQE.[10] This demonstrates the great advantage of quasi-2D perovskites in PeLEDs. However, quasi-2D perovskites are easily subjected to issues caused by Auger recombination. The quantum well structure also increases the number of localized carrier density, resulting in that Auger effect kicks in at a lower excitation density than 3D perovskites. Huang group have demonstrated that the QW widths could be tuned by various precursor stoichiometry, and they successfully enlarged the QW width to reduce Auger recombination.[34, 35] However, the intrinsic quantum confinement may restrict the effort and progress in suppressing Auger recombination.

1.2.3 *Perovskite quantum dots (0D perovskites)*

For perovskite QDs, they can be synthesized by hot injection method or ligand assisted reprecipitation (LARP). The hot injection method was first introduced for the synthesis of CdSe QDs and then applied to a variety of colloidal nanocrystals. By modifying this technique, colloidal perovskite QDs can be fabricated in a supersaturated solution through fast injection of the precursors at an elevated temperature.[36] Compared to complicated synthesis procedures of colloidal nanocrystals that require core/shell structures to present high PLQYs and dedicated control to achieve monodisperse nanocrystal size, the synthesis of perovskite quantum dots seems much easier. Perovskite QDs synthesized via hot inject methods show uniform nanocrystal size and high PLQYs approaching 100%.[7] The LARP method utilizes the different solubility of perovskite in polar solvents (e.g. DMSO and DMF) and non-polar solvents (e.g. chloroform and tolune).[37] A small amount of perovskite precursor in polar solvent is quickly injected into non-polar solvents with long-chain organic ligands. The nanocrystals immediately form upon injection,

the surrounding ligands protect nanocrystals from degradation and aggregation. The LARP method doesn't require high temperature, which is more cost-effective than hot injection method. However, the size and quality control of perovskite QDs through LARP method becomes more difficult. Nevertheless, a high EQE of 16.48% has been achieved for PeLEDs based on LARP-synthesized QDs.[38] Perovskite QD solution can also be spin-coated onto substrate, the thickness can be controlled by the solution concentration and spin-speed. However, different from bulk perovskite precursors, the perovskite QDs already show perovskite lattice structures in solution. Besides, it is feasible to spin coat perovskite QDs layer-by-layer to form the multilayer structure due to the non-polar solvent such as toluene, octane and chloroform used for dispersing QDs , which extends the maximum thickness of perovskite QD films can achieve.[39] In contrast, the layer-by-layer deposition is usually difficult for bulk perovskite films as the polar solvent in precursors such as DMOS, DMF and GBL can destroy underneath bulk perovskite films. Furthermore, heterojunction perovskite films can be obtained by spin-coating perovskite QD films with different compositions *via* layer-by-layer deposition. For example, utilizing the layer-by-layer deposition of perovskite QDs, Zhao *et al.* demonstrate solar cells with abrupt compositional variations throughout the perovskite film, which facilitates the charge separation at the internal interfaces.[40] The as-fabricated heterojunction perovskite QD solar cells achieve a record high PCE of 17.39% among all quantum dot solar cells.

Perovskite QDs have also been widely used in LED applications due to their high PLQY values. However, the electrical conductivity of QDs is usually poor due to the insulating ligands and interdot charge transport. This hinders the development of perovskite QDs, some recent works have relieved this problem by washing the ligands and doping metal ions to improve

conductivity.[38, 41] The EQEs over 6, 16 and 20% has been achieved for blue, green and red emission perovskite QD LEDs.[7, 38, 42]

1.2.4 *Besides solution-processed perovskites*

Besides solution-processed methods, perovskite films can be deposited through thermal vapor evaporation, chemical vapor deposition (CVD) and atom layer deposition (ALD).[43-45] For thermal vapor evaporation method, the perovskite films are deposited through the vapors of precursor chemicals under heating in a vacuum chamber. For examples, the $CsPbBr_3$ films can be deposited through heating CsBr and $PbBr_2$ sources, the corresponding vapors deposit onto substrates to form perovskite films. These two sources can be heated simultaneously (dual-source evaporation) or they can be deposited sequentially (single-source evaporation). Compared to solution processed perovskite films, vapor-deposited films show more uniform surface morphologies with more precise control of film thickness. They are more directly applicable to larger-scale and volume manufacturing. However, the PLQYs and absorption coefficients of vapor-deposited perovskite films are usually worse than solution-processed counterparts, hindering their various applications in solar cells and LEDs.

1.3 PEROVSKITE LIGHT-EMITTING DIODES

1.3.1 *Basic operating principles*

In LED technologies, semiconductors converts injected current to light. When a suitable voltage is applied, electrons and holes are injected from the cathode and anode, then recombine in the semiconductor emitter and release the energy in the form of photons. The color of the emission light is determined by the semiconductor bandgap, described by the equation

$$\lambda = \frac{hc}{E_g} \tag{1.2}$$

Where λ is the emission wavelength, h is the plank constant, c is the speed of light in vacuum space and E_g is the semiconductor bandgap. Due to the facile bandgap tunability of metal halide perovskites, various emission color ranging from UV to NIR can be achieved. White light emission can be achieved by combining three primary colors (red, green and blue) or a layer of light-emitting phosphor with blue backlight.

One important performance parameter in LEDs is the external quantum efficiency (EQE), which is defined as the ratio of the number of emitted photons (N_{photon}) to the number of injected charge carriers ($N_{electron}$). The EQE can be calculated *via*

$$\mathrm{EQE} = \frac{N_{photon}}{N_{electron}} = \frac{N_{photon}}{I/e} \tag{1.3}$$

Where I is the current flowing the LED device. The number of photons can be calculated by measuring the emission spectra and power, described by the following equation

$$N_{photon} = \frac{P \times \int_0^\infty \Phi(\lambda)\, d\lambda}{\int_0^\infty \Phi(\lambda) \times \frac{hc}{\lambda} \times R(\lambda)\, d\lambda} \tag{1.4}$$

Where P is the emitted power measured by a photodetector, $\Phi(\lambda)$ is the measured EL spectrum per nanometer. $R(\lambda)$ is the responsivity of the photodetector on each wavelength.

The PeLEDs can be assumed as Lambertian sources, which obeys the Lambertian cosine law: $I(\theta) = I_0 cos\theta$. Where θ is the angle between the direction of the emission light and the surface normal, $I(\theta)$ is the radiant intensity at the angle of θ and I_0 is the radiant intensity at $\theta = 0$. Then the luminance (L) can be calculated by:

$$L = \frac{683}{\pi} \times \frac{N_{photon} \int_0^\infty \Phi(\lambda) \times \frac{hc}{\lambda} \times V(\lambda)\, d\lambda}{A \int_0^\infty \Phi(\lambda)\, d\lambda} \tag{1.5}$$

Where $V(\lambda)$ is the luminous function representing the average spectral sensitivity of human visual perception of brightness, and A is the device area.

1.3.2 *Optimizing performance of PeLEDs*

There are two typical types of PeLED structures: non-inverted and inverted types (**Figure 1.3**). In general, the non-inverted type of PeLED structure is (from bottom to top): ITO/HTL/perovskite/ETL/metal, while the inverted type structure is: ITO /ETL /perovskite /HTL /metal. The HTL and ETL represents hole transport layer and electron transport layer. They also usually work as electron and hole-blocking layer to confine electron and hole pairs in perovskite layers to emit photons.

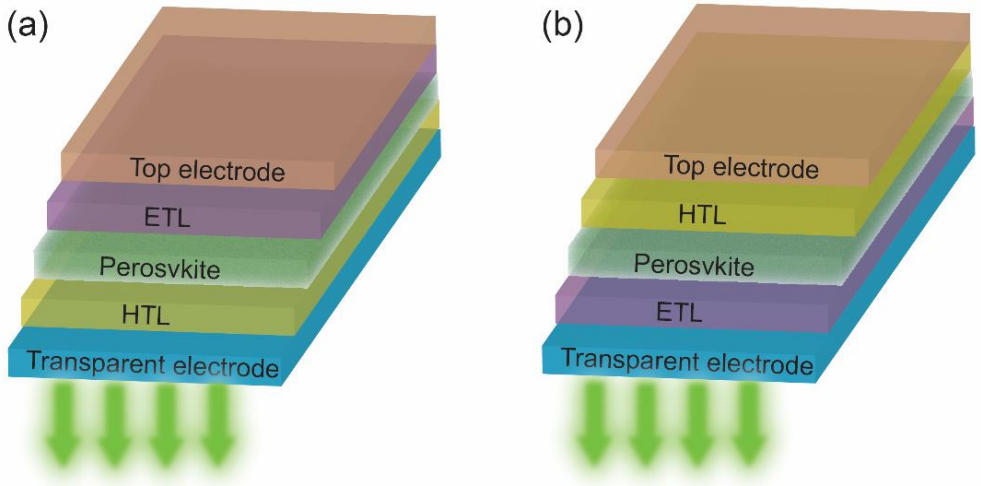

Figure 1.3. Schematic device structures of non-inverted and inverted type PeLEDs.

The development of EQEs of PeLEDs based on 3D perovskites, qusi-2D perovskites and 0D perovskite quantum dots is shown in **Figure 1.4**. It is apparent that the EQEs of all kinds of PeLEDs increase dramatically in last several years. This rapid increase is much faster than that of conventional organic LEDs (OLEDs), which may be a result of many efforts on understanding the

physics of light emission of perovskites and developing fabrication techniques to obtain high-quality perovskite films. The development of blue LEDs falls behind green and red counterparts due to relatively poor PLQY of blue perovskite emitter and inefficient hole injection because of deep valence band. It is interesting to see the EQEs of 3D PeLEDs have been significantly improved, after researchers boosting the PLQYs of 3D perovskites by defect passivation.

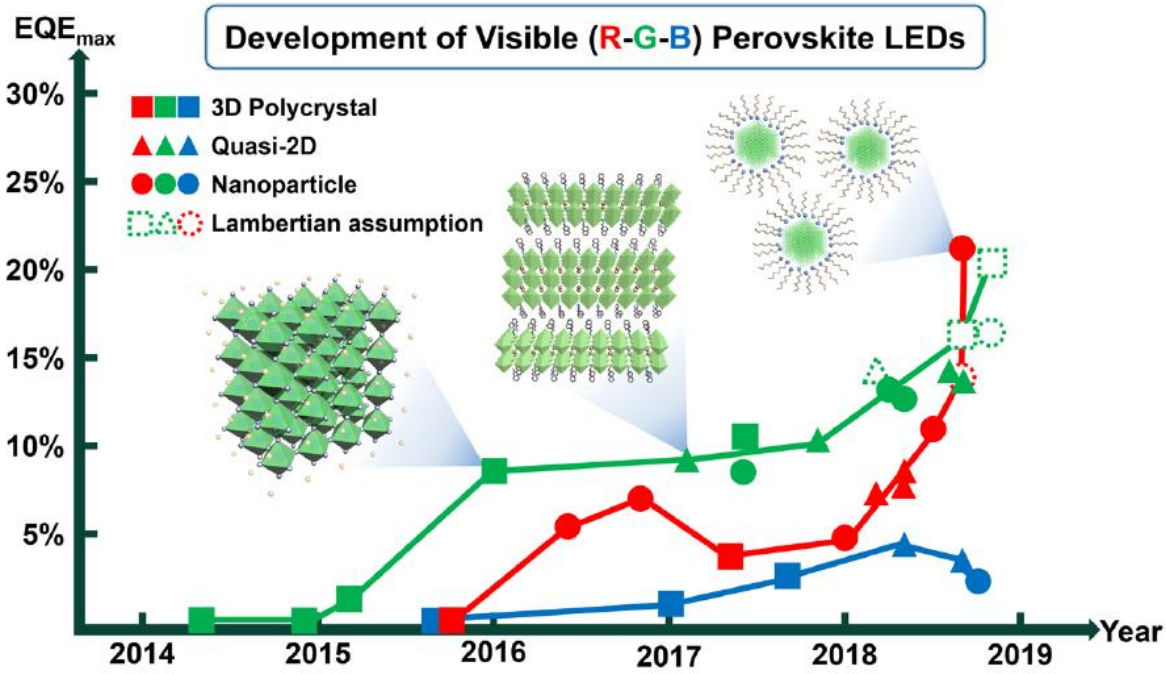

Figure 1.4. EQE developments depending on the dimension of metal halide perovskites. Reproduced with permission from ref.46. Copyright 2019 American Chemical Society.

Like other LED categories such as OLEDs and quantum dot LEDs (QLEDs). The EQE of PeLEDs mainly depends on the PLQY of perovskite films, the charge injection balance and light outcoupling efficiency as described by the following equation

$$EQE = \eta_{out} IQE = \eta_{out} \gamma_{bal} \gamma_{e-h} \eta_{S/T} q_{eff} \quad (1.6)$$

Where η_{out} is the light outcoupling efficiency and IQE is the internal quantum efficiency, which is the product of charge injection balance (γ_{bal}), the probability of forming a correlated

electron–hole pair or exciton from each pair of injected carriers ($\gamma_{e\text{-}h}$), singlet/triplet capture ratio ($\eta_{S/T}$) and effective radiative quantum yield (q_{eff}). Generally, the $\eta_{S/T}$ is close to unity for perovskite films, thus we can usually neglect this item in the equation. Based on equation (1.6), we suggest some guidelines on achieving a high-efficiency PeLED as shown in **Figure 1.5**. (i). Charge injection should be balanced, the ratio of the number of electrons to holes should be close to unity (maximize γ_{bal}). (ii). Perovskite films should have good surface coverage with negligible pin holes (maximize $\gamma_{e\text{-}h}$). Otherwise, the shunt path could be formed, and charge carriers could directly pass through the emitter to electrodes with recombination. (iii). Nonradiative recombination loss should be minimized to increase the PLQY of films (maximize q_{eff}). (iv) Light extraction management is important in boosting PeLED efficiencies. The proportion of outcoupled light from PeLEDs to air (η_{out}) should be maximized.

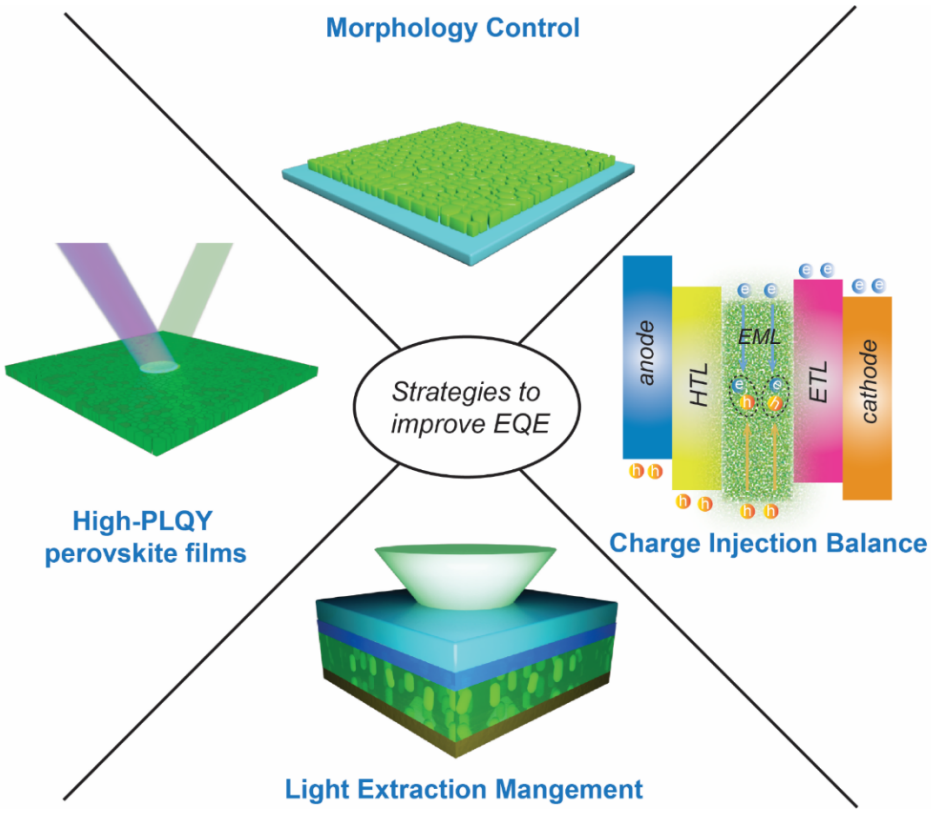

Figure 1.5. Promising strategies to improve device efficiency of PeLEDs.

The intrinsic quantum yield (q) of perovskite films is mostly determined by the ratio of radiative to total recombination processes, which can be described as

$$q = \frac{k_r}{k_{nr} + k_r} \tag{1.7}$$

Where k_r is the radiative decay rate and k_{nr} is the non-radiative decay rate. Therefore, reducing k_{nr} and increasing k_r is of help to improve q. Indeed, many strategies have been demonstrated effective on improving the intrinsic radiative quantum yield such as defect passivation, exciton confinement etc. Xu *et al.* minimized the non-radiative losses through the rational design of passivating molecules. As a result, a record high efficiency of 21.6% was achieved among PeLEDs without outcoupling structures.[47] Jalebi *et al.* maximized the luminesce from halide perovskites by potassium passivation. The external PLQY was improved to 66%, corresponding to a high internal PLQY of 95%.[8] Quasi-2D perovskites have also shown high PLQYs due to the exciton confinement from MQW structures. High performance LEDs based on quasi-2D perovskites have been demonstrated. The effective radiative quantum yield (q_{eff}) is closely connected to the intrinsic quantum yield (q) of perovskite films, the relationship between them can be expressed as

$$\frac{q_{eff}}{q} = \frac{F}{qF + 1 - q} \tag{1.8}$$

Where F is the Purcell factor that describes how the cavity affects the dipole power generated inside the perovskite layer. Therefore, increasing the Purcell factor is also an effective method to increase the effective quantum yield, thus the EQE of PeLEDs. However, this usually requires a design of photonic nanostructures like photonic crystals, which may be cost effective.

The surface morphology of perovskite films is highly dependent on the surface properties of underlying layers. Perovskite precursors have a poor wetting capacity on most of organic HTLs due to their hydrophobic surfaces, leading to a smaller number of nucleation sites and thus discontinuous crystal grain distribution. Polymers with hydrophilic surfaces like PVP, PFN, PEI

and betaine were successfully utilized as the interlayer to improve surface morphology of perovskite films and device efficiency of PeLEDs.[48-51] For example, the amphiphilic conjugated polymer PFN was used to convert the surface of the HTL from hydrophobic to hydrophilic, and a high-quality perovskite film with a uniform surface was obtained. This helped fabricate a highly efficient PeLED with a peak EQE of 14.4%.[49]

The charge injection balance can be well-adjusted by choosing proper transport layers and tuning their thicknesses. The electron usually dominate injection in PeLEDs, Lin *et al.* inserted a thin PMMA layer (5 nm) in ETL to slow down the electron transport and balance electron and hole injection.[52] As a result, a high EQE of 20.3% was achieved for that green-emission PeLED.

Besides charge injection balance and effective quantum yield, the light outcoupling efficiency is also a large factor affecting the EQE. Therefore, studying the limits of light outcoupling is of great significance to achieve a highly efficient PeLED. From our optical simulation of power distribution in PeLEDs, we found the outcoupling efficiency is limited to 20-25% (**Figure 1.6**). Around 75%-80% of generated light from perovskite layers is trapped in devices without emssion in air, due to the high refractive index of perovskite materials ($n \approx$ 2.2-2.6). The state-of-art PeLEDs have achieved EQEs over 20%, approaching the theoretical limitation determined by light outcoupling. More efforts should be delved into device structure optimization to increase the light outcoupling efficiency. Cao *et.al* demonstrated efficient and high brighness PeLEDs based on the perovskite films that spontaneously form the submircometer-scale structures. They claimed these structures could be of help to extract light out from the devices.[53] Shen *et al.* ultilized bioinspired moth-eye nanostructures in the ZnO layer to extract waveguided light from PeLEDs, achieveing a record high efficiency of 28.2% at that time.[54] In fact, there are already some outcoupling techniques successfully applied in OLEDs and QLEDs, which includes optimizing device layer

thickness and refractive index, adjusting emitter diople orientation and intergrating photonic structures to LEDs (microlens array, diffraction gratings, low-index grids, buckling patterns). These technqiues should be aslo of help to improve the light outcoupling efficiency of PeLEDs.

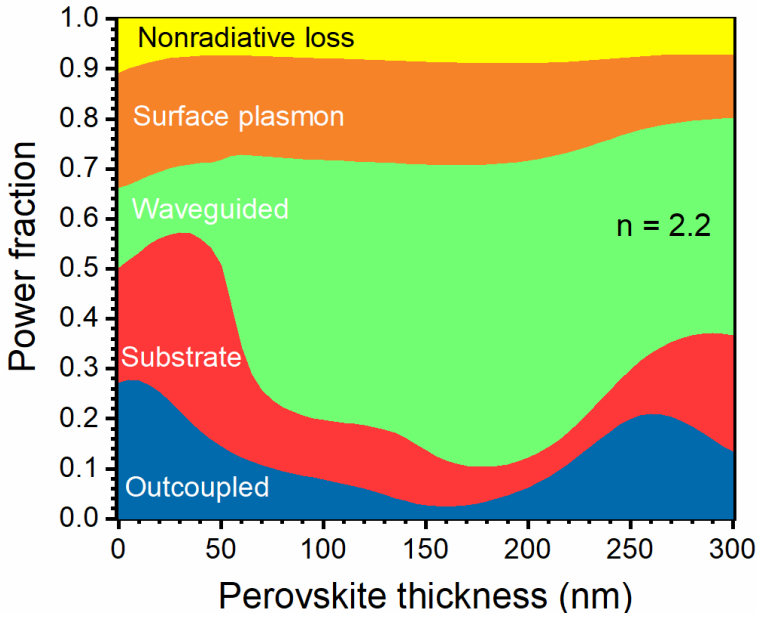

Figure 1.6. Power distribution into different optical modes of $CsPbBr_3$ LEDs with various perovskite layer thicknesses. The refractive index (n) of the $CsPbBr_3$ films is ≈ 2.2 near emission wavelength. The LED structure is ITO/PEDOT:PSS/Poly-TPD/perovskite/TPBI/LiF/Al.

1.3.3 *Operational stability*

Although PeLEDs have achieved comparable efficiencies to state-of art OLEDs and QLEDs after going through a rapid development in last several years, studies on operational stability lag behind. To commercialize PeLEDs, they must come out of the aging problem. Previous studies have shown perovskites are degraded by surrounding environment including moisture, oxygen, temperature and UV light.[55, 56] Ambient moisture has been long reported to play an import role in the degradation of perovskite films. For example, an optically brown $MAPbI_3$ film decompose to a

yellow PbI_2 film out of a glovebox. And the sufficient oxygen and intense UV light may facilitate this decomposition.

Apart from decomposition, moisture may also lead to the hydration for some types of perovskite films probably in the absence of sufficient oxygen or UV illumination.[57] Interestingly, the phase transition in this case can be reversible as shown in **Figure 1.7**. The pristine $CsPbIBr_2$ film with orange-red color became transparent after moisture exposure, but then reversed back to original color after being heated at 160 ℃ in a nitrogen-filled glove box.[43] However, this process is still undesirable in device fabrication and tests as sometimes heating is not compatible nor practical for some devices. In addition, the non-perovskite phase films show little absorption of light and dark photoluminescence. The crystal morphologies of films in perovskite (PVSK) phase and degraded non-PVSK phase are totally different.

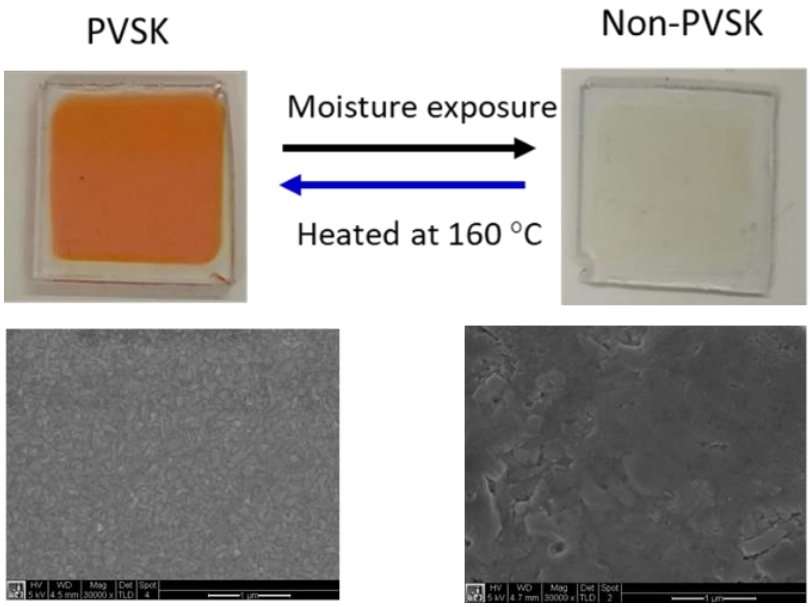

Figure 1.7. $CsPbIBr_2$ films in perovskite (PVSK) and non-PVSK phases.

Although ambient environment is a big factor affecting the stability of perovskite films, it is fortunate that appropriate encapsulation is able to address this problem to a great extent in PeLEDs.

The UV epoxy could be dropped onto the top metal layer and sealed with a thin glass side. The devices were then placed under UV lamb for 10 minutes to harden epoxy. We found the encapsulated devices placed in ambient condition for 2 weeks still keep similar performance to fresh devices, demonstrating the protection from moisture and oxygen can help increase the environment stability for PeLEDs. However, different from environmental stability, the operational stability describes the luminance evolution of PeLEDs under continuous operation. To quantify the operational stability, T_{50} lifetime is defined as the time it takes for the luminance to decrease to half of its original value. We measured the T_{50} lifetime by setting the initial luminance as 100 cd/m^2 under constant driving current. The brightness of common display screens in cellphones and computers is 100-400 cd/m^2. We measured the T_{50} values for our quasi-2D and 3D perovskite LEDs to be 0.8 and 3 hours respectively, which is much shorter than the environment lifetime. The factors affecting operational stability is still controversial, but ion migration has been regarded as the major degradation mechanism in PeLEDs by many researchers in perovskite community. It is not unusual to see a perovskite LED degrades to half of the initial efficiency within hours or even minutes due to ion migration under an applied electric field.[58] The cations and halides ions can move across the LED device layer stack between two electrodes under applied electric field, resulting in defect migration, modification on charge injection and the distortion of the perovskite crystal lattice. There are some potential ways to suppress ion migration and improve operational stability of perovskite materials. For example, immobilizing cations and anions of perovskites with fluorides has been demonstrated to be of help to improve the operation stability in solar cells.[59] Passivating defects in perovskite thin films should also help reduce ion migration and improve stability. Furthermore, depositing a permeable polymer or Al_2O_3 on the bottom and top of perovskite may play a significant role in reducing ion migrations.

1.4 OPTICALLY AND ELECTRICALLY PUMPED PEROVSKITE LASER DIODES

Photonic integrated circuits with miniature component sizes and high integration density have been regarded as the technology that can potentially provide breakthrough advancement in modern computing and communication systems, as it aims to achieve an optical analogy of VLSI that can overcome several bottleneck that electronic technologies encounter such as speed, bandwidth, and power consumption.

Key components in photonic integrated circuits include lasers, waveguides, modulators, and photodetectors that can be lithographically defined and fabricated on low-cost Si platforms to achieve ultimate system compatibilities. Among these, lasers have been the most challenging to integrate with Si due to the incompatible fabrication processes between laser gain materials and Si. Compared to traditional semiconductor lasers, solution processed hybrid perovskite lasers are expected to reduce the cost and simplify the fabrication process.

1.4.1 *Basic operating principles*

The action of lasing usually requires the population inversion to activate the stimulated emission and resonant cavities. We describe five ways in which energy conversion can occur in a two-level system in the following. Level 1 is the low-energy state and level 2 is the high-energy state.

(a) Absorption of photons from the pump: The atom is raised from level 1 to level 2. In other words, an electron in the atom jumps from an inner orbit to an outer orbit.

(b) Spontaneous emission of a photon of energy close to the energy bandgap: The atom jumps down from level 2 to the lower level 1. The process occurs “spontaneously” without any external influence.

(c) Stimulated emission: this process requires the population inversion, that is to say, the number of atoms at higher energy level should be higher than that at lower energy level. The atom

jumps down from energy level 2 to the lower level 1, and the emitted photon of energy is an exact replica of a photon already present. The process is induced, or stimulated, by the incident photon.

(d) Absorption of a photon of energy close to the bandgap: The atom jumps up from level 1 to the higher level 2. As in (c), the process is induced by an incident photon.

(e) Nonradiative deexcitation: The atom jumps down from level 2 to the lower level 1, but no photon is emitted so the energy must appear in some other form, like trap-assisted recombination, Auger recombination to release phonons.

To meet the requirement for lasing, the optical gain from stimulated emission should exceed the loss from absorption, nonradiative deexcitation, cavity leakage. The perovskite materials can achieve population inversion and stimulated emission under pulsed laser pumping condition at room temperature and under CW laser pumping condition at cryostat temperature. The temperature rise and Auger recombination loss during longer pulse pumping hinder the achievement of optically pumped CW perovskite laser diodes at room temperature.

1.4.2 *Resonant cavities*

The resonant cavities need to be well-designed to allow the light circulates inside the cavity with minimized cavity transmission and loss. There are several commonly used cavities in perovskite laser diodes.

(1) Fabry-Perot (FP) and whispering-gallery-mode (WGM) cavity

The FP cavity can be simply made by two high reflective end-facets, such as perovskite nanowires. The lasing wavelength is determined by $\lambda = \frac{2nL}{m}$, where n is the refractive index of the gain medium, L is the cavity length and m is the mode number (integer). The finesse F (or quality factor) is a measure of the sharpness of resonant modes.

$$F = \frac{\pi\sqrt{R}}{1-R} \tag{1.9}$$

Where R is the intensity reflection coefficient of two mirrors. The free spectral range (FSR) of two adjacent resonant modes is

$$\Delta v_{FSR} = \frac{c}{2nL} \tag{1.10}$$

The bandwidth of a peak is determined by

$$\Delta v_{FWHM} = \frac{\Delta v_{FSR}}{F} = \frac{c}{2nLF} \tag{1.11}$$

For FP cavity, the optical gain of the medium need to meet the following criteria for lasing.

$$e^{2(g-\alpha)L} > \frac{1}{R^2} \tag{1.12}$$

Where α is the loss per length inside the cavity. The FP cavities exhibit efficiently directional laser, which is a big advantage in integrating with other optical components for on-chip photonic circuits.

WGMs are specific resonances of a wave field that are confined inside a given resonator with smooth edges due to continuous total internal reflections. Perovskite microdisks and microcubes can form the intrinsic WGM cavity, where edge surfaces can act as reflectors. The WGM cavity can have a very high quality factor ($Q \sim 10^8$), however, the rough perovskite films scatter the traveling light, limiting the Q to 10^3-10^4. In addition, the output from the WGM cavity is usually unidirectional with emissions all around edge surfaces, which is not favorable for integrating with other optical components in an optical platform. However, the ring resonator structure composed of a bus waveguide and a WGM cavity can address this problem and produce directional output.[60] The perovskite nanostructures including 1D nanowires, 2D microdisks and 3D microspheres can be synthesized by liquid-phase self-assembly, liquid-solid interface growth and vapor-phase growth methods.[61-69] While versatile perovskite lasers have been reported with these intrinsic

cavities, the geometry of these self-assembled perovskite nanostructures couldn't be precisely controlled, which may hinder practical applications.

Besides these self-assembled perovskite nanostructures, hybrid perovskites can be processed to various cavity geometries by microfabrication technologies due to their structural softness.[70] Template-confined solution-growth method has been proposed by Fu group.[71-73] They used the PDMS template with patterned structures to confine the perovskite crystal growth during the slow evaporation of the solution under heating. Based on this approach, perovskite nanowires, microdisks and microring arrays with controlled geometries were successfully fabricated. Zhizhchenko *et al.* developed a laser ablation approach to fabricate perovskite microdisks with diameter ranging from 2 to 9 μm.[74] This method allowed them fabricate perovskite WGM microlasers with *Q* up to 5500. Top-down lithography is a standard process in manufacturing and thus crucial for the development of on-chip integrated photonics, Wang et al. patterned perovskite single crystal into a high-Q microdisk cavity with a bus waveguide by electron-beam lithography and inductively coupled plasma etching.[75]

(2) Distributed Brag Reflectors (DBR)

The working mechanisms of DBR and FP cavities are similar. The DBR consists of alternative low and high refractive index layers. For example, SiO_2 (n = 1.5) and TiO_2 (n = 2.5) are commonly used in DBR structures, the thickness of each layer is determined by $\lambda/4n$ (λ is the desirable lasing wavelength). In generally, The DBR consisting of 10 pairs of SiO_2/TiO_2 layers can achieve a high reflection over 95%. The gain medium is sandwich between two DBRs to form the vertical cavity surface emitting laser (VCSEL) structure (**Figure 1.8a**). The advantage of DBR structure is that it can be designed to possess a high reflection at a specific range of wavelength but a low reflection

at another wavelength range (**Figure 1.8b**). Therefore, the pump light with shorter wavelength can transmit through the DBR, but the generated light from gain medium will be reflected by DBRs and circulate inside the cavity.

Various perovskite lasers based on DBR cavities have been established since 2014, for example. In 2014, Deschler *et al.* demonstrated the operation of an optically pumped VCSEL based on hybrid perovskites for the first time.[76] Three narrow peaks can be observed in their work when the device was optically pumped. Chen *et al.* embedded a high quality $MAPbI_3$ thin film between two gallium nitride (GaN) DBR mirrors and achieved a single-mode lasing with a low threshold (~7.6 μJ/cm^2) and a high *Q* (~1100) under 340 ps pulse pumping.[77] The number of lasing peaks in a VCSEL is determined by the overlap between cavity-supported resonance modes and the spectral region of optical gain. Therefore, a single-mode lasing often demands a relatively short cavity length.

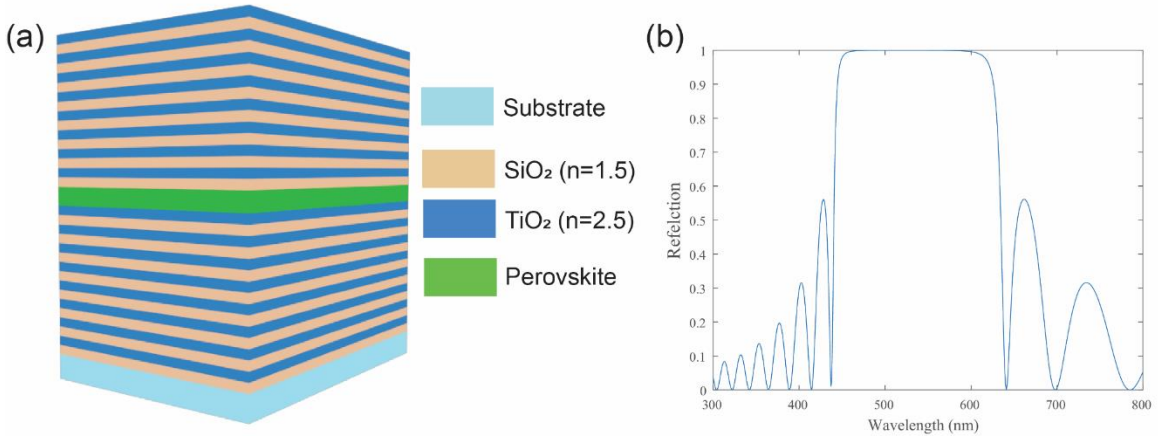

Figure 1.8. Perovskite VCSEL structure. (a) Schematic device structure of a perovskite VCSEL with bottom and top DBRs. (b) Simulated reflection spectrum of a DBR composed of 10 pairs of SiO_2/TiO_2.

(3) Distributed feedback (DFB) cavity

It is likely that many of us have known the color selection of a CD ROM if it is observed at different angles. The DFB structure is a periodic grating. The grating period determines the resonant wavelength. The duty cycle and depth of grating affect the quality factor of the resonant peak. The SEM image of a grating with a period of 280 nm is shown in **Figure 1.9(a)**. **Figure 1.9(b)** shows the FDTD simulation of light power distribution in a structure where a perovskite layer is on top of a periodic grating at resonant wavelength. The standing wave is achieved in the horizontal direction and only a small fraction of power emits from the top, leading to a well-designed resonant cavity. The resonant wavelength of a DFB cavity needs to satisfy the Brag condition

$$m\lambda = 2n_{eff}\Lambda \tag{1.13}$$

Where n_{eff} is the effective refractive index of the integrated structure. Λ is the grating period. m determines the order of diffraction. m = 1 represents the first order grating, where light resonates in the grating surface direction and emits from the edge. In a second order grating, the light radiates normal to the grating surface. As the second order gratings have larger dimensions compared to first order ones, they are often easier to fabricate by lithography and thus are preferred by researchers in perovskite community for a first demonstration of lasing operation.

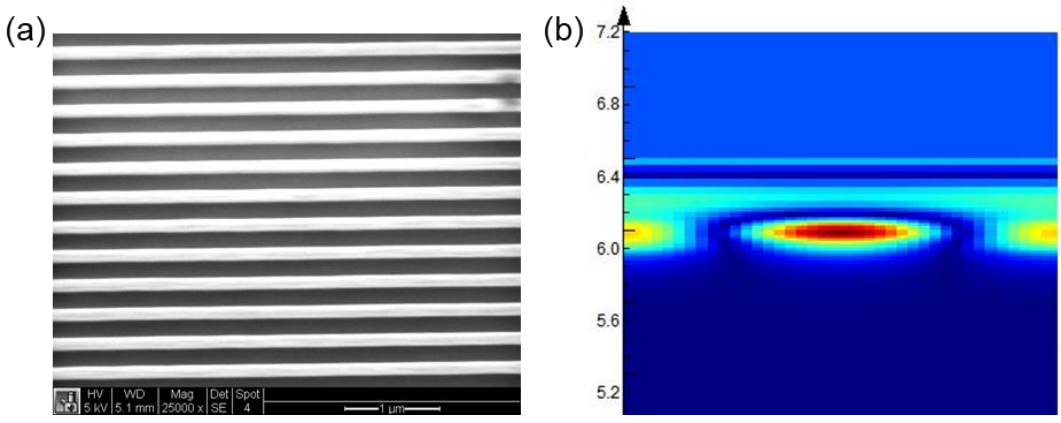

Figure 1.9. 2nd order DFB structure. (a) Planar SEM image of a second-order DFB grating (Λ = 280 nm). (b) Electric field distribution inside one grating period.

DFB cavities have been widely used in commercial standard lasers due to great robustness. Among perovskite lasers, DFB cavities have also been widely adopted and show remarkable performance. Jia *et al.* demonstrated CW-pumped perovskite lasing at low temperature utilizing the DFB structure in 2017.[19] They spun cast a $MAPbI_3$ film onto a 2nd-order Al_2O_3 grating on a sapphire substrate and cooled the device down to around 100 K. When temperature is cooled down to below about 160 K, the lattice structure of $MAPbI_3$ changes from tetragonal to orthorhombic, with the latter having a slightly larger optical bandgap. The mixed-phase system, where tetragonal-phase inclusions formed inside the bulk orthorhombic host matrix within a few 100 ns upon intense optical excitation (presumably due to local heating), can avoid lasing death phenomenon and account for continuous gain demonstrated in that work. Besides 1D Bragg grating, a 2D PC based perovskite laser has been demonstrated by Chen *et al.* with a high power-conversion efficiency of 13.8±0.8%. The single-mode lasing wavelength could be tuned by the PC pitch range.[78] Thermal nanoimprint techniques have also been introduced to directly emboss photonic nanostructures into perovskite films. Pourdavoud *et al.* created 1D diffraction grating and 2D PC resonator directly into $MAPbI_3$ films, and achieved low threshold lasing at room temperature with narrow linewidth.[79, 80] Interesting, they found pressed perovskite films show decreased roughness (0.5 nm rms) compared to those (23.8 nm rms) of pristine films, which led to reduced ASE threshold.[80]

1.4.3 *Electrically pumped perovskite laser diodes*

Perovskite materials open up new perspectives for solution-processed laser diodes. Towards this long-standing goal, we have to figure out the lasing threshold under electrical pumping, e.g. how much current density we need to inject into devices. We estimate the exciton density (n_{exciton}) generated in the carrier recombination zone by the following equation[81]

$$n_{exciton} = \frac{J}{e} \times EQE \times \frac{1}{\eta_{out}} \times \frac{1}{\eta_{PL}} \times \frac{1}{L_{exciton}} \times \tau_{exciton} \quad (1.14)$$

Where e is the electron elementary charge, η_{out} is the light out-coupling efficiency, η_{PL} is the internal PLQY, and $L_{exciton}$ is the width of the carrier recombination zone. In the calculation, we use η_{out} = 20% as this is typical light outcoupling efficiency in PeLEDs and $L_{exciton}$ = 40 nm. The $L_{exciton}$ is overestimated here as it should be smaller than the perovskite layer thickness, which may lead to overestimation of $J \times EQE$ required for lasing. η_{PL} is calculated by the following equation

$$\eta_{PL} = \frac{k_2 n}{k_1 + k_2 n + k_3 n^2} \quad (1.15)$$

Where k_1, k_2 and k_3 are fitted recombination coefficients for KBr-treated 3D perovskites, n is the carrier density and it is the same as $n_{exciton}$ in this case.

The ASE threshold (E_{th}) is converted into exciton density (n_{ASE}) using the following equation

$$n_{ASE}(cm^{-3}) = E_{th}\left(\frac{\mu J}{cm^2}\right) \times \frac{\lambda_{excitation}}{hc} \times \frac{1}{d(cm)} \times a \quad (1.16)$$

Where $\lambda_{excitation}$ is the wavelength of the excitation pulse laser, h is the plank constant, c is the light speed, d is the thickness of the perovskite film and a is the absorption of films. In this calculation, we use E_{th} = 15 μJ/cm^2, $\lambda_{excitation}$ = 365 nm, d = 100 nm and a = 0.3.

Combining equation (1.14) and (1.16), we can obtain the relationship between the required threshold of $J \times EQE$ and optically pumped ASE threshold.

$$J \times EQE = E_{th} \times e \times \frac{\lambda_{excitation}}{hc} \times \frac{1}{d(cm)} \times \frac{1}{\tau_{exciton}} \times a \times \eta_{out} \times \eta_{PL} \times L_{exciton} \quad (1.17)$$

The relationship between luminance (L) and $J \times EQE$ can be calculated by the following equation

$$L = \frac{J}{e} \times EQE \times \frac{683}{\pi} \times \int_0^\infty \Phi(\lambda) \times \frac{hc}{\lambda} \times V(\lambda)\, d\lambda \quad (1.18)$$

Where λ is the emission wavelength, $V(\lambda)$ is the luminous function representing the average spectral sensitivity of human visual perception of brightness, and $\Phi(\lambda)$ is the normalized EL spectrum per nanometer. After calculation, luminance (L) is proportional to $J \times EQE$ as

$$L\ (cd/m^2) = 3.67\ \times 10^6\ \times (J \times EQE)(A/cm^2) \quad (1.19)$$

For the ASE threshold of 15 μJ/cm^2, a $J \times EQE$ of 95 A/cm^2 and luminance of 350 Mcd/m^2 are needed. An electrically driven perovskite laser device should integrate a well-designed resonant cavity with a highly efficient LED structure. The resonant cavity with high Q can reduce the required lasing threshold. Optimizing the properties of perovskite materials and engineering LED structure could increase the value of $J \times EQE$. Both approaches should be pursued to finally achieve lasing under electrical pumping for perovskite laser diodes. In the last several years, the demonstrated perovskite-based lasers can be divided into two categories, one is conventional lasing based on population inversion, the other one is low-threshold exciton-polariton lasing. The polariton lasing doesn't require population inversion, which may be a potential direction for achieving electrically pumped lasing. Recently, Evans *et al.* reported CW polariton lasing in $CsPbBr_3$ NWs under a low lasing threshold of ≈ 6 kW/cm^2 at 77 K.[17] A high Rabi splitting energy of 200 ± 12 meV was observed in $CsPbBr_3$ NWs, indicating that strong light-matter interaction is intrinsic to this class of materials. However, it may be difficult to integrate perovskite nanowire in the LED device stack.

Tian *et al.* demonstrated CW lasing in a $MAPbBr_3$ single crystal VCSEL at room temperature. The authors suggested the polariton lasing may occur in the strongly confined optical cavity, which accounts for the ultralow threshold of CW lasing (34 mW/cm^2).[22] Although the authors observed a large Rabi splitting energy of 372 meV at room temperature, further supports for polariton lasing in this work are in investigation. Nevertheless, it shows the great promise that one can achieve electrically driven polariton lasing based on the high-quality perovskite single crystal and VCSEL structure. Perovskite single crystals have very low defect densities, smooth outer surfaces and high carrier mobilities, which are very suitable for lasing applications. However, LEDs based on

perovskite single crystals have been rarely reported, more studies in this field are required to explore the potential of perovskite single crystals for electrically pumped lasing applications.

1.5 SCOPE OF THIS WORK

This dissertation consists of 7 chapters. In this first chapter, I aim to explain the motivation why we are using metal halide perovskites as solution processed emitters for various light-emitting applications including LEDs and lasers. I also introduce the basic working mechanisms and research progress of these devices. In Chapter 2, I show the importance of light extraction management in improving device efficiency of PeLEDs, which is currently a hot topic after the development of perovskite materials has reached into a relatively mature stage. In Chapter 3, I demonstrate a red-emission PeLED with enhanced operational stability based on a perovskite QD emitter. The surface tension brought by the QD structure can keep perovskites in the desired cubic phase. In Chapter 4, I develop a high-resolution photolithographic approach to pattern multicolor perovskite thin films. This approach can be further applied in applications of perovskite liquid crystal displays (LCDs) and perovskite micro-LED arrays. In Chapter 5, I demonstrate optically pumped perovskite lasers with external optical cavities such as DBR and DFB. In Chapter 6, I introduce my progress towards electrically driven perovskite lasers. The efficiency roll-off (droop) is significantly suppressed after applying combined strategies including balancing charge injection, suppressing auger recombination, and reducing Joule heat. In the last chapter, I summarize this dissertation work, analyze the existing challenges, and propose future research directions.

Chapter 2. OPTICAL SIMULATION OF POWER DISTRIBUTION IN PELEDS

Manuscript submitted for publication:
Zou C, Lin L. Y. Effect of emitter orientation on outcoupling efficiency of perovskite light-emitting diodes.

2.1 ABSTRACT

Metal halide perovskites have emerged recently as promising candidates for next-generation light emitting diodes (LEDs) and display applications. The device performance of perovskite LEDs (PeLEDs) has experienced a rapid advancement in last several years with the external quantum efficiencies (EQEs) reaching over 20%, comparable to the state-of-art organic LEDs (OLEDs) and quantum dot LEDs (QLEDs). The photoluminescence quantum yields of perovskite films have also been approaching 100%. Therefore, the next step to improve the EQE of PeLEDs should be focused on boosting light extraction. In this work, we show the emitter dipole orientation as a key parameter in determining the outcoupling efficiency of PeLEDs. Horizontally oriented dipoles are preferred over vertically oriented dipoles in terms of improving light extraction. To experimentally determine the dipole orientation of perovskite films, we carried out angular p-polarized photoluminescence (PL) measurements. The results show that all-inorganic $CsPbBr_3$ films have a preferred vertical dipole orientation, which is not favorable to light extraction. By tuning the refractive index, thickness and dipole orientation of perovskite layers, we believe there is still much room for improving the outcoupling efficiency, thus the EQE of PeLEDs.

2.2 INTRODUCTION

Metal halide perovskites have attracted intense interests recently due to their excellent properties including high photoluminescence quantum yield (PLQY), facile bandgap tunability and simple

solution processability.[23, 82] They have been widely used in a great variety of optoelectronic devices like photovoltaics, photodetectors, light-emitting diodes (LEDs) and lasers.[19, 43, 55, 83-89] Perovskite LEDs (PeLEDs) have gone through a rapid development, and the external quantum efficiencies (EQEs) have been improved from 0.76%[30] to over 20%[10, 31, 42, 52, 53] in last several years. Besides, by appropriately passivating defects, the internal PLQYs of perovskite thin films have been approaching 100%.[7-9] However, the highest EQE that a PeLED can achieve is still limited by the light outcoupling efficiency.[90] Recent studies have shown that around 75-80% of generated power from perovskite films is trapped in PeLEDs due to the high refractive index (n > 2) of perovskite films, restricting the maximum outcoupling efficiency of PeLEDs to 20%-25%.[53, 91]

Presently most research efforts are focused on analyzing and improving the optoelectronic properties of perovskite materials, there are few publications dealing with light outcoupling of PeLEDs.[90-96] If we retrospect the development histories of OLEDs and QLEDs, research is often concentrated on material exploration in the beginning. But once the material development reaches a mature stage, more efforts are delved into the optimization of light extraction.[97] PeLEDs are expected to follow the same trajectory, therefore, the next step to optimize PeLEDs should be focused on improving the light outcoupling efficiency. In fact, there are already some outcoupling techniques successfully applied in PeLEDs. For examples, Zhang *et al.* fabricated PeLEDs on three-dimensional nanophotonic substrates to enhance light extraction.[94] Shen *et al.* integrated bioinspired moth eye nanostructures into a ZnO layer and achieved a record EQE of 28.2% among PeLEDs.[95] However, these techniques usually require complicated fabrication procedures to produce photonic nanostructures. Engineering the optoelectronic properties of materials used in PeLEDs can provide more cost-effective approaches to increasing their EQE. The investigation on

the underlying physics of light outcoupling from PeLEDs is a necessary step toward this goal. Shi *et al.* have revealed the effects of the thickness and refractive index of perovskite films on light outcoupling from PeLEDs.[91] In this study, we demonstrate the emitter orientation also plays an important role in light extraction from PeLEDs.

2.3 RESULTS AND DISCUSSION

In general, the EQE of a PeLED is determined by four individual factors:[91, 93]

$$EQE = \eta IQE = \eta\gamma\eta_{S/T}q_{eff} \tag{2.1}$$

Where η is the light outcoupling efficiency and IQE is the internal quantum efficiency, which is the product of the charge injection balance (γ), the singlet/triplet capture ratio ($\eta_{S/T}$) and the effective radiative quantum yield (q_{eff}). Generally, the $\eta_{S/T}$ is close to unity for perovskite films, thus we can usually neglect this item in the equation.[91] The effective radiative quantum yield is closely connected to the intrinsic quantum yield (q) of perovskite films, the relationship can be described as[98]

$$\frac{q_{eff}}{q} = \frac{F}{qF+1-q} \tag{2.2}$$

Where F is the Purcell factor that describes how the cavity affects the dipole power generated inside the perovskite layer.

The charge injection balance can be well-adjusted by selecting proper transport layers and tuning their thicknesses.[99] The effective quantum yield can be improved by passivating defects and confining bounded excitons.[100] Therefore, equation (1) shows studying the limits of the light outcoupling efficiency η is of great importance for achieving a high EQE. **Figure 2.1(a)** shows the device structure of the PeLED studied in this work. The device consists of a glass substrate covered with a 150 nm-thick indium tin oxide (ITO) layer. A $CsPbBr_3$ layer with various thickness

is sandwiched between a 30 nm poly-TPD layer (hole transport layer (HTL)) and a 40 nm TPBI (electron transport layer (ETL)). **Figure 2.1(b)** shows the PL spectrum of a $CsPbBr_3$ film, the PL peak wavelength is located at 523 nm.

We adopt an optical simulation based on a classical dipole model to study the effect of the dipole orientation on the outcoupling efficiency of PeLEDs.[101, 102] The inset of **Figure 2.1(a)** illustrates the *x*-*y*-*z* coordinates. The emitting dipoles in perovskite films with random orientation can be treated as a superposition of p_x, p_y and p_z dipoles. With respect to the substrate plane (*x*-*y*), we define p_x and p_y dipoles are oriented horizontally while p_z diploes are oriented vertically. If we choose the *x*-*z* plane as the plane of incidence, p_y dipoles emits *s*-polarized light whereas p_x and p_z dipoles are accounting for *p*-polarized emission.[103] The radiation of a dipole is strongest perpendicular to the dipole orientation.[104] Therefore, p_z dipoles mainly emit light travelling with a large angle to the surface normal (*z* direction).[105] Due to the total internal reflection (TIR), the generated light with a large emission angle can easily be trapped inside the functional layers (ITO, HTL, perovskite, ETL) and couples to evanescent waves at the ETL/metal interface, accounting for a low outcoupling efficiency for light emitted from p_z dipoles. Therefore, horizontally oriented p_x and p_y dipoles are preferred in terms of improving light extraction from PeLEDs. The ratio of the vertical dipoles to total dipoles is defined as Θ, and it is equal to 0.33 in the isotropic dipole case. We assume the charge injection is well balance with $\gamma=1$, and the intrinsic quantum yield q = 0.9, according to state-of-art PLQYs of perovskite films in reported literatures.[8, 9] The emitting dipoles are assumed to locate at the middle of the perovskite layer.

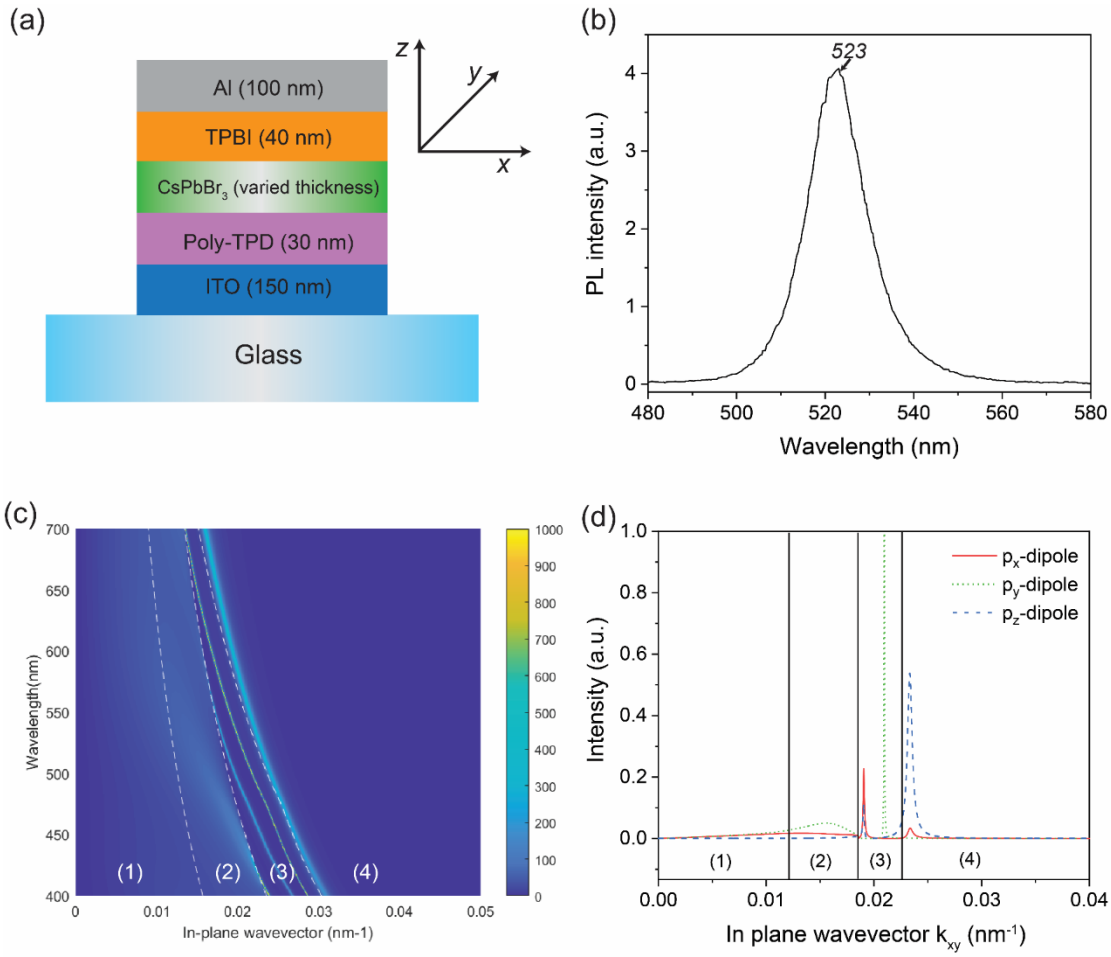

Figure 2.1. Power distribution of Horizontal (in-plane) and vertical dipoles. (a) Schematic structure of the PeLED studied in this work. The inset schematically defines the *x*-*y*-*z* coordinates. (b) PL spectrum of the $CsPbBr_3$ film. (c) Simulated power distribution diagram in PeLEDs assuming isotropic emitter orientation. The white dashed lines divide the graph to four regions: (1) direction emission, (2) substrate mode, (3) waveguide mode and (4) surface plasmon mode. (d) Power dissipation spectrum of p_x, p_y and p_z dipoles at the wavelength of 523 nm.

Figure 2.1(c) shows the total optical power distribution diagram of PeLEDs with isotropic dipole orientation ($\Theta = 0.33$). We can distinguish four optical channels of PeLEDs from left to right: direct emission, substrate mode, waveguide mode and surface plasmon mode.[90] These four channels are separated by the in-plane wavevector k_{xy}: (1) Direct emission: $k_0 \cdot n_{air} \geq k_{xy} \geq 0$,

where $k_0 = 2\pi/\lambda$ is the vacuum wave vector, and n_{air} is the refractive index of air. In this region, light outcouples into the air from PeLEDs. (2) Substrate mode: $k_0 \cdot n_{sub} \geq k_{xy} \geq k_0 \cdot n_{air}$, where n_{sub} is the refractive index of the substrate. In this region, light is trapped in the substrate due to the TIR at the substarte and air interface. (3) Waveguide mode: $k_0 \cdot n_{eff} \geq k_{xy} \geq k_0 \cdot n_{sub}$, where n_{eff} is the effective index of the functional layers (including ITO, HTL, perovskite and ETL). In this region, light is trapped in functional layers because of the TIR at the ITO and substrate interface. (4) Surface plasmon mode: $k_{xy} \geq k_0 \cdot n_{eff}$. In this region, light couples to the top metal electrode in the form of evanescent waves. It is noticed that a large portion of optical power couples to two sharp waveguide modes (region 3) and one surface plasmon mode (region 4). **Figure 2.1(d)** shows the individual contributions from p_x, p_y and p_z dipoles to the power dissipation spectra. Most of the optical power generated from p_z dipoles couples to surface plasmon and waveguide modes, consistent with the low outcoupling efficiency for vertically oriented dipoles. The horizontally oriented p_x and p_y dipoles both have large contributions to direction emission and substrate modes (region 1 and 2). The two distinct sharp peaks in region 3 correspond to *p*-polarized and *s*-polarized waveguide modes for p_x and p_y dipoles, respectively.

Figure 2.2(a), (b) present the simulated power distribution into different optical modes of PeLEDs with various perovskite layer thickness for isotropic ($\Theta = 0.33$) and horizontal ($\Theta = 0$) dipole orientation, respectively. The nonradiative loss reflects the effective quantum yield qeff, which is affected by the Purcell factor of a PeLED cavity. As the perovskite layer is between the Al anode and bottom substrate, the variation of the perovskite layer thickness greatly modifies the PeLED cavity, accounting for the oscillating behaviors in direct emission. The coupling to surface plasmons is mainly determined by the distance from the emitting dipole location to the metal electrode. Therefore, the power fraction of the surface plasmon mode shows a declining trend as

the perovskite layer thickness increases. On the opposite, the power fraction of the waveguide mode shows an increasing trend, which can be easily understood considering more light is trapped in functional layers due to the TIR as the perovskite layer thickness increases. It is obvious that PeLEDs with horizontal dipole orientation show increased outcoupling efficiency compared to those with isotropic dipole orientation for various thickness of perovskite layers. In addition, as only vertically oriented dipoles mainly contribute to the surface plasmon mode, PeLEDs with horizontal dipole orientation show much smaller power fraction of the surface plasmon mode.

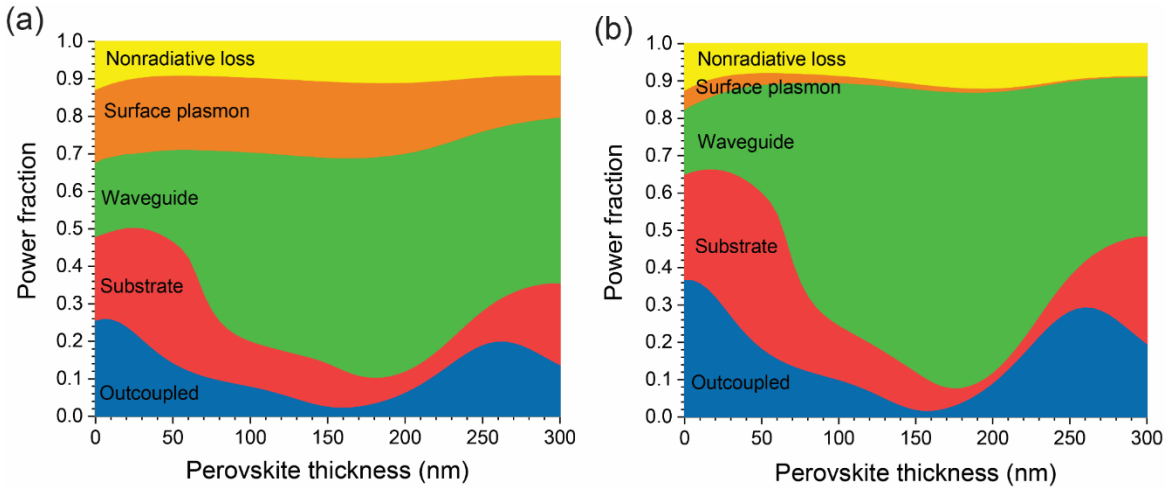

Figure 2.2. Power distribution into different optical modes of PeLEDs with various perovskite layer thickness. (a) isotropic dipole orientation (Θ = 0.33) (b) horizontal dipole orientation (Θ = 0).

Angular *p*-polarized PL measurement can be used to determine the dipole orientation of perovskite films.[97, 106, 107] **Figure 2.3(a)** schematically illustrates the experimental setup. A 40 nm thick $CsPbBr_3$ film deposited on a glass substrate is excited by a continuous wave (CW) laser with a wavelength of 405 nm. To extract the light trapped in the substrate, a glass half-ball lens is attached to the substrate with index-matching fluid (IMF, n =1.52). The whole sample is placed at the center of a rotation stage, which can be rotated to various angles. The x-y-z coordinate is

annotated in the figure for the sample rotated to the angle θ. The angular light emissions go through a linear polarizer with vertical polarization axis (annotated inside the polarizer) and then get collected by a fiber-coupled spectrometer with a collimator. The light emitted from p_y dipoles is *s*-polarized (perpendicular to x-z plane), which will be blocked by the polarizer filter. The angular PL is only contributed by *p*-polarized emission from horizontally oriented p_x dipoles and vertically oriented p_z dipoles. We simulated the angular *p*-polarized PL intensity profiles by assuming different dipole orientations of perovskite films, the results are shown in **Figure 2.3(b)**. Because the optical power in the substrate mode can be extracted by the attached half-ball lens, there are PL intensity peaks emerging at the angles greater than approximately 41° (the TIR angle at the substrate and air interface). As the vertical dipole ratio (Θ) increases, the intensity of this peak also increases. This is because, for this sample without the metal electrode, the vertical dipoles radiate mostly into the substrate mode while the horizontal ones mainly outcouple to the air. The PL intensity peaks at angles great than 41° can be used to quantify the Θ value. By fitting measured experimental data (solid circles) in **Figure 2.3(c)**, we extract the value of Θ to be 0.41. This result indicates the dipole orientation in $CsPbBr_3$ films is more vertically oriented, which is not very favorable in terms of light extraction. The slightly vertically orientated dipole orientation in $CsPbBr_3$ films is consistent with reported literatures,[93, 96, 108, 109] and it may be caused by induced vertical alignment of dipoles at the perovskite/substrate interface due to localized electrostatic surface charges [96, 108]. However, the Θ value is also highly dependent on film morphology, crystal orientation, electronic transfer and dielectric environment.[53, 96, 108-110] By depositing a Al_2O_3 layer on top of perovskite nanocrystal films, Jurow *et al.* could counterbalance the influence of the substrate and decreased the transition dipole to surface angle by more than 50% to only 14°.[96] The

feasibility to control the dipole orientation of perovskite films provides great potential for achieving high-efficiency PeLEDs.

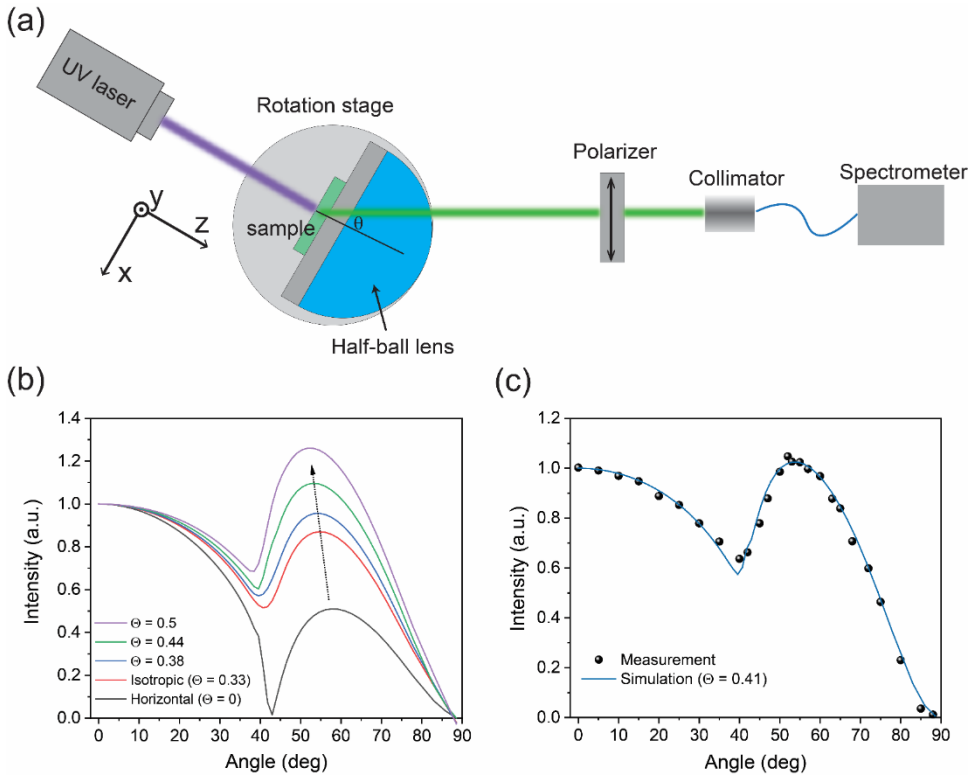

Figure 2.3. Quantifying the dipole orientation of a perovskite emitter. (a) Schematic experimental setup for measuring the dipole orientation of perovskite films. (b) Simulated *p*-polarized PL intensity as a function of emission angle. (c) Measured data and the fitting curve (Θ = 0.41).

Furthermore, we studied the dependence of the EQE on the dipole orientation and perovskite layer thickness (assuming $\gamma=1$, q = 0.9). **Figure 2.4** shows both factors significantly influence the EQE. For PeLEDs with various perovskite layer thickness, the EQE increases as the dipole orientation become more horizontal (Θ decreases). This indicates further improvement of PeLEDs should be feasible through designing perovskite materials with more horizontally oriented dipoles.

The optimum thickness of the $CsPbBr_3$ layer in PeLEDs is 10-15 nm in the case of Θ = 0.41. But even for a 30 nm thick $CsPbBr_3$ layer (Θ = 0.41), the EQE can keep at 20%. Such thickness is commonly used in PeLEDs as a perovskite layer that is too thin leads to poor coverage and shorting problems, and a perovskite layer that is too thick leads to loss of electron-hole pairs for radiative recombination during the charge transport process. In our simulation, the maximum EQE that PeLEDs can achieve is about 36% with a horizontal dipole orientation (Θ = 0). Considering the current record efficiency of 21.6% among PeLEDs without outcoupling nanostructures, we believe there is still much room for the performance improvement of PeLEDs.

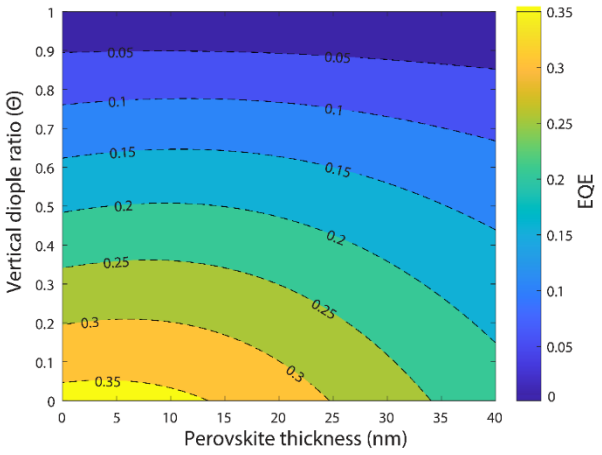

Figure 2.4. Contour plot of the simulated EQE as a function of the perovskite layer thickness and vertical dipole ratio (Θ). The black dashed lines represent the contour lines of the EQE.

In addition to the emitter orientation, the thickness and refractive index of perovskite films are also of importance determining the outcouping efficiency of PeLEDs. **Figure 2.5(a)** shows the dependence of outcoupling efficiency on perovskite refractive index for 15 and 40 nm thick perovskite layers. Generally, in PeLEDs with bulk thin films, the thickness of the perovskite layer is 30-50 nm. Usually, the outcoupling efficiency decreases when the refractive index of the emitter layer increases. The reason is that there are more internal reflections inside the emitter layer due

to high refractive index. Therefore, more waveguided light is trapped inside the emitter layer. However, for ultrathin perovskite layer (15 nm), the outcoupling efficiency doesn't vary too much just because the perovskite layer is too thin. Therefore, we can conclude that the outcoupling efficiency of ultrathin PeLED is not sensitive to the refractive index of perovskite materials, which is a big advantage. If the thickness increases, the outcoupling efficiency will be sensitive to the refractive index, and a high outcoupling efficiency requires a low refractive index, which is opposite to the relatively high refractive index of perovskite (usually between 2.0-2.7, depending on halide composition, preparation method etc.). **Figure 2.5(b)** shows the power dissipation spectra of PeLEDs with 15 and 40 nm thick emitter. It can be clearly observed that the power intensity of 15 nm thick device is higher than that of 40 nm thick device for all in-plane wavevectors in the direct emission region.

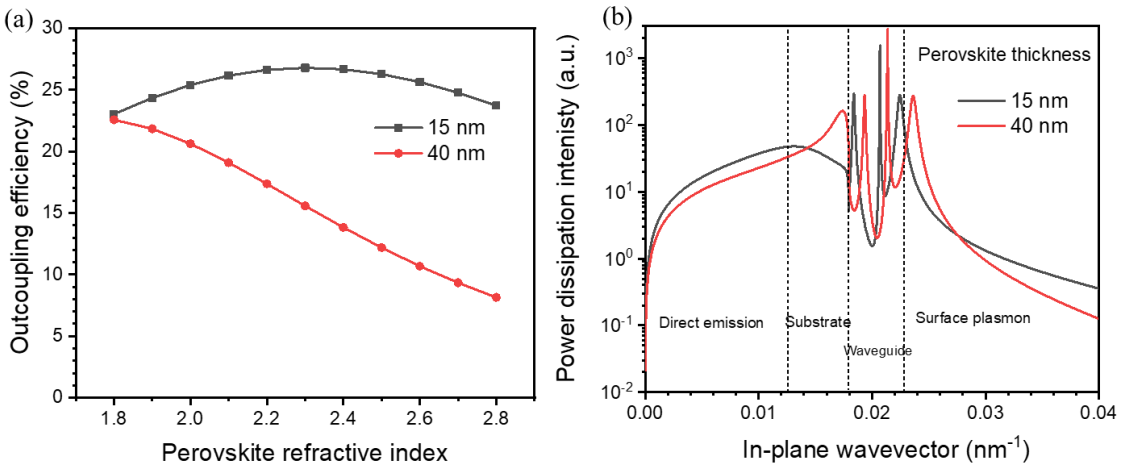

Figure 2.5. Sensitivity of Outcoupling efficiency on perovskite refractive index for thin and thick perovskite films. (a) The dependence of outcoupling efficiency on perovskite refractive index and (b) power dissipation spectra for PeLEDs with 15 and 40 nm thick perovskite layers.

2.4 CONCLUSION AND OUTLOOK

In summary, we have investigated the effect of the dipole orientation on the outcoupling efficiency of PeLEDs through optical simulations. We show horizontally oriented dipoles are preferred over vertically oriented dipoles in terms of improving light extraction. A perovskite emitter with a horizontal transition dipole moment can lead to a potential maximum EQE of 36% considering an IQE of 90%, well beyond the limits of isotropic light sources. By performing angular *p*-polarized PL measurements, we find the dipole orientation in $CsPbBr_3$ films is more vertically oriented, which is not very favorable in terms of light extraction. Further control of the dipole orientation of perovskite films by engineering film morphology, crystal orientation and interfacial interactions holds great promise for significant advance of PeLED performance.

Currently, the physic mechanisms to tune the emitter orientation of perovskite films still need intensive investigation. Kim *et al.* developed a host/guest system which has preferentially horizontal dipoles by doping proper phosphorescent dye molecules in OLEDs, such an approach may be enlightening in PeLEDs.[97] In addition, photon recycling can be prominent in perovskite materials which have sufficiently high radiation efficiency and small Stocks-shift (strong overlap between absorption and emission spectra). The photon recycling events can help waveguided light outcouple to air during the reabsorption and reemission processes. Cho *et al.* demonstrated that photon recycling can contribute higher than 70% to the total emission.[111] By maximizing the benefit of photo recycling by increasing the reabsorption coefficient and PLQY, the EQE of PeLEDs is expected to be further improved. However, The PLQY should be sufficiently high otherwise the benefit from photon recycling may not exceed the reabsorption loss and the EQE with photon recycling contribution is similar to that for a non-absorbing perovskite.

Apart from engineering perovskite materials, the alternative option is to engineer other layers in the device stack. By taking place of glass (n = 1.52) with sapphire (n = 1.77) substrates, we demonstrated the power fraction of waveguide mode decreases while more light is distributed into outcoupled and substrate modes (**Figure A.1**).[87] Combined with sapphire half-ball lens and index matched fluid, we can expect to extract all the light trapped in the substrate to boost the device efficiency significantly.

Chapter 3. PEROVSKITE QUANTUM DOT LIGHT-EMITTING DIODES

Adapted with permission from:
Zou, C., Huang, C.Y., Sanehira, E.M., Luther, J.M. and Lin, L.Y. Highly stable cesium lead iodide perovskite quantum dot light-emitting diodes. *Nanotechnology*, *28*(45), p.455201.

3.1 ABSTRACT

Recently, all-inorganic perovskites such as $CsPbBr_3$ and $CsPbI_3$, have emerged as promising materials for light-emitting applications. While encouraging performance has been demonstrated, the stability issue of the red-emitting $CsPbI_3$ is still a major concern due to its small tolerance factor. The $CsPbI_3$ bulk films are only stable in cubic phase at temperature over 300 ℃, which makes it hard to apply them in red-emission PeLEDs. However, the reduced surface energy of quantum dots can help stabilize $CsPbI_3$ in cubic phase, here we report a highly stable $CsPbI_3$ quantum dot LED with red emission fabricated using an improved purification approach. The device achieved decent external quantum efficiency (EQE) of 0.21 % at a bias of 6 V and outstanding operational stability, with a L_{70} lifetime (EL intensity decreases to 70% of starting value) of 16 h and 1.5 h under a constant driving voltage of 5 V and 6 V (maximum EQE operation) respectively. Furthermore, the device can work under a higher voltage of 7 V (maximum luminance operation) and retain 50% of its initial EL intensity after 500 s. These findings demonstrate the promise of $CsPbI_3$ quantum dots for stable red LEDs and suggest the feasibility for electrically pumped perovskite lasers with further device optimizations.

3.2 INTRODUCTION

Recent years have been marked with increased attention to achievement by solution-processed halide perovskite materials in the field of light-emitting diodes (LEDs) [5, 30, 50, 112]. Most of the prior work use organic-inorganic hybrid perovskites, such as $CH_3NH_3PbBr_3$ ($MAPbBr_3$) as active layers [113-115]. Despite the demonstrated strong photoluminescence quantum yields (PLQY), the stability issue of $MAPbBr_3$ remains a critical challenge for further development and commercialization of perovskite-based LEDs. More recently, a growing number of research studies have been devoted to all-inorganic perovskites, such as cesium lead bromide ($CsPbBr_3$), which exhibit higher thermal stability and outstanding optical properties, especially their high PLQY [116, 117]. However, cubic phase $CsPbI_3$ bulk films, which is required to generate red light, are still only stable at high temperature above 300 °C, not desirable for practical applications.

Our previous work has shown quantum dot (QD) surfaces can be used to stabilize cubic phase $CsPbI_3$ at room temperature [118]. Furthermore, QD structure is desirable for LED applications due to the added ability of precise control over the emission wavelength with a narrow emission spectrum and strong quantum confinement effect. As a result, all-inorganic perovskite QDs have been pursued as LED materials and have been demonstrated with higher thermal stability compared to the organic cation-based perovskites [119-124]. Although some stability tests have been performed on the all-inorganic perovskite QD-based LEDs, there is limited study on the mechanisms of device degradation in the literature, which is required before this research field can be further developed for practical applications.

To generate high-power white light for illumination, one of the effective approaches is to use individual LEDs that emit three primary colors and then mix all the colors to form white light. All-inorganic PeLEDs based on $CsPbBr_3$ QDs have been investigated as a green light source, and a

peak external quantum efficiency (EQE) exceeding 8.7% has recently been demonstrated[125]. To achieve red-emitting PeLEDs which is indispensable for white light generation, $CsPbI_3$ QDs readily emit in the proper wavelength range. However, reported research results on $CsPbI_3$ QD LEDs are still scarce before 2017, with electroluminescence from $CsPbI_3$ QDs reported recently [118, 119, 126, 127]. The underlying reason may be attributed to the small tolerance factor of $CsPbI_3$ QDs [128].

Goldschmidt's tolerance factor is an indicator for the stability and distortion of crystal structures [129], which accounts for the relative size of the constituent ions. Yakunin *et al.* have demonstrated red LEDs fabricated with $FAPbI_3$ and $Cs_{0.9}FA_{0.1}PbI_3$ QDs with impressive colloidal stability [130], however, little is known about the operational stability of these red-emitting perovskite QD LEDs thus far. A novel purification method has been employed in our previous work for retaining the phase stability of the $CsPbI_3$ QDs [118]. In this study, we show that red-emitting LEDs consist of the above-mentioned all-inorganic $CsPbI_3$ QDs can achieve outstanding operational stability with a maximum EQE of 0.21%. Our LEDs achieve a high L_{70} lifetime over 16 h under a constant applied voltage of 5 V (J = 23 mA/cm^2), at the same time, a decent peak EQE of 0.21% is obtained, which is comparable with other all-inorganic perovskite QD LEDs. Red emission which hits the red corner of Commission Internationale de l'Eclairage (CIE) chromaticity diagram also has been observed, enabling excellent display and white PeLED technology.

3.3 METHODS

The fabrication method of $CsPbI_3$ QDs can be found in our previous report [118]. In general, methyl acetate (MeOAc) was added into the crude $CsPbI_3$ QD solution to wash and isolate QDs, the purified QDs were dispersed in hexane or octane. The formation of α-$CsPbI_3$ QDs are phase-stable for months in ambient. Recently, Zeng *et al.* also reported the different performances of perovskite

QDs by using different solvents for purification process [131]. The octane and hexane are usually used to disperse perovskite QDs since they have the similar polarity to that of the surface ligands (oleic acid and oleylamine). Given the ionic nature of perovskites and the ionic binding of the ligands, the solvents with high polarity like DMF and DMSO could completely dissolve the ionic perovskite. Therefore, the non-solvents with low polarity are preferred for purification process. Compared to 1-butanol, acetone, ethyl acetate, Me(OAc) was tested to be able to successfully extract the stable $CsPbI_3$ QDs with cubic phase. Other solvents destabilized QDs and resulted in pale yellow and PL inactive solution after a short time storage. The synthesized $CsPbI_3$ QDs purified by Me(OAC) shows nearly unchanged absorption spectra after being placed in ambient condition for 10 days, as shown in **Figure A.2**.

Material properties of the $CsPbI_3$ QDs were characterized first. UV-Visible absorption spectra of $CsPbI_3$ thin films were measured by Varian Cary 5000 UV-vis-NIR Spectrophotometer. Steady-state PL spectra were obtained using a spectrofluorometer (Fluorolog FL-3, Jobin Yvon Horiba) with xenon short arc lamp as the light source. Transient PL lifetime data were acquired using a time-correlated single-photon counting (TCSPC) system (FluoTime 100, PicoQuant) with a pulse laser excitation source (470 nm, 60 ps, 40 MHz) at a low pump intensity.

The $CsPbI_3$ QD LED has a device structure with the following layers in order: Indium tin oxide (ITO) coated glass, PEDOT:PSS (30nm), $CsPbI_3$ QDs (~70 nm), TPBI (35 nm), LiF (1 nm)/Al (150 nm). Prepatterned ITO-coated glass substrates were first cleaned by sonication in detergent water, isopropyl alcohol (IPA) and DI water sequentially for 30 min, followed by ozone plasma treatment for 15 min. The PEDOT:PSS solution was filtered by 0.45 um nylon syringe filters and spin-coated onto prepatterned ITO substrates at 4000 rpm for 30 s, followed by annealing on a hot plate at 140 °C for 15 min. Next, the $CsPbI_3$ QD solution was spin-coated at

1000 rpm for 45 seconds two times to obtain a continuous and smooth film. The as-coated substrates were then transferred into a N_2-filled glovebox. Finally, TPBI (35 nm), LiF (1 nm), and Al (150 nm) layers were deposited sequentially by thermal evaporation through shadow masks at the rate of 1.0, 0.1 and 2 Å/s respectively. The device area was 0.05 cm^2 as defined by the intersection area between the bottom ITO and top Al electrodes.

To evaluate the device performance, we carried out various characterizations on the devices in ambient conditions under room temperature with lab humidity of 65%. The EL spectra, CIE color coordinates and luminance (*L*)-current density (*J*)-voltages (*V*) characteristics were collected using a computer-controlled system incorporating a Keithley 2400 source meter and a Konica Minolta CS-2000 spectroradiometer. A calibrated Newport 818-UV Si photodetector (active area: 1 cm^2) was centered above one LED pixel at a fixed distance (2 cm) to measure the emitted front-face power output through the ITO substrate. Lambertian profile was used for calculating the EQE, which can be expressed as the ratio of the number of output photons to that of injected electrons[6]:

$$\mathrm{EQE} = \frac{N_{photon}}{I/e} * \frac{a^2+L^2}{a^2} \tag{3.1}$$

Where N_{photon} is the number of emitted photons collected by the photodetector (calculated from the measured power and the corresponding EL spectrum), and *I* is the injection current. *L* is the distance between the light-emitting pixel and the photodetector, while *a* is the radius of the photodetector active area.

3.4 Results and Discussion

The UV-Visible absorption and PL spectra of the as-prepared $CsPbI_3$ QD film are shown in **Figure 3.1(a)**. We can observe a PL peak located at 685 nm. The absorption edge is also near 685 nm. We

measured the absorption curves after 0, 5, and 10 days storage, and discovered an encouraging result that the absorption property of the material doesn't change significantly. **Figure 3.1(b)** shows the transient PL decay trace. A PL lifetime of ~6 ns was extracted by fitting the data using a single-exponential decay model [126].

The charge mobility in the $CsPbI_3$ QD films can be measured using a space charge-limited current method[132-134]. Hole-only devices were fabricated using the structure ITO/PEDOT:PSS/$CsPbI_3$/Au, The energy level alignment makes the whole device only transport holes. **Figure 3.1(c)** shows the current dependence on voltage in dark condition. At first, the current shows linear dependence, which indicates an ohmic characteristic. The I-V curve shows a different pattern identified by the dramatic increase of the current at 1.2 V, indicating the beginning of a trap-filling process. After the traps are completely filled, the device reaches the child region [134]. The dark current shows quadratic dependence on voltage ($I \sim V^2$) in this region. Furthermore, the dark current can be fitted by the Mott-Gurney law:

$$J_d = \frac{9\varepsilon\varepsilon_0\mu V^2}{8L^3} \tag{3.2}$$

Where V is the applied voltage, J_d is the current density, ε (28) is the relative dielectric constant for $CsPbI_3$ QDs. L is the thickness of the $CsPbI_3$ QD film, which is estimated to be ~100 nm from the scanning electron micrograph (SEM) image. From here, we can extract the mobility (μ) of our $CsPbI_3$ QDs to be 1.4×10^{-4} cm^2 V^{-1} s^{-1}, which is comparable to the reported mobility of 10^{-4} cm^2 V^{-1} s^{-1} in $MAPbI_3$ thin films [135] and other inorganic QDs like PbSe [136].

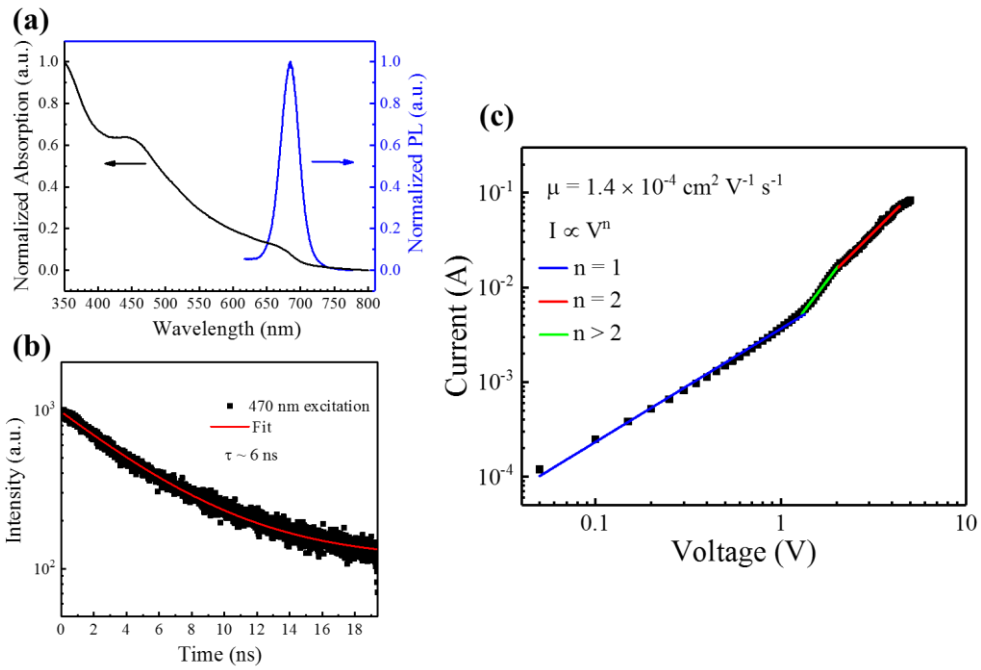

Figure 3.1. Characterizations of $CsPbI_3$ QD films. (a) UV-Visible absorption and PL spectra. (b) Transient PL measurement. A lifetime of 6 ns was obtained from fitting the data. (c) I-V measurement of a hole-only device in the dark condition for extracting the mobility in the $CsPbI_3$ QD film using a space charge-limited current method.

A schematic device structure is shown in **Figure 3.2(a)**, and the corresponding SEM cross-section image of the as-fabricated LED device is shown in **Figure 3.2(b)**. All device layers can be clearly identified. The flat-band energy diagram of the device is illustrated in **Figure 3.2(c)**, in which TPBI and PEDOT:PSS are employed as electron and hole transport layer (ETL and HTL), respectively [137]. On the other hand, they also block holes and electrons respectively due to the appropriate HUMO and LOMO values, which facilitates the recombination of electro-hole pairs in the perovskite active layer.

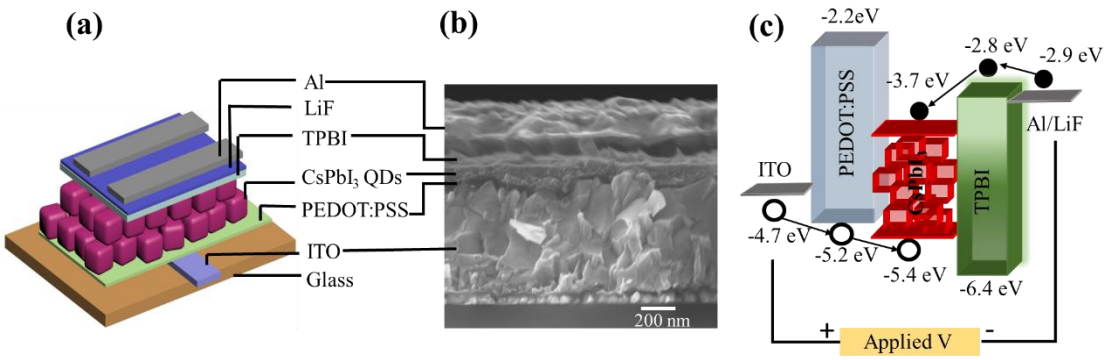

Figure 3.2. $CsPbI_3$ QD LED device stack. (a) Schematic diagram of the $CsPbI_3$ QD LED device structure. (b) The cross-section view SEM image of the fabricated device. (c) Energy band diagram of the LED device.

The *L-J-V* characteristics of the device are presented in **Figure 3.3(a)**. The $CsPbI_3$ QD LED shows a clear diode characteristic with a turn-on voltage V_{on} of 3 V. The luminance achieves a maximum value of 7.2 cd/m^2 under a bias voltage of 7 V. The current efficiency and EQE as a function of the applied voltage in logarithmic and linear scale for the $CsPbI_3$ QD LED are shown in **Figure 3.3(b)**. A maximum current efficiency of 0.012 cd/A and EQE of 0.21% are observed at an applied bias of 6 V. The EQE can be further increased by enhancing the PLQY and conductivity of $CsPbI_3$ QD thin films in addition to better device design to minimize the energy barriers at all interfaces [122]. We also found that the active perovskite layer thickness affected EQE and device performance substantially. We spin-coated $CsPbI_3$ QDs with different spin parameters to change the active layer thickness. A maximum EQE was achieved by a two-cycle spin coating process, which resulted in an approximately 70 nm-thick active layer.

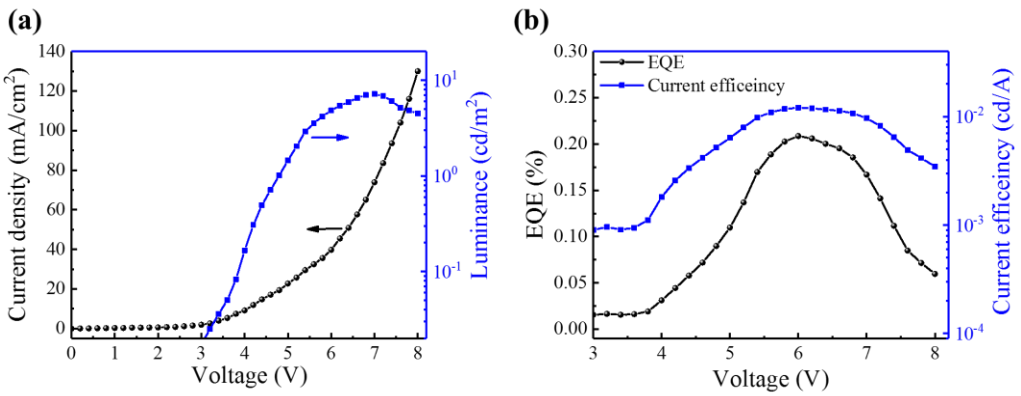

Figure 3.3. Performance characterizations of $CsPbI_3$ QD LEDs. (a) Current density and luminance versus voltage, and (b) external quantum efficiency and current efficiency versus voltage for the $CsPbI_3$ QD LEDs.

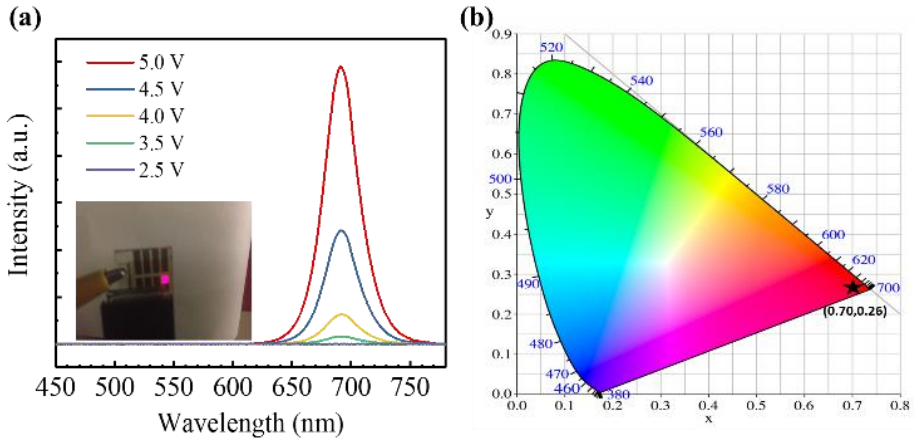

Figure 3.4. Colorimetric characterizations of red emissions from $CsPbI_3$ QD LEDs. (a) EL spectra under different applied voltages. Inset: Photograph of the device in operation, showing red emission. (b) CIE coordinates of the emitted light from the $CsPbI_3$ QD LED.

Figure 3.4(a) presents the EL spectra of the $CsPbI_3$ QD LED under different applied biases. As the applied voltage increases, a narrow EL peak at 693 nm starts to emerge (FWHM linewidth $\Delta\lambda$ ~ 32 nm). It should be noted that there are no notable parasitic emissions from the charge transport layers and the shape of the EL spectrum doesn't change at different applied voltages.

These observations indicate that carriers are well confined in the perovskite QD layer and the recombination zone doesn't change in response to different applied voltages [50]. The inset photo shows a bright and uniform red light from a $CsPbI_3$ QD LED in operation. The EL corresponds to the CIE color coordinates of (0.70, 0.26) at 5 V, which is on the red corner of the CIE color diagram, as shown in **Figure 3.4(b)**.

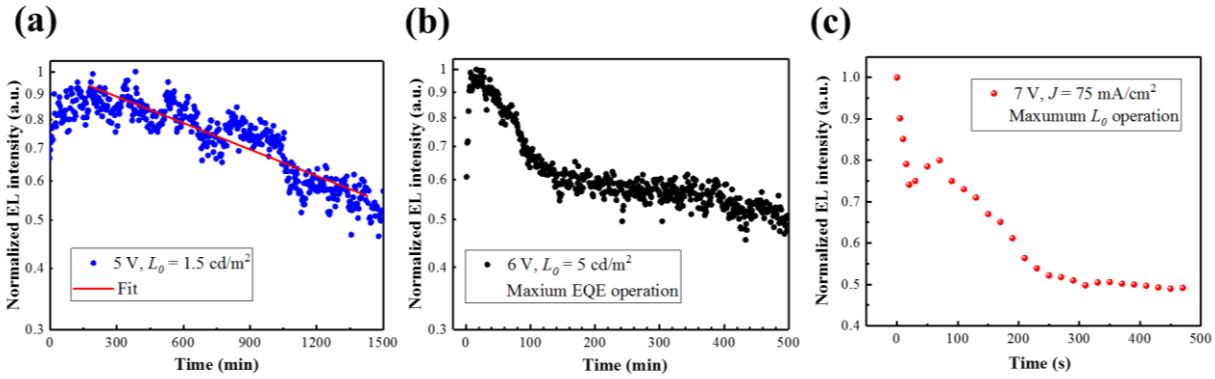

Figure 3.5. Operational stability characterizations of $CsPbI_3$ QD LEDs. Under (a) low bias of 5 V, (b) 6 V bias where maximum EQE is achieved, and (c) high bias and current injection condition (7 V, J = 75 mA/cm^2), where maximum luminance is reached. (a) and (b) are in logarithmic scale and (c) is in linear scale. The measurements were performed at room temperature under ambient conditions.

To further the advancement of perovskite materials for LED applications, understanding the device stability behaviour under varying driving voltages is required. The operating lifetime is typically tested for the purpose of determining the resistance of materials under electrical and thermal stress. LED lifetime is measured by how the intensity of emitted light diminishes over time. According to IES TM21 standard criterion, we define the time it takes for the EL intensity decreasing to 70% of the initial intensity as L_{70} lifetime (T_{70}). To evaluate the stability of the $CsPbI_3$ QD LEDs under different driving conditions, we applied different voltages to find the correlation between output EL and lifetime. The normalized EL intensity versus time under a constant applied

bias of 5 V was recorded and presented in logarithmic scale in **Figure 3.5(a)**. The corresponding luminance at the starting point is about 1.5 cd/m^2. The EL intensity slightly increases during the first 3 hours and then decreases steadily. The EL decay process can be fit well by a single-exponential decay model of $I = 0.92e^{-t/22} + 0.06$. The increase at the beginning may be attributed to an annealing effect on the perovskite QD film and/or improved interface contact caused by joule heating. During the operation of the fabricated LED, no evident changes in the peak position and shape of the EL spectra were observed. The device under the low applied bias of 5 V exhibits very high stability (T_{70} ~ 16 h). This is somewhat unexpected as the common belief is that the iodide ions would result in perovskite quantum dots with low stability due to their metastable state in the cubic phase [124, 138]. We attribute this to the process of purification using MeOAc, which results in stable $CsPbI_3$ QDs in the cubic phase [118], and thus the long lifetime of our $CsPbI_3$ QD LEDs. More importantly, we found that such an EL decay is a temporary behaviour, and the EL intensity could recover to its original status after a short relax time. This finding demonstrates that the treated $CsPbI_3$ QDs are thermally stable and will not decompose under such an applied bias and corresponding injection current (J = 23 mA/cm^2). The temperature of device increases inevitably during the stability test, which would increase nonradiative recombination rate and leads to the EL decay. To further investigate the device stability, a harsher condition with an applied bias of 6 V was used, where the device worked with the maximum EQE. The result is shown in **Figure 3.5(b)**. The corresponding luminance at the starting point is about 5 cd/m^2. In this case the output EL intensity from the light-emitting pixel also increases at the first 15 minutes. For the EL intensity decay process, it is observed that there are fast and slow decay components, which is due to the high injection current at first and the device degrades very fast as a result. In this case, L_{70} lifetime is estimated to be 1.5 hours. As shown in **Figure 3.5(c)**, under higher applied

voltage of 7 V (J = 75 mA/cm^2, maximum luminance operation), the device degrades more rapidly and retains 50 % of its initial EL intensity after 500 s. Specifically, the EL intensity drops dramatically to 75% of initial value (L_0) at the first few seconds since the device is not able to stand such high current density. Then the device performs similarly to that in the low applied voltage condition. The perovskite QDs usually have lower mobility and thermal conductivity because of the insulating surface ligands and poor transport between QDs[23], thus they typically have bad thermal stability under high injection current. However, our $CsPbI_3$ QD LED device could still tolerate such a high injection current density for 500 s, which indicates that our $CsPbI_3$ QDs have good thermal stability. Our results under both low and high injection conditions compare favorably with reported results from literature for PeLEDs [122, 123, 139]. These findings provide insight for the feasibility of electrically pumped perovskite lasers which need high injection current density to enable population inversion [140]. The operational device stability under high current injection can be further optimized and improved by using thermally stable carrier transport layers, such as inorganic materials which usually generate less resistive heating and have better thermal stability [141].

3.5 CONCLUSION AND OUTLOOK

In conclusion, we fabricated $CsPbI_3$ QD LEDs by adopting a novel purification route that enabled the QDs to retain the phase stability under current injection. Various device performance including EL spectra, CIE coordinates, *L-J-V* characteristics, luminance and EQE were characterized. We also performed stability measurements. Our devices achieved 16 h L_{70} lifetime under the applied voltage of 5 V. To the best of our knowledge this is the highest stability among iodide-based PeLEDs reported at that time. The device also showed reliable performance operating at 6 V where

the maximum EQE was achieved. The half-life time of 500 s under high applied bias of 7 V shows the feasibility for electrically pumped perovskite lasers with further device optimization. These findings suggest the promise of perovskite light-emitting devices under electrical pumping.

However, perovskite QDs often suffer from relatively poor charge transport properties because of existing organic ligands. The poor charge transport may affect the balance of charge injection and thus deteriorate the device efficiency of perovskite QD LEDs. Washing ligands is an effective way to increase the carrier mobility of perovskite QDs. However, the stability of perovskite QDs may become worse because of more exposure to ambient environment. Furthermore, the surface tension to keep QD structure is hard to maintain as the density of surrounding ligands decreases. Organic ligands also play an important effect in determining PLQY. If too many ligands are washed away, the PLQY of perovskite QDs will significantly decrease.[41] Therefore, there certainly exists a trade-off between good charge transport and high PLQY, which increases the complexity and difficulty to obtain a high-efficiency LED based on the perovskite QD emitter. In addition, similar to colloidal nanocrystals such as CdSe and PbS, the perovskite QDs also suffer from serious Auger recombination due to enhance localized carrier densities inside QDs, which may further limit their application potential in electrically driven lasers. However, after suppressing Auger recombination, several works have demonstrated CW lasing using colloidal nanocrystals.[25-27] Taking this as a lesson, perovskite QDs still hold great promise in the field of LEDs and lasers.

Chapter 4. PHOTOLITHOGRAPHIC PATTERNING OF PEROVSKITE THIN FILMS FOR MULTICOLOR DISPLAYS

Adapted with permission from:
Zou, C., Chang, C., Sun, D., Böhringer, K.F. and Lin, L.Y. Photolithographic Patterning of Perovskite Thin Films for Multicolor Display Applications. *Nano Letters*, *20*(5), pp.3710-3717. Copyright 2020 American Chemical Society

4.1 ABSTRACT

Although the achievements of highly efficient red, green and blue (RGB) PeLEDs are of importance for the commercialization of perovskite multicolor displays, however, a high-resolution method to pattern perovskite films is also a necessary keystone to achieve this goal, whereas there are few works on this topic.

In this work, we developed a high-resolution photolithographic method to pattern multicolor perovskite thin films. RGB single-color patterns were successfully fabricated with a highest resolution of 10 μm, corresponding to 1270 dots per inch (dpi). Furthermore, green and red perovskite patterns were fabricated on a single substrate based on this method, which can be applied in liquid crystal display (LCD) applications. Finally, a current-driving perovskite micro-LED display was demonstrated, the device shows great homogeneity without obvious unfunctional pixels.

4.2 INTRODUCTION

In the past several decades, discontinuous miniaturization of solution-processed semiconductor materials have been attracting a lot of attentions as this technique has great potential applications

in full-color displays, image sensors and thin film transistors (TFTs).[142-145] High-resolution lithographic patterning methods including photolithography and electron-beam lithography have been broadly utilized in organic and quantum dot (QD) optoelectronics,[146-148] promoting the commercialized development of organic and QD micro- and nano-scale devices.

Metal halide perovskites stand out from other families of semiconductor materials not only for their great optoelectronic properties, but also for their simple solution-processing preparation and facile bandgap tunability.[149] Previous works on solar cells are mainly focused on iodine-based perovskite with narrow bandgap to absorb more light. The real advantages of bandgap tunability are presented in light-emitting applications, where strong and pure color emissions covering the entire visible light range are particularly in need.

Up to now, there has been few studies on patterning perovskite films especially using lithographic methods,[150] and perovskite micro-LED displays have not been demonstrated. This may be due to the ionic nature of perovskite materials, making them prone to dissolution in common polar solvents required in high-resolution lithographic methods.[151]

To avoid the challenges in lithographic methods, many researchers have developed other methods to pattern perovskite films instead. Most remarkable, several groups inkjet-printed polycrystalline perovskite patterns on various substrates.[152-155] However, inkjet printing is a low throughout process, and usually demands substrate heating and specially prepared inks. Nanoimprinting has also been adopted to generate perovskite patterns. Wang *et al.* and Pourdavoud *et al.* thermally imprinted nano-scale photonic structures to perovskite films.[79, 156] In addition, several other groups adopted PDMS templates to force perovskite precursors crystallizing into desirable structures.[71, 157-159] However, these methods are likely to deteriorate the intrinsic properties of perovskite materials and thus affect device performance.

In industry, the more desirable manufacturing method for multicolor displays is photolithography, because it provides good resolution, high throughout, excellent reproducibility and large-scale manufacturing. Recently, Wu *et al.* and Kim *et al.* spin coated perovskite percusors on a photolithographic patterned self-assembled (SAM) layer.[144, 160] Perovskite patterns were formed in hydrophilic areas. Lin *et al.* patterned fluorinated polymer (orthogonal resist) and adopted an orthogonal solvent to lift-off perovskite films.[161] However, the orthogonal resist and solvent have to be chosen cautiously so that the solvent only dissolves the resist but not perovskite. Harwell *et al.* used SU-8 and PMMA double-layer resists on top of perovskite in a standard photolithography process and etched perovskite with argon milling.[162] However, this method involves the process of physically etching perovskite and other complicated procedures.

In this work, we develop a general photolithographic approach to pattern perovskite in micrometer resolution utilizing a dry lift-off process. No solvent is required in this lift-off process, thereby avoiding the dissolution problem of perovskite materials in common polar solvents. This approach relies on the use of parylene as an intermediary and the easy mechanical peeling-off of parylene films on various substrates.

4.3 METHODS

Materials. $PbCl_2$, $PbBr_2$, PbI_2, CsBr, CsI, PEABr and dimethyl sulfoxide (DMSO, anhydrous) were purchased from Sigma Aldrich. PEDOT:PSS (AI 4083) and TPBi (>98% purity) was purchased from Ossila. 1,4,7,10,13,16-hexaoxacyclooctadecane (18-crown-6, crown) (99% purity) were purchased from Acros. Aluminum pellets were purchased from Kurt J. Lesker.

Preparation of perovskite films. The green perovskite precursor was obtained by mixing 0.2 M CsBr, 0.2 M $PbBr_2$, 0.08 M PEABr and crown in DMSO. The blue perovskite precursor was

obtained by mixing 0.2 M CsBr, 0.1 M $PbBr_2$, 0.1 M $PbCl_2$, 0.16 M PEABr and crown in DMSO The red perovskite precursor was obtained by mixing 0.2 M CsI, 0.2 M PbI_2, 0.08 M PEABr and crown in DMSO. The addition of crown is to improve the surface morphology and PLQY of perovskite films as reported elsewhere.[163] Unless specified, the concentration of crown is 3.5 mg/ml in perovskite solutions. All precursors were heated at 60 °C for 2 h with constant stirring. The perovskite precursors were spin-coated onto substrates at 3000 rpm for 60 s with an acceleration speed of 1500 rpm/s. Afterwards, the perovskite films were immediately annealed at 100 °C for 1 min to accelerate nucleation.

Fabrication of patterned perovskite films. For single-color patterns, the parylene-C film was deposited onto a substrate at room temperature by a CVD process (PDS 2010, SCS Labcoater 2). 5g parylene-C powders were placed inside the furnace. The furnace, vaporizer and vacuum setpoints are 690 °C, 175 °C and 35 mTorr, respectively. The deposition chamber was kept at room temperature. The thickness of the parylene film was measured to be around 2.5 μm by a stylus profilometer (DektakXT, Bruker). The negative photoresist NR9-3000 was spin-coated onto the parylene film with a two-step process (1000 rpm for 5 s and 3000 rpm for 45 s) and then pre-baked at 110 °C for 5 min. The photoresist was then exposed to 365 nm UV light (~9 mW/cm^2) for 20 s (ABM semiauto-aligner) and baked at 100 °C for 5 min. The photoresist was developed in AD10 solution for 30 s and cleaned in deionized (DI) water for 15 s. The patterns should be clearly seen at this stage. The parylene film was then etched by a RIE process with mixed SF_6 (5 sccm) and O_2 (50 sccm) gas. The RF power was set as 250 W and the process pressure was 40 mTorr. The etch rate was measured as 350 nm per minute, and the parylene film was etched for 9.5 minutes. The selectivity of the photoresist to parylene was 1.2:1, so the photoresist was usually etched away after the RIE process. However, acetone or O_2 plasma could be used to strip the remaining

photoresist. The RGB perovskite precursors were then spin-cast using the above-mentioned method. The parylene film was mechanically peeled off by a narrow-tip tweezer with desired perovskite patterns remained on the substrate. Multiple standard photolithography processes could be used sequentially to pattern multicolor perovskite films on a single substrate.

Characterization of perovskite films. The PL spectra of perovskite films and patterns were measured by our home-made micro-PL system. A continuous wave (CW) laser (λ=405 nm) was used as the excitation source, the laser beam was focused onto the sample through an objective lens. The location of the laser beam was observed by a CCD camera (Chameleon 3, FLIR). The PL emission was collected by a pair of convex lenses and focused onto an optical spectrometer (OSM 100, Newport). The surface morphologies of perovskite patterns were analyzed by AFM (ICON, Bruker). The fluorescent images of perovskite patterns were obtained by a fluorescent microscope (EVOS, Thermo Fisher Scientific).

Fabrication of micro-LED displays. To avoid the electrical shunt path between ITO and Al, a 120 nm thick SiO_2 layer was deposited by plasma enhanced chemical vapor deposition (PECVD) at 125 °C onto ITO-coated glass substrates. The parylene film was deposited onto SiO_2 by CVD at room temperature. The parylene film was then etched using the same procedure above-mentioned. The trenches were transferred to the SiO_2 layer by RIE with a gas mixture of CF_4 and CHF_3. PEDOT:PSS was spin-coated at 4000 rpm and annealed at 110 °C for 10 min, the annealing temperature should not be over 130°C as parylene may become softened at this temperature and hard to peel off afterwards. The green perovskite precursor was spin-cast as above mentioned. The samples were then transferred into a thermal evaporator and the chamber was pumped to a base pressure below 2×10^{-6} Torr. TPBi (40 nm) and LiF (1 nm) were thermally evaporated at a rate of 0.8 and 0.3 Å/s, respectively. Finally, functional layers were lifted off by peeling off the parylene

film. The top electrode Al (70 nm) was deposited through thermal evaporation at a rate of 2 Å/s. The SiO_2 layer works as a separator layer to isolate individual micro-LED pixels.

Characterization of perovskite micro-LEDs. The current density-voltage (*J-V*) characteristics were measured by a source meter (Keithley 6430). Simultaneously, front-face EL power output from the ITO side was measured by a calibrated silicon photodiode (Newport 818-SL). The EQE was calculated as the ratio of the number of emitted photons to the number of injected electrons. The EL spectra of PeLEDs were measured by a fiber-coupled spectrometer (OSM 100, Newport). All device measurements were carried out under ambient conditions. The EL images of perovskite micro-LED displays were obtained by an optical microscope in dark field.

4.4 RESULTS AND DISCUSSION

4.4.1 *Single-color patterns*

For photolithographic patterning of perovskite thin films, the lift-off process may be preferable as it avoids the process of etching perovskites. However, the problem with this process still exists in finding appropriate orthogonal solvents and resists to address the incompatibility of perovskites with the solvents used for photoresist removal. Here, we developed a dry lift-off process which relies on the limited adhesion of parylene to various substrates.[164, 165] The type of parylene we used in this work is parylene-C as it has a very low permeability to solvents.

Figure 4.1a depicts the fabrication procedures of patterning perovskite thin films. First, a ~2.5 μm-thick parylene film was deposited onto the clean substrate by room-temperature chemical vapor deposition (CVD). Subsequently, standard photolithography was used to fabricate desired trenches in the photoresist layer (step 3-5). The patterned trenches were then transferred to the parylene film by reactive ion etching (RIE). The remaining photoresist was stripped by O_2 plasma

or acetone. Then, the perovskite precursor was spin-coated to the substrate followed by annealing at 100 °C to promote the crystallization. To increase the PLQY of perovskite thin films, we used quasi-2D perovskites here due to their better exciton confinement provided by the multiple quantum wells structure.[100] For green perovskite precursors, approximate amount of phenethylammonium bromide (PEABr), CsBr and $PbBr_2$ were mixed in dimethyl sulfoxide (DMSO) solvent. The PLQY of green perovskite films could reach over 70%. For blue and red perovskites, part of the bromide halides was replaced by chloride and iodine halides, respectively. Finally, the underlying parylene film was easily peeled off by a narrow-tip tweezer. Using this approach, we could pattern large-scale and multicolor perovskite films on various substrates.

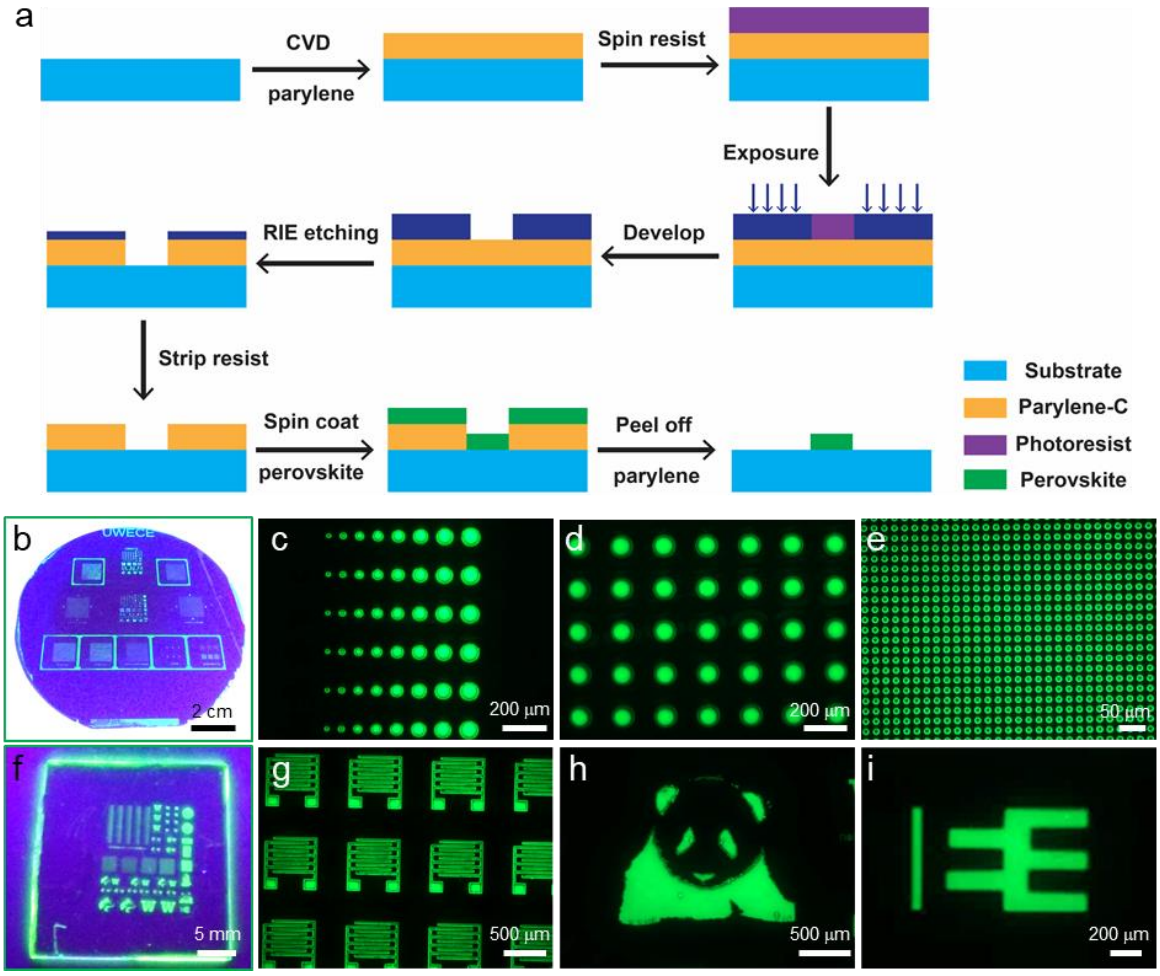

Figure 4.1. Photolithographic patterning of single-color perovskite films. (a) Schematic fabrication procedures for high-resolution photolithographic patterning of perovskite thin films. (b) and (f) Optical images of green perovskite patterns on a 4-inch silicon wafer and a 1-inch glass square under excitation from an UV lamp. (c) Perovskite circles with diameters varying from 20 to 90 μm. (d) Uniform arrays of 100 μm and (e) 10 μm perovskite circles (scale bar 50 μm). (g) Interdigitated electrode (IDE) patterns. (h) A cartoon image of a panda. (i) A UW EE department logo.

Figure 4.1(b), (f) show the optical images of perovskite patterns on a 4-inch silicon wafer and 1-inch glass substrates under ultraviolet (UV) lamp excitation. **Figure 4.1(c)-(e)** present fluorescent images of perovskite circles with different diameters. 10 μm circles were successfully achieved as shown in **Figure 4.1(e)**. Examples of an interdigitated electrode pattern, a cartoon image of a panda and the UW EE department logo are presented in **Figure 4.1(g)-(i)**. All these images show strong green luminescence with high color contrast, demonstrating the successful application of this dry lift-off process for patterning perovskites. Furthermore, using this protocol, we are able to achieve a high patterning resolution for perovskite films. The micro-patterning of features as small as 4 μm is possible (**Figure 4.2**). It can be clearly seen that there is almost no perovskite left for 1 μm line pattern (**Figure 4.2(a)**). The 2 μm micro-line pattern collapses with lines overlapping (**Figure 4.2(b)**). 4 and 6 μm mirco-line features can be easily distinguished, especially the latter shows a good line shape (**Figure 4.2(c)**). In **Figure 4.2(d)**, we show perovskite circle arrays with the diameters of 3 and 5 μm. The pattern of 3 μm circle array is very poor while the pattern of 5 μm circle array shows good round shapes.

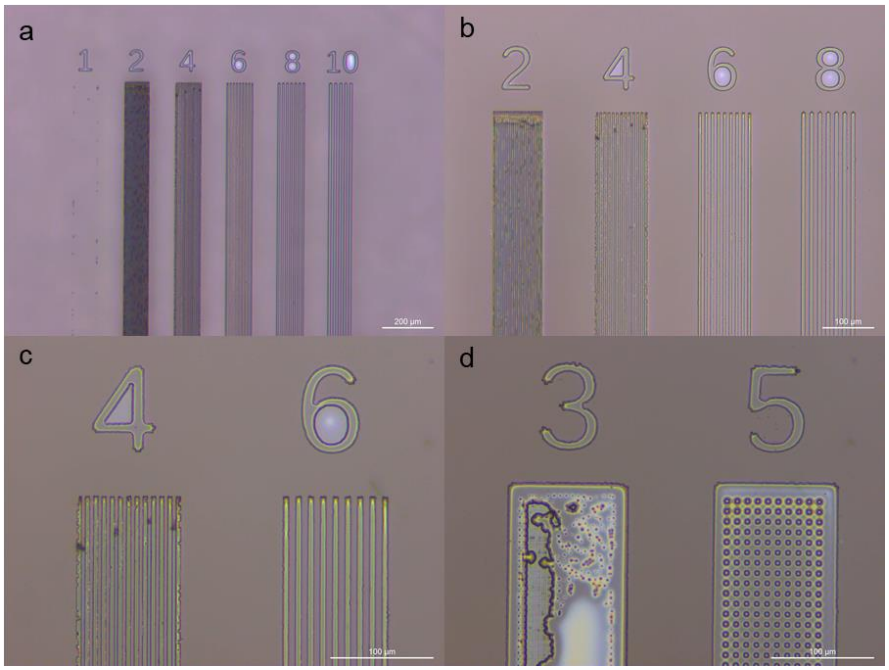

Figure 4.2. Patterning resolution of our approach for perovskite films. (a)-(c) Optical microscope images of perovskite micro-line patterns with different magnifications. The numbers represent the line width and spacing distance, ranging from 1 to 10 μm. (d) Perovskite circle array patterns. The numbers represent the diameter of the circle array (unit μm).

Although the demonstrations above were done using quasi-2D perovskites, our approach can be extended to other types of metal halide perovskites such as perovskite quantum dots (QDs)[83], vacuum-deposited perovskites[43]. We also examined the surface morphologies by atomic force microscope (AFM) and PL profiles of patterns made from quasi-2D, QD and vacuum-deposited perovskites, as shown in Figure 5.3. The quasi-2D perovskite circles were found to possess nest-like topography, where elevated rims are formed toward the circumference. Consequently, the PL intensity from the center is 60% of that from the edge. These results are consistent with the work reported by Lin *et al.*[161] The non-uniform topography is a common issue for spin-coating processes and depends on many parameters such as choice of solvent, solution viscosity, spin-speed and

dispense approach (static and dynamic dispense). It is interesting to note that perovskite QD circles show more uniform height and PL profiles compared to quasi-2D perovskites, which may be due to the different solvent used for these two perovskite solutions (hexane for perovskite QDs and DMSO for quasi-2D perovskites). To avoid the non-uniform topography from spin-coating processes, thermal evaporation was adopted to vacuum-deposited perovskite films. As a result, perovskite patterns from vacuum-deposition show uniform height and PL profiles.

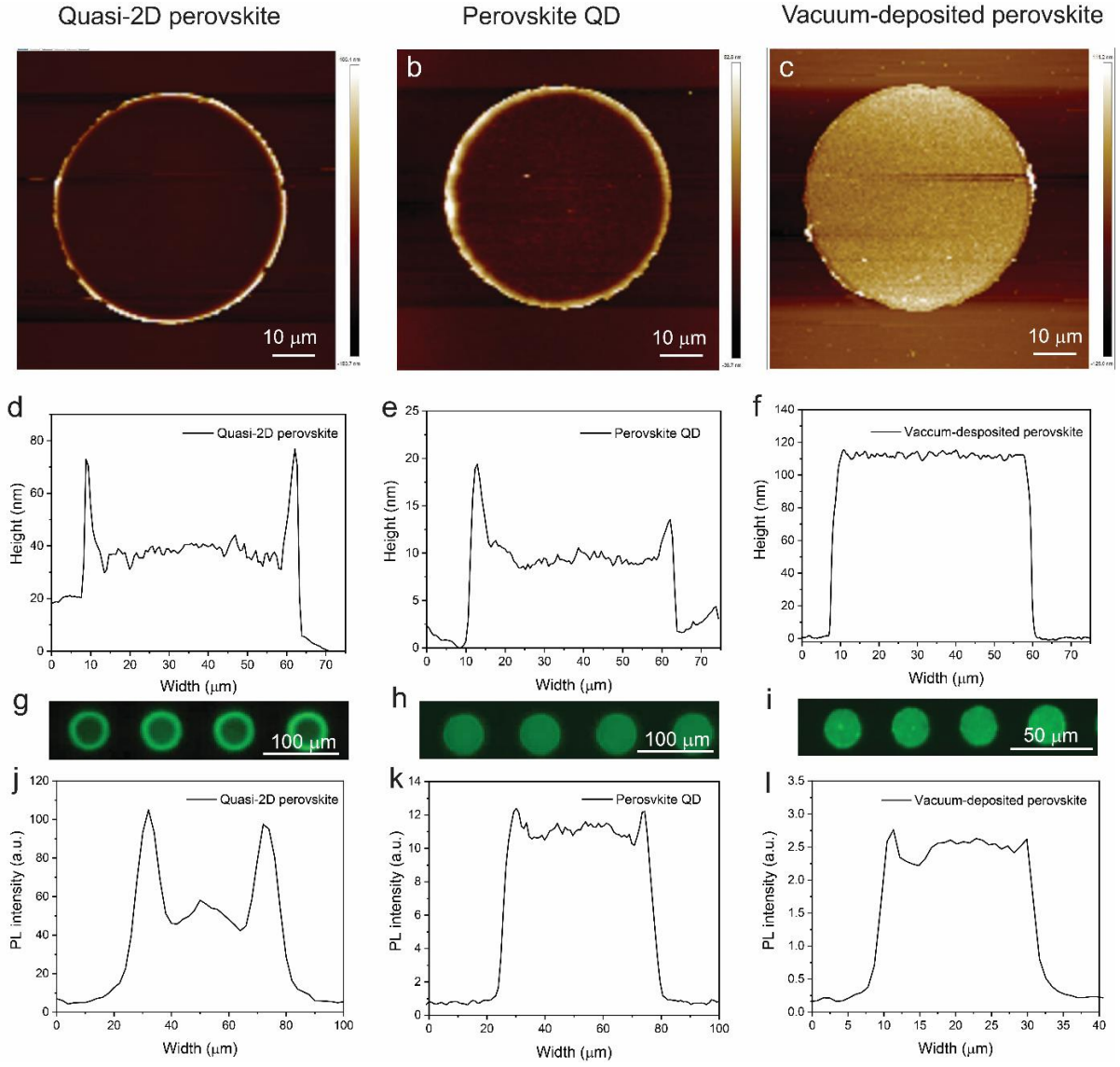

Figure 4.3. Surface morphologies and PL distributions of perovskite patterns. (a)-(c) AFM images of 50 μm circles for quasi-2D perovskites, perovskite QDs and vacuum-

deposited perovskites, respectively. (d)-(f) Corresponding height profiles of 50 um perovskite circles. (g)-(i) Magnified fluorescent images of perovskite circles. (j)-(l) Corresponding PL profiles of perovskite circles.

However, among these perovskite materials, quasi-2D perovskites are widely used in high-performance LED applications due to their high PLQY, good charge transport and simple preparation method.[100, 166, 167] We will use quasi-2D perovskite films in the following work unless otherwise specified.

Other color perovskite patterns have also been demonstrated in this work. RGB-emission perovskite films under UV excitation show strong PL for all these colors. Blue, green and red perovskite circles (50 μm diameter) are shown in **Figure 4.4(a)-(c)**. In addition, the University of Washington logos emitting blue, green and red light are displayed in **Figure 4.4(d)-(f)**. Blue and green perovskite patterns show strong luminescence with high color contrast while red ones suffer from relatively low contrast due to the environmental instability of red perovskites. **Figure 4.4(g)** shows blue, green and red perovskite emission spectra. The peak wavelength is 482, 523 and 670 nm for blue, green and red-emission perovskite thin films, respectively. The green perovskite films show the narrowest linewidth of ~17 nm while the linewidth is ~28 and ~38 nm for blue and red perovskite films, respectively. To demonstrate the potential of our approach for high-resolution displays. RGB 10 um circles were also successfully fabricated (**Figure A.3**), corresponding to a high-resolution of 1270 dots per inch (dpi).

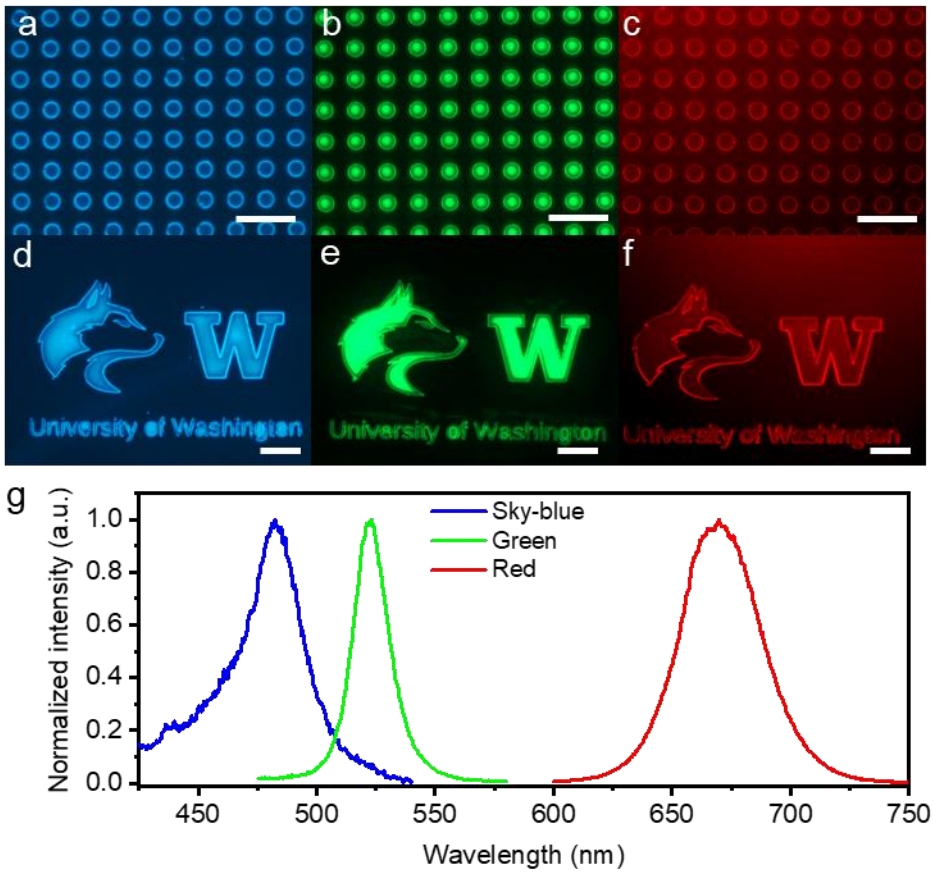

Figure 4.4. Perovskite RGB patterns and their PL spectra. (a)-(c) Blue, green and red perovskite circles (50 μm diameter). (d)-(f) University of Washington logos, scale bar 200 μm. g PL spectra of blue, green and red perovskite films.

4.4.2 *Multicolor patterns*

For commercial RGB displays, one solution is to fabricate green and red pixels together on one substrate with underneath blue backlight, this is widely used in LCD applications.[143, 148] The green and red-emission pixels could absorb blue light and convert it to green and red light, thus achieving real RGB displays.

Herein, we use standard photolithography with the demonstrated dry lift-off process twice to pattern green and red perovskite sequentially on a glass substrate. **Figure 4.5(a)** schematically

illustrates the fabrication procedures. The parylene and photoresist were sequentially deposited onto the substrate with prefabricated green perovskite patterns. The standard photolithography and RIE were used again to generate patterned trenches in the parylene film. The red perovskite precursor was spin-cast and annealed for a short time. After peeling off the parylene film, multicolor perovskite patterns were successfully formed. **Figure 4.5(b)** displays the uniform array of alternative green and red perovskite circles, each circle has a diameter of ~50 μm. The magnified fluorescent image is shown in **Figure 4.5(c)**, the second photolithography and lift-off processes did not affect the prefabricated green perovskite patterns due to the excellent sealing of parylene films. The perovskite films covered by parylene could even survive in acetone solution for several days. We also measured the overall PL spectrum contributed by both green and red perovskite circles at the same time (**Figure 4.5d**). The overall PL from multicolor patterns shows two emission peaks located separately at green and red wavelength regions. The peak PL intensity of green perovskite patterns is about 2.5-fold as high as that of red ones. This difference can be easily understood considering the relatively poor PLQY and stability of red-emission perovskites which include more iodine halides. **Figure 4.5(e)** shows the PL spectra of green perovskite patterns before and after the second patterning process. No peak wavelength shift is observed, and only a slight drop of PL intensity is seen after going through the second patterning process.

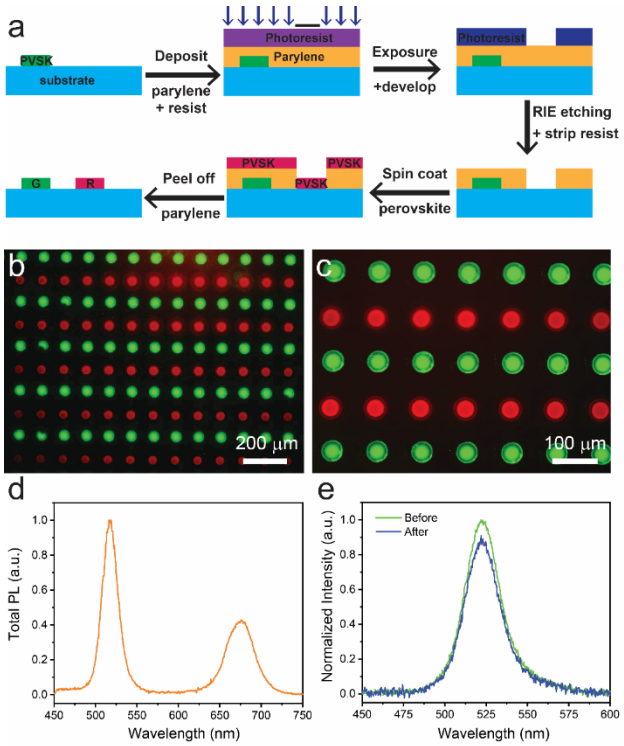

Figure 4.5. Multicolor perovskite patterns on a single substrate. (a) Schematic fabrication procedures of multicolor perovskite patterns. (b) Fluorescent microscope image of green and red perovskite circles with a diameter of 50 μm. (c) Higher-magnification fluorescent image of the dual-color patterns. (d) Overall PL spectrum of the dual-color perovskite patterns. (e) PL spectra comparison of green perovskite patterns before and after the second patterning process.

To further verify our approach is effective and non-intrusive, we measured the absolute PLQY evolution of green perovskite films during multicolor patterning processes (**Figure A.4**). The PLQY remains essentially the same after the first patterning process, and only slightly drops from 69 ± 7% to 62 ± 8% after the second patterning process. This is likely due to the degradation of perovskite patterns caused by long-time exposure to environment moisture and resist baking in the second photolithography process. These results indicate our approach preserves the properties of prefabricated perovskite patterns properly and thus multiple patterning processes are feasible.

4.4.3 *Perovskite mirco-LED displays*

Another solution for achieving RGB displays is to develop self-emissive arrays of RGB pixels under the current-driving mode.[142, 143] The emission of the display is controlled by the current flowing to individual pixels through a TFT back plane. Nowadays, this solution has been widely adopted in commercial LED TVs. Through the proposed photolithographic method with dry lift-off, we successfully demonstrated a green pixelated perovskite micro-LED array for the first time, to the best of our knowledge.

Figure 4.6(a) schematically depicts the structure of PeLEDs with green pixels. To avoid the current shunt path between the cathode and anode, an insulating layer (SiO_2) was deposited and etched to separate PeLED pixels. The functional layers including poly(3,4-ethylenedioxythiophene) polystyrene sulfonate (PEDOT:PSS), perovskite and 2,2',2''-(1,3,5-Benzinetriyl)-tris(1-phenyl-1-H-benzimidazole) (TPBi) were patterned based on above-mentioned photolithographic method. Finally, the top electrode was deposited to finish fabrication. The energy level diagram of PeLEDs is shown in **Figure 4.6(b)**, the electrons and holes are injected from indium tin oxide (ITO) and Aluminum (Al) respectively and recombine in the perovskite layer to emit photons. **Figure 4.6(c)-(e)** displays various current-driving PeLED patterns including an array of 20 μm-diameter circles, an array of 30 μm square patterns and a University of Washington logo. These images were obtained by an optical microscope in dark field. Uniform electroluminescence (EL) from PeLED pixels were observed. **Figure 4.6(f)** shows the EL spectra of pixelated PeLEDs at various biases from 3 to 5 V. The EL spectra exhibit a narrow linewidth of 19 nm, indicating a high color purity of PeLEDs which is of importance in display applications. The inset photo in **Figure 4.6(f)** shows a green-emission PeLED with many squared subpixels operated at a bias of 4 V. The device exhibits great emission homogeneity without any obvious

dead pixels, just like a single unit. Pixelated PeLEDs with blue and red emission can be fabricated in a similar approach based on our proposed method.

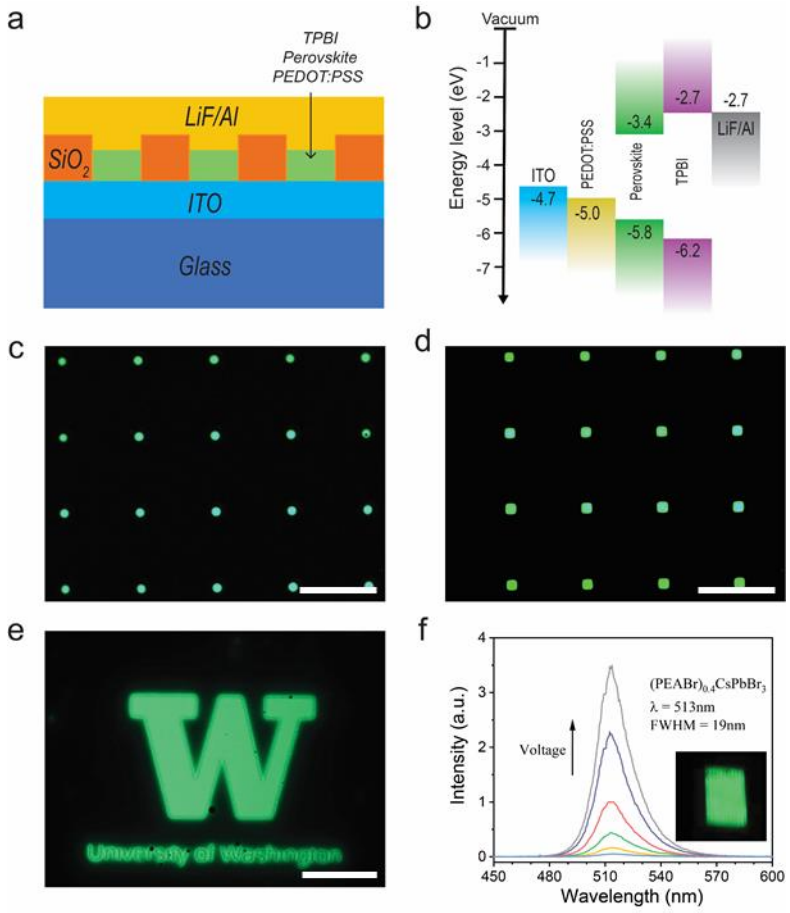

Figure 4.6. Prototype perovskite micro-LED array. (a) Schematic structure of pixelated PeLEDs. (b) Energy level diagram. (c)-(e) Optical microscope images (in dark field) of electrically driven perovskite patterns, the scale bar is 200 μm. (c) 20 μm-diameter circles, (d) 30 μm-size squares and (e) University of Washington logo. (f) EL spectra of pixelated PeLEDs at various voltages from 3 to 5 V. The inset photograph shows a large emitting area (2 × 2 mm2) with patterned perovskite squares.

The performance of the pixelated PeLEDs (30 μm-size square array with 100 pixels) was further characterized. **Figure 4.7(a)** shows the luminance (*L*)-current density (*J*)-voltage (*V*)

characteristics. The current density and luminance were calculated based on the total area of PeLED pixels. It is clearly observed that the devices show typical diode characteristics, the current density increases exponentially with voltage. The turn on voltage of the devices is determined to be about 3.4 V (defined as the voltage at which a luminance of 1 cd/m^2 is obtained). The maximum luminance of 13043 cd/m^2 is achieved at 8.4 V, and the luminance starts to decrease after that because of Joule heat and Auger recombination. The dependence of EQE and current efficiency on current density is shown in **Figure 4.7(b)**. The device exhibits a maximum EQE of 1.24%, current efficiency of 3.85 cd/A and luminous efficiency of 1.86 lm/W.

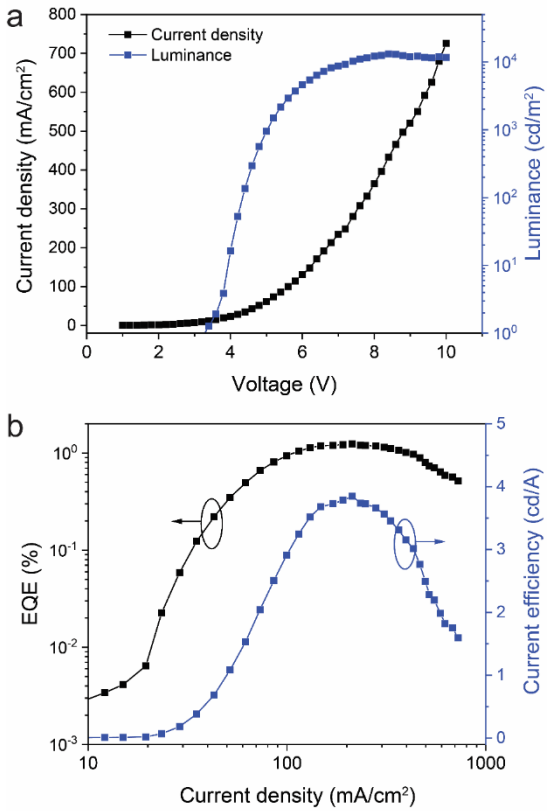

Figure 4.7. Performance characterization of pixelated PeLEDs. (a) L-J-V characteristics. (b) The plot of EQE and current efficiency versus current density.

However, in comparison, reference PeLEDs (non-patterned) show a peak EQE of 3.9%. To analyze this difference, we compared the performance of devices that went through various

processing steps. As shown in **Figure 4.8**, All devices show typical diode characteristics with current density and luminance increases dramatically after turn-on voltage. The peak EQE for reference, patterned parylene and pixelated devices is 3.9%, 3.1% and 1.2%, respectively.

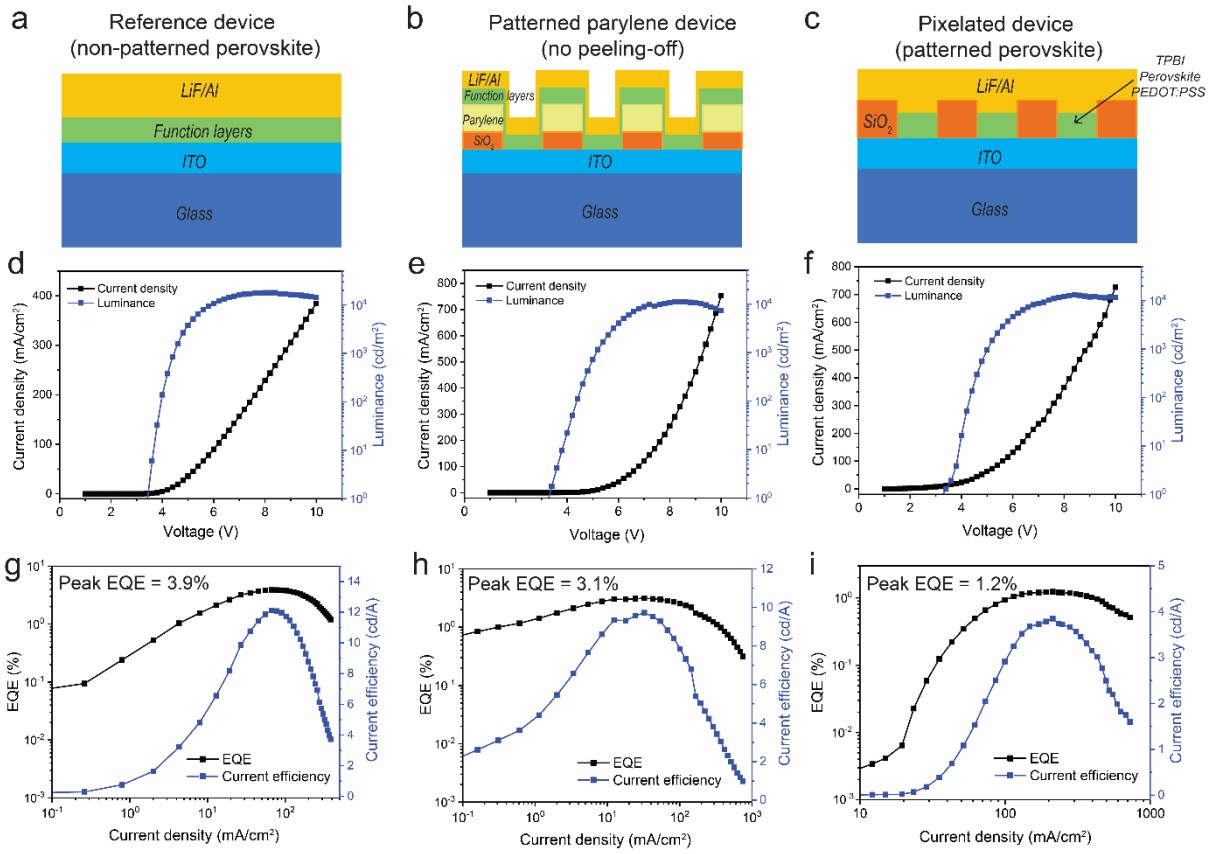

Figure 4.8. Performance characterization of pixelated devices undergoing various processing steps. (a)-(c) Schematic structures of reference, patterned parylene and pixelated devices. The functional layers include PEDOT:PSS, perovskite and TPBi. The reference devices are conventional planar-type PeLEDs without patterning perovskite films. The patterned parylene devices have patterned parylene films and all function layers deposited. The parylene films are not peeled off before depositing the top electrode, which is the main difference from final pixelated devices. (d)-(f) *L-J-V* curves and (g)-(i) the dependences of EQE and current efficiency on current density for corresponding devices that went through various processing steps.

We further compare the *J-V*, *L-V* and *EQE-J* curves of these three devices as shown in **Figure 4.9**. The patterned parylene devices show a peak EQE of 3.1%, close to that (3.9%) of reference devices. In addition, both devices show similar *L-J-V* curves with low leakage current. The pixelated devices show a lower peak EQE of 1.2%, and the *J-V* curve shows distinct characteristics compared to those of the other two devices. Specifically, the current density of the pixelated devices is higher at 1-4 V and the transition of typical diode turn-on behavior is ambiguous. We also notice that the pixelated LEDs achieve the peak EQE at a higher current density (213 mA/cm^2) and show worse efficiency roll-off characteristics compared to the reference and patterned parylene devices. We attribute these phenomena to higher leakage currents in pixelated devices, likely caused by imperfect pixel edges after dry lift-off process and a few possibly existing poor pixels. Further optimization should be focused on improving the thickness uniformity of patterned perovskite pixels and reducing the pixel edge flaws to minimize the leakage current.

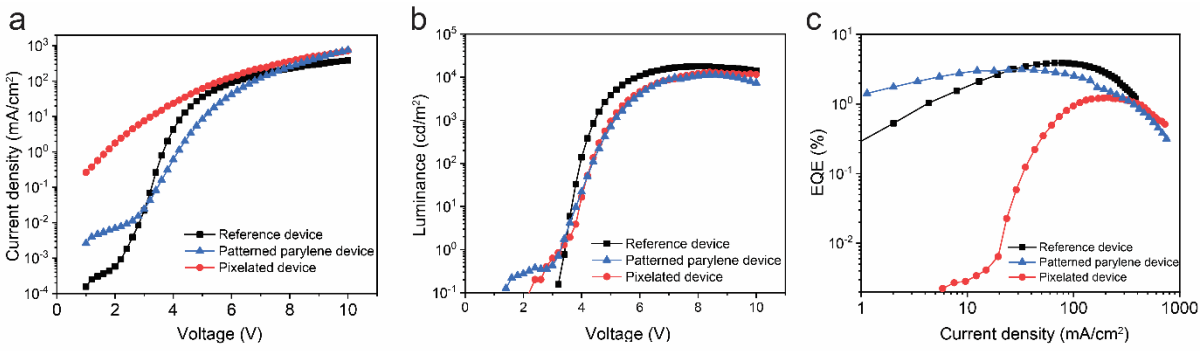

Figure 4.9. Performance comparisons of reference, patterned parylene and pixelated devices. (a) current density *versus* voltage, (b) luminance *versus* voltage and (c) EQE *versus* current density for reference, patterned parylene and pixelated devices.

4.5 CONCLUSION AND OUTLOOK

In summary, we have succeeded in developing a high-resolution, large-area photolithographic method to pattern perovskite thin films using parylene as an intermediary. The utilization of parylene enables a dry lift-off process where unwanted perovskite is mechanically lifted off without the aid of orthogonal solvents. Based on this approach, RGB single-color patterns have been successfully fabricated. Thus far, the highest pattern resolution we can achieve is down to 4 μm. The parylene films are also able to protect the perovskite films underneath well, enabling multicolor perovskite patterns by using the standard photolithography process multiple times. Finally, an electrically driven green perovskite display consists of a perovskite micro-LED array has been demonstrated with high color purity and contrast. The pixelated PeLEDs show a peak EQE of 1.24% and maximum luminance of 13043 cd/m^2.

We have also demonstrated our photolithographic patterning approach is generic and can be applied to various types of metal halide perovskites including quasi-2D perovskites, perovskite quantum dots[83], vacuum-deposited perovskites[43]. Our work demonstrates the feasibility of patterning multicolor perovskite thin films and supports the promising potentials of perovskites for commercialized multicolor displays.

Chapter 5. OPTICALLY PUMPED PEROVSKITE LASERS

Adapted with permission from:
Huang, C.Y., Zou, C., Mao, C., Corp, K.L., Yao, Y.C., Lee, Y.J., Schlenker, C.W., Jen, A.K. and Lin, L.Y. $CsPbBr_3$ perovskite quantum dot vertical cavity lasers with low threshold and high stability. *ACS Photonics*, *4*(9), pp.2281-2289. Copyright 2017 American Chemical Society

5.1 PEROVSKITE QUANTUM DOT VCSELS

5.1.1 *Abstract*

All-inorganic cesium lead bromide ($CsPbBr_3$) perovskite quantum dots (QDs) have recently emerged as highly promising solution-processed materials for next-generation light-emitting applications. They combine the advantages of QD and perovskite materials, therefore have strong potentials in achieving high optical gain with high stability. Here, we report an ultralow lasing threshold (0.39 μJ/cm^2) from a hybrid vertical cavity surface emitting laser (VCSEL) structure consisting of a $CsPbBr_3$ QD thin film and two highly reflective distributed Bragg reflectors (DBRs). Temperature dependence of the lasing threshold and long-term stability of the device were also characterized. Notably, the $CsPbBr_3$ QDs provide superior stability and enable stable device operations over 5h/1.8 × 10^7 optical pulse excitations under ambient conditions. This work demonstrates the significant potential of $CsPbBr_3$ perovskite QD VCSELs for highly reliable lasers under not only short pulse (femtosecond) but also quasi-continuous-wave (nanosecond) operations.

5.1.2 *Introduction*

Over the past few years, solution-processed organic-inorganic halide perovskite materials such as $APbX_3$ (A = methylammonium (MA) or formamidinium (FA); X = Cl, Br, or I), have emerged as a compelling newcomer among photonic materials, particularly for photodetection and

photovoltaic applications.[2, 168-171] These materials exhibit high carrier mobility,[172] sharp optical absorption edges and high photovoltaic efficiency,[173] as well as an unusual defect tolerance.[174] The unique optoelectronic properties have led to record certified research solar cell power conversion efficiencies as high as 22.1%.[118] More recently, the application of perovskites as light-emitting materials[3, 23, 175, 176] has given rise to new prospects for light emitting diodes (LEDs),[177, 178] amplified spontaneous emissions (ASE)[179-181] and lasing.[11, 13, 182-186] However, a major concern for these perovskite materials is their poor stability upon exposure to moisture, thermal stress, and light.[187, 188] This remains an impediment for realizing practical and commercial perovskite-based optoelectronic devices. As a result, many research efforts have been devoted to improving the stability of perovskite devices.[189, 190]

To address the aforementioned issues, an alternate approach is to abandon the organic cation by replacing MA or FA with Cesium (Cs). This kind of cation engineering, yielding a perovskite-like thin film structure, has been employed for both LEDs and lasers.[123, 191-195] The quantization of their electron energy levels also implies narrow emission linewidths and broad wavelength tunability. To integrate high stability with the merits of quantum confinement, all-inorganic $CsPbBr_3$ QDs and nanowires have been synthesized and employed for ASE and lasing.[179, 181, 192, 196] However, these studies focused chiefly on the gain media without integrating external resonant cavities. Most recently, a $CsPbBr_3$ vertical cavity laser with 9 $\mu J/cm^2$ lasing threshold was reported.[197] A well-designed resonant cavity is a critical step to achieve lasing in single-mode Gaussian beam with high directionality, which is important for optoelectronic integrated circuits, especially for optical communication applications.

In the last three decades, there have been significant advances in vertical cavity surface emitting lasers (VCSELs), which have attracted wide attention owing to their low lasing threshold,

low beam divergence, circular beam profile and simplified two-dimensional array architecture compared to edge-emitting lasers.[198-200] The laser cavity consists of two highly reflective distributed Bragg reflector (DBR) mirrors parallel to each other and a gain medium sandwiched in between for stimulated emissions. Most of the VCSELs that have been demonstrated use quantum well structures as the gain medium layer. More recently, colloidal semiconductors QDs have been applied to VCSELs in the visible wavelength range.[201] Semiconductor QDs can reduce the temperature sensitivity of lasing threshold compared to quantum wells due to their high, delta-function-like density of states profile. Light in the green-wavelength region (typically 500 ~ 550 nm) induces maximum luminous sensation for human eyes and thus has a wide range of applications. However, to achieve VCSELs emitting green wavelengths at room temperature has been a challenge (the so-called green gap).[202] Green lasers in general are produced through frequency-doubling technologies which typically have low efficiencies.

In this work, we explore a strategy for improving the lasing threshold and stability of perovskite lasers by combining a surface-emitting vertical resonant cavity with CsPbBr3 QDs. The hybrid-integrated perovskite laser, with an emission wavelength of 522 nm, achieved an ultralow lasing threshold of 0.39 μJ/cm2, which further facilitates long-term stability. The device maintained its performance over 1.8 × 107 optical pulse excitation cycles in a duration of over 5 hours.

5.1.3 *Methods*

Device Fabrication. Commercial-available distributed Bragg reflector (DBR) mirrors (FD1M) with ~99.5% reflection for 510 nm were purchased from Thorlabs. A set of DBR mirrors were cleaned sequentially with acetone, isopropanol and deionized water under sonication for 10 minutes, respectively. Afterwards, the cleaned mirrors were treated with oxygen plasma for 10

minutes before spin-coating process. To form highly smooth thin films, $CsPbBr_3$ QDs solution was spin-coated onto one mirror at 1000 rpm for 45s. To complete the VCSEL structure, the other DBR mirror was bonded to the as-coated mirror with optical epoxy at the peripheral. Finally, the device was pressed under a heavy load to minimize the air gap in the cavity during the drying process of optical epoxy for 24h. **Figure 5.1** exhibits the schematic device structure and the transmission spectrum of the commercial DBR mirror.

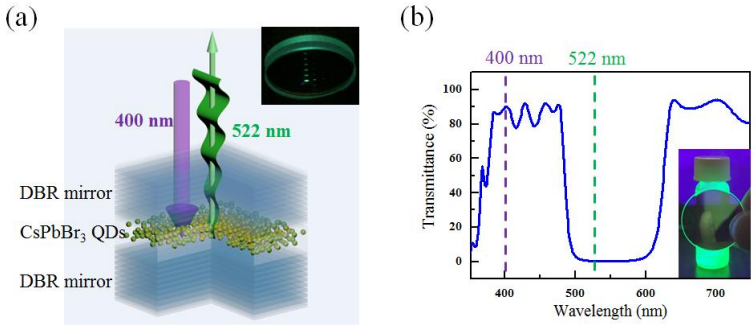

Figure 5.1. $CsPbBr_3$ QD VCSEL based on a DBR cavity. (a) Schematic structure of the $CsPbBr_3$ QD VCSEL. Inset: photograph of the device in operation. (b) Transmittance spectrum of the DBR mirror. Inset: photograph of the mirror in front of an excited $CsPbBr_3$ QD solution. The DBR mirror reflects the green PL while passing the UV excitation light.

Synthesis of $CsPbBr_3$ Quantum Dots (QDs). Cesium carbonate (Cs_2CO_3, 99.9% trace metals basis), Lead (II) bromide ($PbBr_2$, 98%), octadecene (ODE, technical grade 90%), oleylamine (OLA, technical grade 70%), n-octane (≥ 99%) were purchased from Sigma-Aldrich. Oleic acid (OA, technical grade 90%), ethyl acetate (≥ 99.5%) were purchased from Alfa Aesar. For the synthesis of Cs-oleate, 0.326 g Cs_2CO_3 (1 mmol) was loaded into a 100 mL, 3-neck flask along with 18 mL octadecene and 1 mL oleic acid. The mixture was dried for 30 mins at 100 ˚C, and then heated under N_2 flow to 150 ˚C until all Cs_2CO_3 have reacted with OA. The clear solution was kept at 150 ˚C to prevent the solidification of Cs-oleate solution. For the synthesis of $CsPbBr_3$

QDs, 66.7 mg of $PbBr_2$ (0.18 mmol) was loaded into a 25 mL 3-neck flask along with 5 mL ODE, 1 mL OLA and 0.5 mL OA. The mixture was dried for 10 mins at 100 ˚C and then heated to 150 ˚C under N_2 until a clear solution was obtained. After the $PbBr_2$ salt had dissolved completely, the temperature was raised to 170 ˚C and then as-prepared Cs-oleate solution was swiftly injected. Within seconds, the final solution was cooled down to room temperature by an ice-water bath. To purify the particles, excess amount of ethyl acetate was added into the crude solution. The precipitate was collected by centrifugation and re-dispersed in n-octane. The process was repeated for several times and the final product was dispersed in n-octane. Before use, $CsPbBr_3$ QDs solution was filtered by a 0.45μm pore size poly (tetrafluoroethylene) filter to remove precipitations and impurities.

Material Characterization. Powder X-ray diffraction (XRD) patterns of $CsPbBr_3$ QDs deposited on a Si substrate were recorded using Bruker F8 Focus power XRD with monochromatized Cu Kα radiation (λ = 1.5418 Å). Transmission electron microscopy (TEM) and high-resolution TEM (HRTEM) were performed on Tecnai G2 F20 operating at 200kV. UV-Visible absorption spectra of the films were measured with Varian Cary 5000 UV-vis-NIR Spectrophotometer. Steady-state photoluminescence (PL) emission spectra were acquired using a spectrofluorometer (Fluorolog FL-3, Jobin Yvon Horiba) with xenon short arc lamp as the light source. For $CsPbBr_3$ QDs thin film, the time-resolved PL measurements were performed using a time-correlated single-photon counting (TCSPC) system (FluoTime 100, PicoQuant) while the perovskite thin film was photo-excited by a pump laser source (405 nm, 60 ps, 40 MHz) from PicoQuant.

Device Characterization. A femtosecond Ti:Sapphire laser (Coherent, Inc) with a frequency-doubling external beta barium borate crystal (400 nm, 50 fs, 1kHz) and a nanosecond Nd:YAG

laser (355 nm, 5 ns, 10 Hz) were used as the pump sources. For the steady-state PL and lasing measurement, a home-built micro-PL system was utilized and the luminescence was recorded by a micro-spectrometer (OSM-100, Newport) and a spectrometer (iHR550, HORIBA JOBIN YVON) equipped with a CCD detector cooled by liquid nitrogen, respectively. For time-resolved spectrogram and PL decay, the emission was collected using a Hamamatsu streak camera (C10910) with the synchroscan attachment (M10911-01). All of the aforementioned measurements were conducted at room temperature. Low temperature measurements were conducted in a cryostat from Janis Research Inc. The VCSEL device temperature could be adjusted from 120 K-295 K with high precision.

5.1.4 *Results and discussion*

To characterize the QD perovskite material, we first use X-ray diffraction (XRD) and transmission electron microscopy (TEM). The XRD pattern of $CsPbBr_3$ QDs is shown in **Figure 5.2(a)**. The single peak at 2θ equal to 30.69° can be indexed to the (200) plane of $CsPbBr_3$, which matches well with the cubic perovskite crystal structure of Pm3m. **Figure 5.2(b)** shows the TEM image of perovskite QDs. The monodisperse $CsPbBr_3$ QDs have an average diameter of 10 nm, with a cubic shape. The optical properties of the $CsPbBr_3$ QDs are first characterized by measuring the absorption and photoluminescence (PL) spectra. **Figure 5.2(c)** shows typical measured ultraviolet-visible (UV-Vis) absorption and PL spectra of the $CsPbBr_3$ QD thin film. The absorption edge and PL peak are located at ~460 nm and 510 nm, respectively. The PL spectrum shows a narrow linewidth with a FWHM of ~22 nm.

Time-resolved PL (TRPL) is a common tool to characterize the excited carrier dynamics in relation to the pumping intensity. **Figure 5.2(d)** exhibits the spectrally integrated PL decay traces from the $CsPbBr_3$ QD thin film under various pump fluences. Under excitation fluence far below

ASE threshold, the PL decay curve follows a single exponential decay (red trace), consistent with single exciton recombination. With increasing excitation fluence, a fast decay process occurs (green trace), which corresponds to the fast Auger recombination. The lifetime of fast Auger recombination and slow single exciton recombination is obtained by fitting the PL decay curve with a bi-exponential decay function. From the best-fitting result, we obtained an Auger recombination lifetime of ~180 ps and a single-exciton recombination lifetime of ~ 4 ns. Well above the ASE threshold, an ASE lifetime of 30 ps could be estimated from the PL decay (blue trace), again by bi-exponential fitting, which is comparable to other published results.[181]

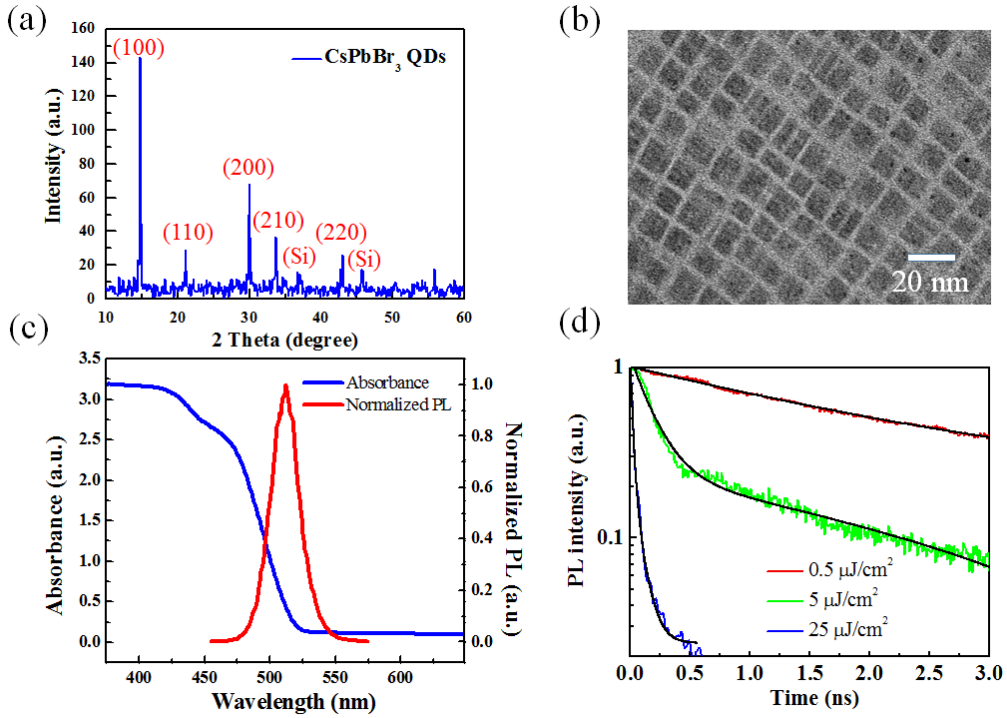

Figure 5.2. Characterizations of $CsPbBr_3$ QD films. (a) XRD pattern of the $CsPbBr_3$ QD film. (b) TEM image of monodisperse $CsPbBr_3$ QDs. (c) UV-Vis absorption and photoluminescence spectra of $CsPbBr_3$ QDs. (d) Time-resolved photoluminescence measurements from the $CsPbBr_3$ QDs film under different pump intensities.

To explore the ASE performance, the closely packed thin film with a thickness of 240 nm was pumped by a femtosecond laser at a wavelength of 405 nm. The pumping configuration was a standard stripe excitation reported elsewhere.[203] The results are presented in **Figure A.5**. At low pump fluence (< 5.6 μJ/cm^2), the spectra exhibit the characteristics of broad spontaneous emission with a linewidth of ~22 nm. As the pump fluence increases above 5.6 μJ/cm^2, a narrower emission band with a linewidth of 7-8 nm starts to emerge at the wavelength of ~524 nm, which is red-shifted by about 14 nm compared to the PL peak. The onset of ASE in the QD thin film is observed with an immediate output intensity increase at the threshold of about 5.6 μJ/cm^2. The linewidth narrowing and lifetime shortening above the threshold are also readily observed. These results are clear signatures that indicate the transition from spontaneous emission (SE) to ASE at the threshold of 5.6 μJ/cm^2.

The deterministic characteristics of lasing are represented by the dependence of laser emission spectrum and output optical intensity on the pump fluence. A femtosecond Ti:Sapphire laser with 400 nm wavelength, 50 fs pulse width and 1kHz repetition was first used as the pump source. **Figure 5.3(a)** shows the PL spectra at different pump fluence. The inset shows the image of the laser output obtained by a CCD camera. Below lasing threshold, the emission is fully blocked by the DBR mirror and there is no signal detected by the CCD camera. As the pump fluence increases, a narrow peak at λ= 522 nm starts to emerge (FWHM line width Δλ= 0.9 nm), which red-shifts 12 nm relative to the PL peak. The red-shift originates from biexciton recombination. Beyond lasing threshold, the rate of emission through biexciton recombination increases significantly, which greatly benefits stimulated emission over spontaneous recombination. The resonant cavity is designed to match this shift. The output intensity versus input pump fluence (L-L curve) measurement result is shown in **Figure 5.3(b)**. The plot of *L-L* curve exhibits abrupt rising at ~0.39

μJ/cm2, further confirming lasing operation beyond this threshold. To gain a deeper insight into our device, we performed PL dynamics measurement on the $CsPbBr_3$ QD VCSEL well above the lasing threshold at 5 μJ/cm^2. **Figure 5.3(c)** shows the time-resolved spectrogram obtained using a streak camera. The corresponded time-resolved PL intensity decay trace is plotted in **Figure 5.3(d)**. The fast decay (~ 10 ps) at peak wavelength (522 nm) indicates that the emission is mainly through a stimulated process, which provides further confirmation on lasing operation of the device. The observed decay time is limited primarily by the resolution of the streak camera.

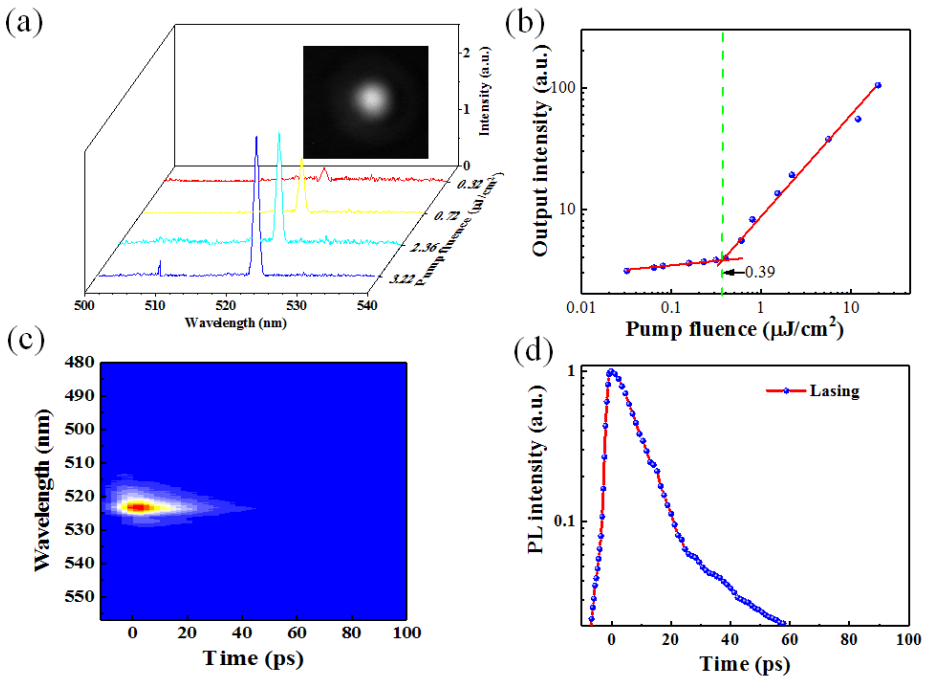

Figure 5.3. Performance characterizations of the CsPbBr3 QD VCSEL under fs-pulse pumping. (a) Pump-fluence dependence of the emission spectrum from the CsPbBr3 QD VCSEL. Inset: Far-field image of the emission from a $CsPbBr_3$ QD VCSEL with pumping fluence above the lasing threshold. (b) L-L curve for the $CsPbBr_3$ QD VCSEL, demonstrating lasing with a threshold of 0.39 μJ/cm^2. (c) Spectrogram and (d) PL time response above the lasing threshold. The device was excited at λ= 400 nm with 50 fs laser pulses

To characterize the laser beam quality, we measured the intensity distribution of the laser beam along x and y direction at 10 cm from the output of DBR mirror. **Figure 5.4(a)** shows the measurement result. The corresponding beam profiles along x- and y-direction are shown in **Figure 5.4(b)** and **(c)**, respectively. The results fit well with a TEM_{00} Gaussian beam (R-squared value is ~0.99), demonstrating single-mode operation with high optical beam quality. The FWHM linewidths for x and y direction are 2.41° and 2.72°, respectively, indicating small beam divergence from our $CsPbBr_3$ QD VCSEL.

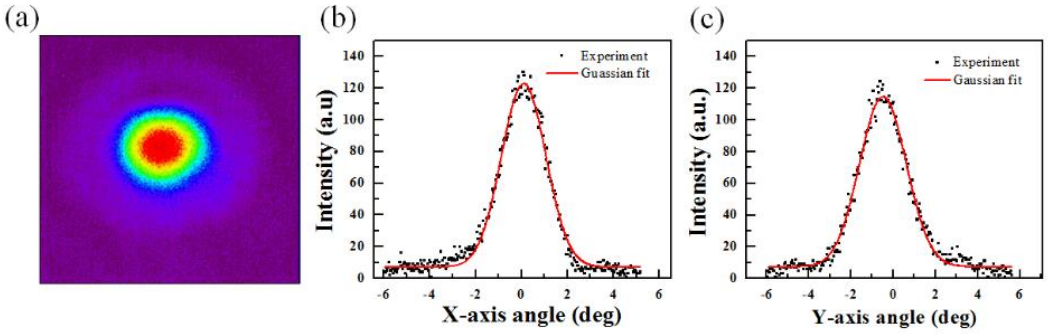

Figure 5.4. Output beam profile of the $CsPbBr_3$ QD VCSEL. (a) Intensity distribution of the laser emission at 20 cm from the output DBR mirror. (b) Gaussian fitting along the X direction and (c) Gaussian fitting along the Y direction. R-squared value is ~0.99.

For long-term applications, lasers operating under continuous wave (CW) pumping are strongly preferred. In this condition, self-heating under high pumping intensity is a major concern as it may prevent the device from lasing. This is due to the increased Auger recombination rate when the pump duration becomes longer than the stimulated emission lifetime. In addition to local heating, non-radiative Auger recombination in perovskite QDs may also lead to reduced quantum efficiency and flickered fluorescence emission.[192] In order to probe the potential for CW operation, while still being able to achieve sufficient pump intensity, a quasi-CW pulsed laser with pulse

duration much longer than Auger lifetime is often utilized.[192, 204] We used a nanosecond Nd:YAG laser (355 nm wavelength, 5 ns pulse duration, 10 Hz repetition) to perform such characterizations. The emission spectra from the $CsPbBr_3$ QD VCSEL under different pump fluences are shown in **Figure 5.5(a)**. The output optical intensity versus the pump fluence is shown in **Figure 5.5(b)**. The narrow emission peaks and the kink in the L-L curve due to transitioning from spontaneous emission into stimulated emission indicate that lasing can still be achieved under such quasi-CW operation. The estimated lasing threshold is 98 $\mu J/cm^2$, which is significantly higher than the 0.39 $\mu J/cm^2$ threshold under fs pulse pumping. This may be attributed to the insulating shell of ligands on the QD surface, which can cause larger thermal load while the device is under CW operation. To address this issue in the future, a possible approach is to perform a ligand exchange to replace long carbon bonds (oleic acid) with short carbon bonds (caprylic acid), which should not affect the dispersion of QD solutions.[205]

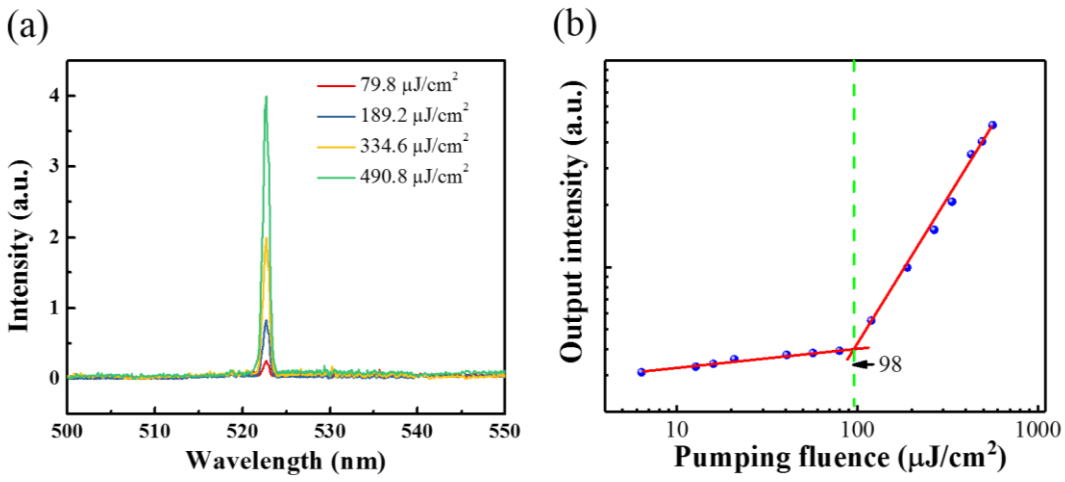

Figure 5.5. Performance characterizations of the $CsPbBr_3$ QD VCSEL under ns-pulse pumping. (a) Evolution of the emission spectra with increasing pump fluence for the $CsPbBr_3$ QD VCSEL. (b) L-L curve for the $CsPbBr_3$ QD VCSEL, showing a lasing threshold at 98 $\mu J/cm^2$. The device was excited at λ = 355 nm with 5 ns laser pulses.

To study the temperature dependence of lasing threshold, the L-L curves of the $CsPbBr_3$ QD VCSEL were recorded under various temperatures from 120 K to 295 K. The femtosecond pulsed laser was used as the pump source. **Figure 5.6(a)** shows the experimental results. The lasing threshold decreases steadily with decreasing temperature, and ultimately reaches 0.15 $\mu J/cm^2$ at 120 K. This is believed to be due to the combination of increased radiative recombination rate and decreased Auger recombination loss.[206] It's worth noting a difference in temperature dependence between $MAPbX_3$ thin films and $CsPbBr_3$ QDs. The $MAPbX_3$ thin films undergo a phase transition from tetragonal to orthorhombic as the temperature decreases below 160K, which leads to a sudden increase in the bandgap.[207] Consequently, the gain spectrum blue-shifts out of the wavelength range for cavity modes, resulting in laser emission disappearance below 160 K.[11] On the other hand, our $CsPbBr_3$ QD laser can still achieve lasing with decreasing threshold and the emission peak wavelength changes by a small amount of ~2 nm even when the temperature decreases below 160 K. We define an 80%-lifetime (T_{80}) as the time when the output intensity decreases to 80% of the initial intensity. As shown in **Figure 5.6(b)**, the device under fs pump pulses exhibits higher stability (T_{80} > 5h/1.8 × 10^7 pump pulses) while the output intensity decreases significantly faster under ns pulse pumping (T_{80} ~ 2h).

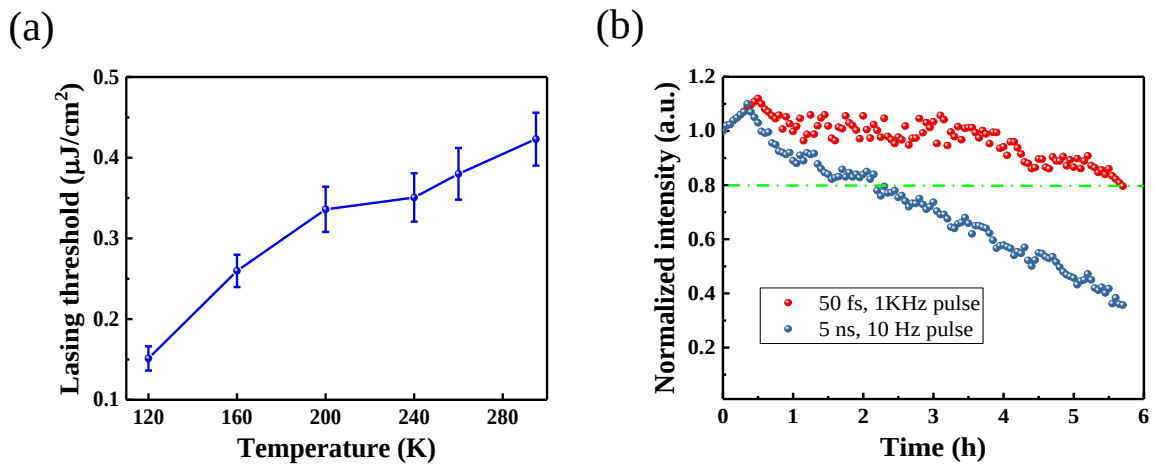

Figure 5.6. Temperature dependent lasing threshold and pulse-duration dependent stability. (a) Lasing threshold fluence as a function of temperature for the $CsPbBr_3$ QD VCSEL. (b) Stability characterizations of the device under fs (red) and ns (blue) pulsed excitation with pump fluences set at 1.1 P_{th}. The measurements were performed at room temperature under ambient conditions.

5.2 Perovskite Distributed Feedback (DFB) Laser

In order to achieve electrically pumped perovskite laser, we first need to demonstrate optically pumped perovskite. Population inversion under optical pumping condition and high-quality cavity are necessary requirements for optically pumped laser. We utilize the second order distributed feedback (DFB) grating as the cavity to provide the resonance condition. The schematic structure of our perovskite DFB laser is illustrated in **Figure 5.7(a)**. The substrate is silicon with 1 um SiO_2, the periodic gratings were fabricated by e-beam lithography with 280 nm period, 50% duty cycle and 60 nm depth. Then a $MAPbBr_3$ perovskite film was spin-coated onto the grating structure. We used 3.5 ns pulse laser with 337 nm wavelength to pump the device and collected the top emission. The experimental setup is shown in **Figure 5.7(b)**. The back focal plane (BFP) of the objective lens, lens 1 (L_1), lens 2 (L_2) and the CCD camera form the 4*f* system to record the BFP images of

our perovskite laser devices. The spectrometer is located at the focal point of L_1 to detect the spectrum of emission beam from our devices. To fabricate the high-quality grating structure, we tested different electron beam dose in electron beam lithography (EBL). It was noticed that the electron dose affects the shape and duty cycle of gratings significantly. SEM images of gratings fabricated at different electron dose are presented in **Figure 5.8**. We found the 165 and 190 uC/cm^2 are the best dose condition and we used these conditions in EBL fabrication.

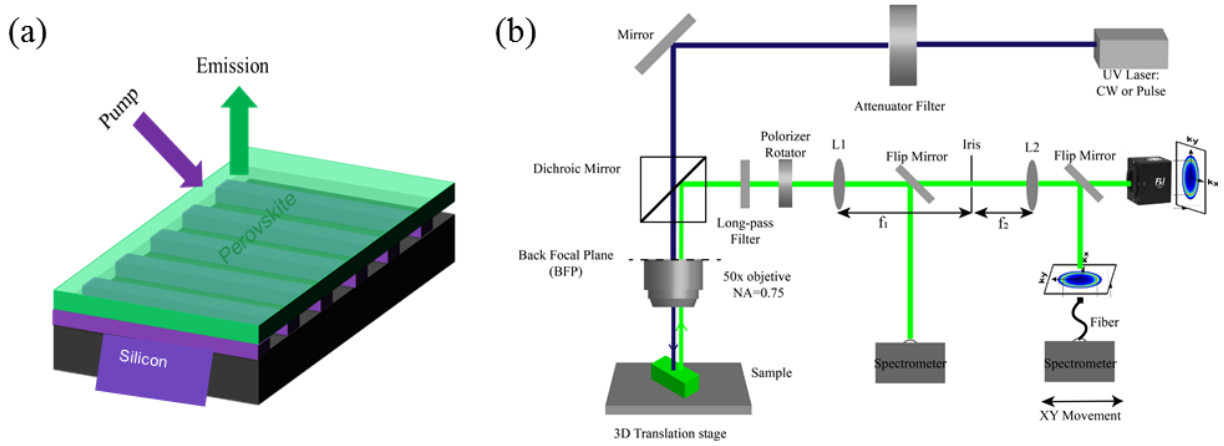

Figure 5.7. Schematic illustration of the perovskite DFB laser and measurement setup. (a) The schematic illustration of optically pumped distributed feedback laser. (b) The experimental setup for characterizing the perovskite laser.

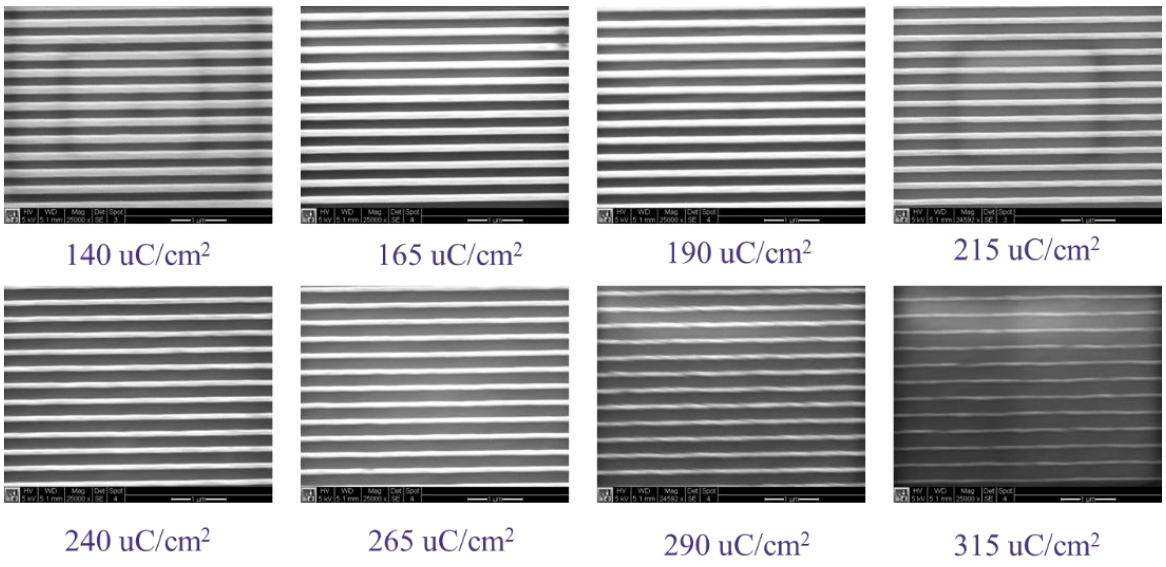

Figure 5.8. Planar SEM images of gratings fabricated by different electron dose.

We measured the emission spectra of our devices with grating structure using the experimental setup in **Figure 5.7(b)**. Below the lasing threshold, the device shows the normal PL spectrum with full width half maximum (FWHM) of 21 nm (**Figure 5.9a**). When the pump fluence increases and reach the threshold to achieve population inversion, a narrow peak emerges on the red side of the PL peak and the FWHM collapses to 1.2 nm. We believe the slightly wide linewidth is mainly caused by the unfavored duty cycle of the grating. A binary grating with a duty cycle of 50% provides minimal in plane feedback, which is not favorable in reducing lasing linewidth. A change in duty cycle from 50% to 25% or 75% can form DFB cavities with high finesse, so the demonstrated perovskite laser can potentially achieve a narrower linewidth and lower threshold. We also measured the amplified spontaneous emission (ASE) spectrum of perovskite thin films. The laser beam was focused to a rectangular stripe on the perovskite thin film and the edge emission was collected by the spectrometer. The ASE spectrum has a peak close to the lasing spectrum, but the FWHM is broadened to ~7.5 nm. **Figure 5.9(b)** shows the emission spectrum

from the device much above the lasing threshold, we can observe that the spontaneous emission peak at ~530 now show much smaller intensity than that of lasing peak located at ~ 552 nm.

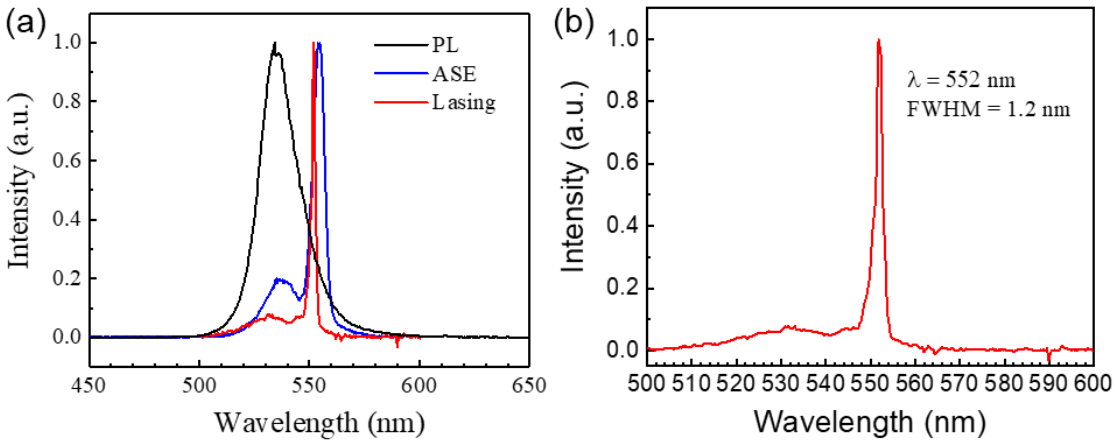

Figure 5.9. Performance characterization of perovskite DFB laser. (a) The PL, ASE and lasing spectrum of our perovskite DFB laser devices. (b) The lasing spectra under increasing pump fluence.

To obtain more insight into the angular dependence of the emission from the perovskite DFB grating, we performed k-space imaging with high numerical aperture (N.A. = 0.75) light collection. The results are shown in **Figure 5.10**. The k-space images of TE mode (electric field parallel to grating ridge) and TM mode (electric field perpendicular to grating ridge) emissions show clear difference, indicating the emission direction is polarization-dependent. It is clear that the grating direct luminescence into arcs of preferred angles in k-space images. Adjust the grating period or the perovskite film thickness can change the positions of these arcs. The k-space image of TE mode emission has most intensity in the center, which indicates the TE emission has much smaller angular divergence compared to TM mode. In addition, when the second order Bragg condition is satisfied, the emission angles are close to zero, which means the rings appear to touch in the center of k-space. Therefore, the current device would support TE instead of TM mode for lasing. Of course, this can be tuned by changing the grating period or perovskite thickness.

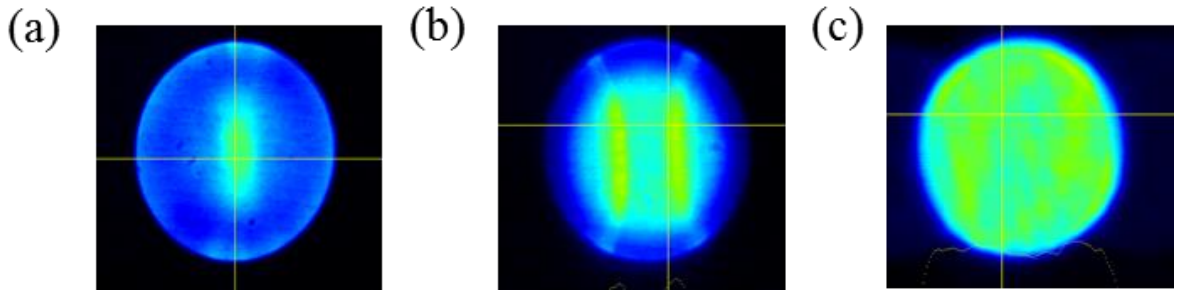

Figure 5.10. Experimental back-focal-plane images of emission from perovskite on grating. (a) Back-focal plane images of the emission component polarized parallel (TE) and (b) perpendicular (TM) to the grating ridge from the on-grating perovskite structure, respectively. (c) Back-focal plane image of the total emission from off-grating perovskite area.

5.3 CONCLUSION AND OUTLOOK

In summary, we demonstrate a perovskite VCSEL by integrating perovskite QDs with DBR mirrors. This approach combines the merit of QDs, namely high quantum efficiency, with a high-quality resonant cavity obtained through the DBR mirrors, and achieved an ultralow lasing threshold of 0.39 μJ/cm^2. The utilization of all-inorganic $CsPbBr_3$ QDs resulted in high device stability, and the laser maintained its performance over hours of operation under both fs and quasi-CW ns pulse pumping at ambient conditions. Besides perovskite VCSELs, we also demonstrate a second-order perovskite DFB laser on the silicon substrate. The *k*-space imaging results further confirm the polarized emission. These results indicate the strong potential of the proposed approaches for low-threshold, highly stable perovskite lasers towards CW operation in the future.

Chapter 6. TOWARDS ELECTRICALLY PUMPED PEROVSKITE LASER DIODES

Adapted with permission from:
Zou, C., Liu, Y., Ginger, D.S. and Lin, L.Y. Suppressing efficiency roll-off at high current densities for ultra-bright green perovskite light-emitting diodes. *ACS nano*, *14*(5), pp.6076-6086.

6.1 ABSTRACT

Perovskite light-emitting diodes (PeLEDs) have undergone rapid development in the last several years with external quantum efficiencies (EQE) reaching over 21%. However, most PeLEDs still suffer from severe efficiency roll-off (droop) at high injection current densities, thus limiting their achievable brightness and presenting a challenge to their use in laser diode applications. In this work, we show that the roll-off characteristics of PeLEDs are affected by a combination of charge injection imbalance, nonradiative Auger recombination, and Joule heating. To realize ultrabright and efficient PeLEDs, several strategies have been applied. First, we designed an energy ladder to balance the electron and hole transport. Second, we optimized perovskite materials to possess reduced Auger recombination rates and improved carrier mobility. Third, we replaced glass substrates with sapphire substrates to better dissipate joule heat. Finally, by applying a current-focusing architecture, we achieved PeLEDs with a record luminance of 7.6 Mcd/m^2. The devices can be operated at very high current densities (J) up to ~ 1 kA/cm^2. Our work suggests a broad application prospect of perovskite materials for high-brightness LEDs and ultimately a potential for solution-processed electrically pumped laser diodes.

6.2 INTRODUCTION

Solution-processed metal hybrid perovskites exhibit excellent luminescence, high color purity and tunable emission wavelengths, making them promising candidates for low-cost, high-performance light-emitting diodes (LEDs) and laser diodes (LDs).[10, 19, 31, 52, 53, 89, 95, 100, 163, 167, 208-212] Previously reported high-efficiency PeLEDs are mainly based on quasi-2D perovskites with multiple quantum wells (MQWs) in an effort to provide confinement for electron-hole pairs and thus increase the photoluminescence quantum yield (PLQY).[10, 53, 100, 163, 167, 209, 210] However, for most of these quasi-2D PeLEDs, the peak EQE is achieved at a very low current density (J < 0.1 mA/cm^2) and starts to drop significantly at high J.[99] This detrimental behavior is described as efficiency roll-off, which is likely caused by a combination of charge injection imbalance, Auger-induced luminescence quenching and Joule heating.[34, 99, 213-215] This efficiency roll-off, also known as droop, can be quantified by the critical current density (J_c) that corresponds to the J at which the EQE reduces to half of its peak value.[35] For most reported green PeLEDs, J_c remains in the regime of 1-100 mA/cm^2,[52, 100, 210] limiting their achievable brightness below 100,000 cd/m^2. A high luminance of ~500,000 cd/m^2 with a EQE of 9.3 % for PeLEDs have been achieved only very recently by Sim *et al.*, who replaced quasi-2D with 3D perovskites.[88] However, this value is still lower than the record for quantum dot LEDs, which is 1.68 × 10^6 cd/m^2 for green-emission.[215]

Suppressing efficiency roll-off at high J is also a necessary step towards electrically pumped perovskite laser diodes (PeLDs), which could in principle be enabled by perovskites' low amplified spontaneous emission (ASE) thresholds and long carrier diffusion lengths.[18] However, one vital problem needs to be overcome, namely, how to inject high J of over several hundreds of A/cm^2 without significant exciton quenching.[81, 216] These high current densities are needed because

the key parameter of $J \times EQE$ or luminance (L) need to be large enough to exceed the lasing threshold.[81]

Although eliminating efficiency roll-off is important both to the development of high-brightness LEDs and electrically pumped laser diodes for a variety of applications in lighting, projection display, and phototherapy, only a few studies on this topic have been reported for PeLEDs to date.[34, 35, 99, 217-219] Herein, we demonstrate, in quasi-2D PeLEDs, suppression of efficiency roll-off by balancing charge injection *via* building an 'energy ladder' in hole transport layers. Upon optimization, we achieved simultaneously high EQE (16.2%) and luminance (~31,000 cd/m^2). Next, to increase carrier mobility and reduce nonradiative Auger recombination, we replaced the insulating long-chain spacer (PEABr) in the quasi-2D perovskite with small cation KBr. The resulting luminance improves by about 4-fold to ~120,000 cd/m^2 and J_c increases by 20-fold to ~800 mA/cm^2. Subsequently, we investigated thermal-induced luminescence quenching by comparing glass and sapphire substrate based PeLEDs and show that Joule heat produced during device operation significantly affects the roll-off characteristics.[215] To further mitigate Joule heating, we fabricated current-focusing devices with small current injection areas and operated them under pulsed current injection. The generated Joule heating can be dissipated to the surrounding insulator area, thus improving heat sinking capability. Pulsed current operation helps devices survive at higher J by further reducing the average heating rate. Together, these strategies allow us to increase J_c up to ~60 A/cm^2 (54-fold improvement compared to the best previously reported values[35]) while operating the device at J values up to ~1 KA/cm^2 (highest reported among PeLEDs) without measurable damage to either the perovskite or injection layers, ultimately leading to a record luminance of 7.6 Mcd/m^2.

6.3 METHODS

Materials. $PbBr_2$ (99.9%, metal basis), CsBr (99.9, metal basis), KBr (99.9%, metal basis), PEABr (98%), PVK (MW 25000-50000) and dimethyl sulfoxide (DMSO, anhydrous) were purchased from Sigma Aldrich. Poly-TPD and TFB were purchased from American Dye Source. Chlorobenzene (anhydrous, 99.8%) and 1,4,7,10,13,16-hexaoxacyclooctadecane (18-crown-6, crown) (99%) were purchased from Acros. Poly(3,4-ethylenedioxythiophene) polystyrene sulfonate (PEDOT:PSS, AI 4083) and 2′,2′-(1,3,5-benzinetriyl)-tris(1-phenyl-1-H-benzimidazole) (TPBi, 98%) was purchased from Ossila. All chemicals were used as received without further purification.

Preparation of perovskite films. The quasi-2D precursor solution was obtained by mixing 0.2M CsBr, 0.2M $PbBr_2$ with different amount of PEABr and crown in DMSO at 60 °C for 2 h with constant stirring. The best molar ratio of PEABr to $CsPbBr_3$ is x = 40%. KBr-treated 3D precursor solution was obtained by mixing 0.024M KBr, 0.216M CsBr, 0.2 M $PbBr_2$ and crown in DMSO at 60 °C for 2 h with constant stirring. The perovskite precursor solutions were spin-coated onto substrates at 3000 rpm for 60s with an acceleration speed of 1500 rpm/s. Afterwards, the perovskite films were immediately annealed at 100 °C for 1 min to accelerate nucleation. Unless specified, the concentration of crown is 3.5 mg/ml in perovskite precursor solutions.

LED fabrication. All precursor solutions were filtered by 0.45 um Nylon or PTFE syringe filters before use. The pre-patterned ITO substrates (sheet resistivity 15 Ω/sq) were cleaned by critical cleaning detergent (Ossilla) in hot water with sonication for 5 min, then rinsed in DI water. The substrates were further cleaned in acetone, isopropyl alcohol, deionized water with sonication for 5 min in sequence. The cleaned substrates were dried by air gun and then placed in oven at 80 °C for 10 min. For Structure A, PEDOT:PSS was spin coated onto the substrate at 4000 rpm for 30s,

followed by annealing at 140 °C for 15 min. For Structure B, TFB solution (4 mg/ml in chlorobenzene) and PVK (4 mg/ml in chlorobenzene) were sequentially spin coated onto the PEDOT:PSS layer at 4000 rpm for 45s, followed by annealing at 150 °C for 20 min. For Structure C, the poly-TPD solution (10 mg/ml in chlorobenzene) was spin-coated onto the substrate at 4000 rpm for 45s, followed by annealing at 150 °C for 20 min. Then a PVK layer was formed by spin coating the PVK solution (4 mg/ml in chlorobenzene) at 4000 rpm and annealed at 150 °C for 20 min. The quasi-2D perovskite precursor was deposited onto different HTLs (Structure A, B and C) as mentioned above. The KBr-treated 3D perovskite precursor was deposited onto poly-TPD/PVK HTLs. The as-prepared substrates were then transferred to a thermal evaporator, the chamber was pumped down to a based vacuum pressure of 2×10^{-6} Torr. TPBi (40 nm), LiF (1 nm) and Al elctrode (70 nm) were sequentially evaporated at a deposition rate of 1, 0.3, 2 Å/s respectively. These devices were then encapsulated by UV epoxy (Ossila) and thin glass slides in a nitrogen-filled glove box. All device tests were conducted in ambient condition (21 °C, 40~50% humidity).

Current-focusing device fabrication. For micro-size current-focusing devices, a 150 nm SiO_2 layer was first deposited onto the ITO-coated substrates by plasma enhanced chemical vapor deposition (PECVD) at 125 °C. The positive photoresist (AZ1512) was spin-coated onto substrates at 2000 rpm for 45s and prebaked at 110 °C for 4 min. The photoresist was exposed for 3.5s (Semiauto aligner, ABM) and then developed in AZ340 for 1 min. The micro-holes with different diameters were transferred to the SiO_2 layer by plasma etching (ICP-Fluorine). The photoresist was then stripped by N-Methyl-2-Pyrrolidone (NMP) at 90 °C overnight.

For nanopatterned current-focusing devices, electron beam lithography was used to generate holes with diameter of 100 nm. ZEP 520 resist (diluted in 1:1) was spin-coated onto the ITO-

coated substrates at 2000 rpm for 60 s and baked at 180 °C for 5 min. The resist was exposed by electron beam at a dose of 160 uC/cm^2 and then developed in amyl acetate for 2 min. The nanopatterned holes were transferred to the SiO_2 layer by plasma etching (ICP-Fluorine). The ZEP resist was finally stripped by NMP at 90 °C overnight. The PeLEDs were then fabricated on substrates with current apertures with the same procedure as mentioned in the LED fabrication section.

Perovskite film characterization. The surface morphologies of perovskite films were analyzed by SEM (FEI, Siron) and AFM (Icon, Bruker). XRD patterns were recorded using Bruker D8 with a Cu Kα radiation (λ = 1.54184 Å). The PLQYs were measured using a CW laser (λ = 405 nm), an integration sphere and a spectrometer as reported elsewhere.[220] The quasi-2D and KBr-treated 3D perovskite films were deposited on clean glass substrates. The samples were clamped by a holder in integration sphere, the laser beam was focused onto samples with a convex lens. The focused beam size was determined by a CCD beam profiler (Thorlabs) and the power was measured by a silicon photodiode (Newport 818-UV). The PLQY was determined as the number of emitted photons to the number of absorbed photons.

For transient PL characterization, the samples were pumped by an ultrafast femtosecond Ti-Sapphire laser with OPA (λ=365 nm, 50 fs). The pump power was adjusted by a variable attenuator wheel and detected by a handheld detector (Coherent FieldMaster). The excitation laser beam profile was measured by a CCD beam profiler (Thorlabs, BC106N-VIS), and the beam diameter was determined by the 1/e^2 cut-off of the Gaussian fit to the beam profile. The emitted PL from samples was collected by a pair of convex lenses and recorded by a streak camera with ~10 ps time resolution. The IRF of the tr-PL set-up was measured using a glass in the same optical geometry as the sample measurements.

Performance evaluation of perovskite LEDs. The current density-voltage (J-V) characteristics were measured by a computer-controlled source meter (Keithley 6430). The voltage was swept from 1 to 9 V with a step voltage of 0.2 V. Simultaneously, front-face EL power output from ITO side was measured by a calibrated silicon photodiode (Newport 818-SL) with a computer controlled optical meter (Newport 1830-C). The photodiode's active area (1 cm^2) was well aligned with the emissive pixel. Lambertian emission profile was assumed in calculating the total radiance. The EQE was calculated by dividing the number of emitted photons by the number of injected electrons. The EL spectra of PeLEDs were recorded by a fiber coupled spectrometer (Newport OSM 100). All device measurements were performed in a dark box under ambient condition.

For pulsed current measurement, a current source (Newport LDP 3811) was used to provide current pulses (2 μs pulse width, 0.2% duty cycle, 1 KHz repetition rate). The emitted EL power was measured by a fast-response silicon photodiode (FDS1010, Thorlabs). The photodiode was connected to a custom-built large bandwidth transimpedance amplifier. The amplified signal was then sent to an oscilloscope for calculating average EL power based on the responsivity of the photodiode.

Measurement of operational lifetime. The PeLEDs were driven by a constant current through Keithley 6430. The initial luminance is set as ~100 cd/m^2 by adjusting the drive current. The EL power was monitored by a silicon photodiode (Newport 818-SL) and the applied voltage was recorded by Keithley 6430. The data was taken with an interval of 10 seconds.

6.4 RESULTS AND DISCUSSION

6.4.1 *Reducing the efficiency roll-off by balancing charge injection.*

For many non-inverted PeLEDs, there is no energy barrier for electron injection between common electron transport layers (ETLs) like 2′,2′-(1,3,5-benzinetriyl)-tris(1-phenyl-1-H-benzimidazole) (TPBi) and perovskite layers. However, hole injection is not efficient due to the energy barrier between common hole transport layers (HTLs) and perovskite layers.[49, 221] As a result, electron and hole charge injection are often not balanced, resulting in deterioration of PeLED performance. In addition, the electron-hole pairs tend to be quenched near the interface between the HTL and perovskite layer due to the unmatched energy levels, which causes nonnegligible luminescence quenching, especially for green- and blue-emitting PeLEDs.[86, 222]

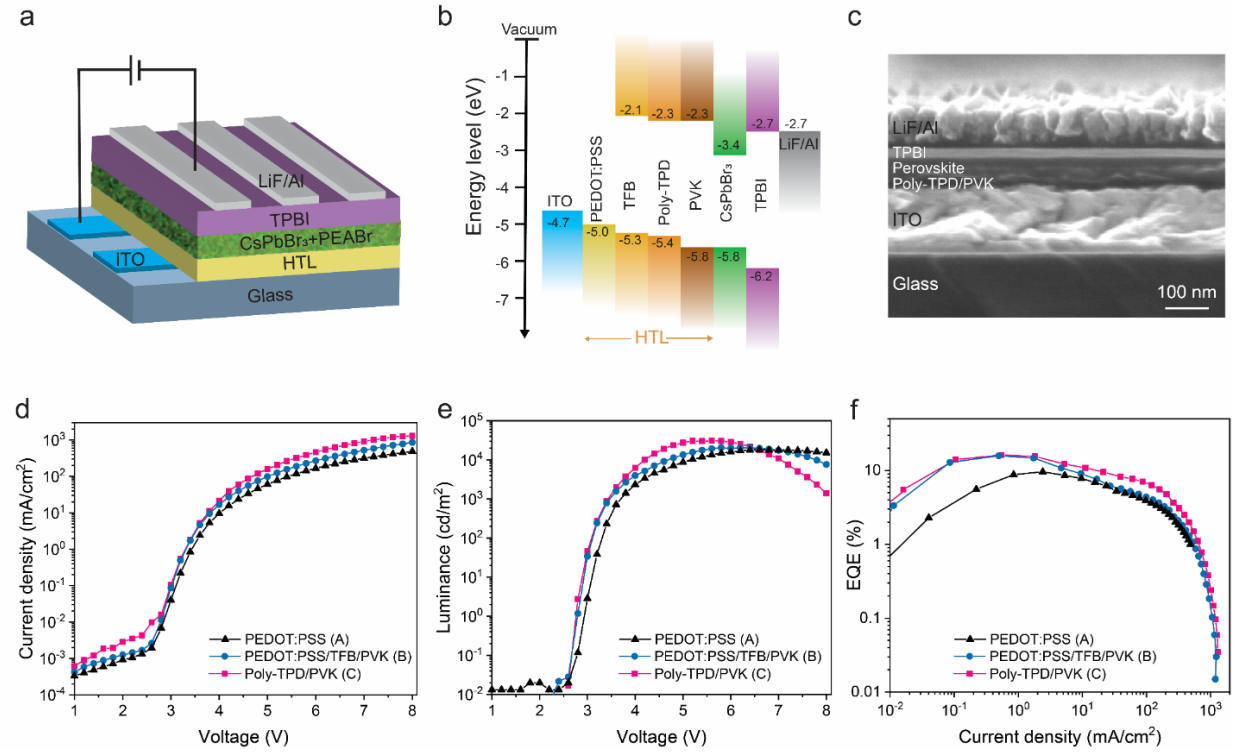

Figure 6.1. Performance comparison of quasi-2D PeLEDs based on different HTLs. (a) Schematic Structure Architecture. (b) Energy level diagram of quasi-2D PeLEDs

with various HTLs. (c) High-resolution SEM cross-sectional image. (d) *J-V*, (e) *L-V* and (f) *EQE-J* data of Structure A, B and C.

We used the quasi-2D perovskite $(PEABr)_xCsPbBr_3$ (where x is the molar ratio of PEABr to $CsPbBr_3$) in our work first due to the enhanced PLQY originated from MQW confinement.[223] We fabricated quasi-2D PeLEDs with the device structure of ITO/HTL/Perovskite/TPBi/LiF/Al as schematically illustrated in **Figure 6.1(a**). Different HTLs were adopted to improve hole injection, the common HTL of PEDOT:PSS was used for comparison (Structure A). By inserting additional HTLs of TFB and PVK between the PEDOT:PSS and perovskite, a stepwise 'energy ladder' is realized (Structure B). In addition, the bilayer HTL of poly-TPD/PVK was also used as an energy ladder (Structure C). **Figure 6.1(b)** shows the energy band diagram of these PeLEDs including various HTLs, the highest occupied molecular orbital (HOMO) energy level of $CsPbBr_3$ is -5.8 eV, while it is only ~ -5.0 eV for PEDOT:PSS. Thus, a large energy barrier exists for hole injection from the PEDOT:PSS and perovskite layer, leading to inefficient hole injection and luminescence quenching at the interface. In contrast, the HOMO energy level of PVK is -5.8 eV, which is well-matched to the valence band edge of $CsPbBr_3$. The HOMO energy levels of TFB and poly-TPD are -5.3 and -5.4 eV respectively, right between those of PEDOT:PSS and PVK. **Figure 6.1(c)** shows the cross-section view of Structure C obtained *via* scanning electron microscopy (SEM). Multiple layers are clearly visible in the following order (from bottom to top): ITO (~150 nm), poly-TPD/PVK(~35 nm), perovskite (~40 nm), TPBi (~40 nm), and LiF/Al (~70 nm).

We measured the current density–voltage (*J-V*) characteristics of all device structures (**Figure 6.1d**) and found Structure C showed the highest *J* whereas Structure A showed the smallest *J*. To further quantify charge injection, we measured the *J-V* characteristics of hole-only devices (based on different HTLs) and electron-only devices (**Figure 6.2**). The hole-only devices based on poly-

TPD/PVK show the highest *J* compared to those of other devices based on PEDOT:PSS and PEDOT:PSS/TFB/PVK. These results confirm the poly-TPD/PVK HTL best enhances the hole injection efficiency and improves the number of injected holes.

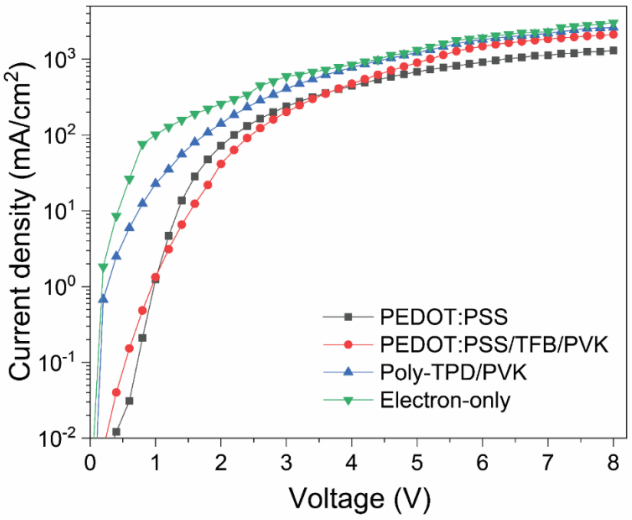

Figure 6.2. Current density-voltage (*J*-*V*) curves of unipolar charge transport devices. The structures are ITO/ZnO/quasi-2D perovskite/TPBi/LiF/Al for electron-only devices and ITO/HTL/quasi-2D perovskite/MoO_3/Au for hole-only devices. Among hole-only devices, the devices based on poly-TPD/PVK show the highest current densities, confirming the better hole injection efficiency.

Furthermore, we found that electrons dominate charge injection into quasi-2D perovskite devices, and a more balanced charge injection occurs in the case of poly-TPD/PVK devices. The perovskite films formed on different HTLs all exhibit smooth and continuous surface morphologies without obvious pinholes (**Figure A.6, A.7**). The leakage *J* for Structure A, B and C is at a low level below 10^{-3} mA/cm^2, confirming good coverage of perovskite films on different HTLs used here.

We further compare the luminance–voltage (*L*–*V*) characteristics (**Figure 6.1e**), the turn on voltage (defined as the voltage at which the luminance is 1 cd/m^2) of multilayer HTL devices (Structure B and C, ~ 2.8 V) is also lower than that for the single layer HTL device (Structure A,

~3 V), consistent with the reduced energy barrier and enhanced hole injection through the energy ladder. Table 6.1 summarizes the performance parameters of Structure A, B and C. Structure A shows a maximum luminance of 18,154 cd/m^2, which is further increased to 20,342 and 31,012 cd/m^2 for Structure B and C, respectively. The 1.7-fold brightness improvement from Structure A to Structure C has been achieved through improving the hole injection efficiency and balancing charge injection.

Table 6.1. Performance comparison of quasi-2D PeLEDs with different HTLs

HTL	***EQE*** **(%)**	***Luminance*** **(cd/m^2)**	J_c **(mA/cm^2)**
PEDOT: PSS	9.6	18 154	46
PEDOT: PSS/TFB/PVK	15.8	20 342	10
Poly-TPD/PVK	16.2	31 012	40

The maximum EQEs for Structure A, B and C are 9.6%, 15.8% and 16.2%, respectively (**Figure 6.1f**). Structure C exhibits the best efficiency roll-off suppression performance with an EQE higher than Structure A and B in a wide range of *J* from 0.01 to 1000 mA/cm^2. We also observe that the devices with multilayer HTLs (Structure B and C) show higher EQEs compared to single-layer HTL device (Structure A). We propose this result is due to either of two causes: (1) suppressed luminescence quenching at the interface between the HTL and the perovskite layer, or (2) more balanced charge injection originated from improved hole injection efficiency.[86, 224] We note that Structure C shows a similar EQE to Structure B at low *J* (0.01 ~ 10 mA/cm^2). However, the EQE of Structure B drops faster after ~10 mA/cm^2, which indicates the imbalanced charge injection at high *J* for Structure B. This finding is consistent with **Figure 6.1(d)**, where Structure

B and C have almost the same *J* at low voltage (2.8 - 3.8 V) and start to show larger discrepancy at high voltage (after 3.8 V, 10 mA/cm^2).

Although the efficiency roll-off of quasi-2D PeLEDs can be suppressed by reducing charge injection barriers, typical quasi-2D PeLEDs still suffer from severe efficiency roll-off at high *J*, likely due to the poor charge transport with the insulating long-chain PEABr layer and increased non-radiative Auger recombination rate originated from the enhanced local charge carrier density in the MQW structures.[34, 225] A 405 nm laser was used as excitation source, the optical chopper is connected to a lock-in amplifier and operated at 400 Hz (**Figure 6.3a**). PeLEDs were operated at different voltages. The PL could enter the photodetector through a long pass (LP) filter. The signal was sent to the lock-in amplifier and PL intensity of devices at different biases could be obtained. The electroluminescence (EL) intensity was obtained directly by photodetector without operating the laser source and optical chopper. For positive voltage region, more carriers are injected with increasing voltage, when the voltage exceeds the maximum EQE point, the PLQE starts to drop, which is due to the increasing Auger recombination with a large number of injected carriers.[34] For negative voltage region, the electric field separates electrons and holes, so the possibility for them to recombine decreases, which accounts for the drop of PLQE under negative voltage.

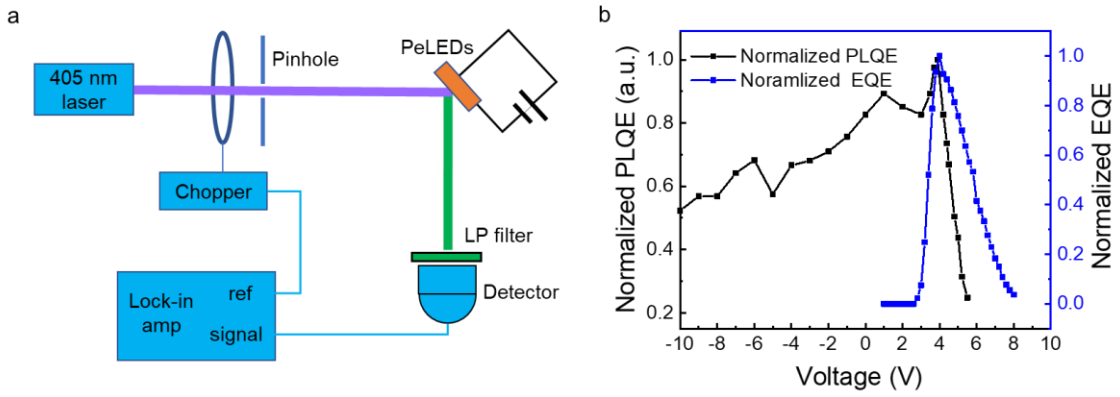

Figure 6.3. Investigation on the photoluminescence quantum efficiency (PLQE) of PeLEDs under electric biases. (a) Layout of the measurement system. (b) The normalized PLQE and EQE of PeLEDs at different biases.

The quasi-2D PeLEDs (x = 0.4) achieve much higher peak EQE than the 3D counterparts (x = 0), however, they show similar or even worse performance at high *J* (**Figure A.8**). These characteristics hinder quasi-2D PeLEDs from maintaining high efficiency at high J and achieving ultrahigh brightness, motivating us to further contrast the performance of quasi-2D and 3D perovskites.

6.4.2 *Higher brightness and enhanced stability from KBr-treated 3D perovskite LEDs.*

For the practical applications of LEDs, and the development of electrically pumped laser diodes, a key parameter of devices is the $J \times EQE$ (or brightness). 3D perovskites generally can withstand higher *J*; however, their PLQY is usually lower due to small exciton binding energy.[32, 226, 227] Although high PLQYs are achievable with proper surface passivation of 3D perovskites.[8, 9, 220]

Recently, Jalebi *et al*. reported the enhanced luminescence from 3D perovskites following potassium passivation.[8] Following this method, we introduced excess KBr during $CsPbBr_3$ synthesis to form KBr-treated 3D perovskites. Enhanced photoluminescence (PL) was also

observed for these KBr-treated 3D perovskite films (**Figure A.9**). The device structure of the KBr treated PeLEDs studied here is the same as Structure C of quasi-2D PeLEDs described above.

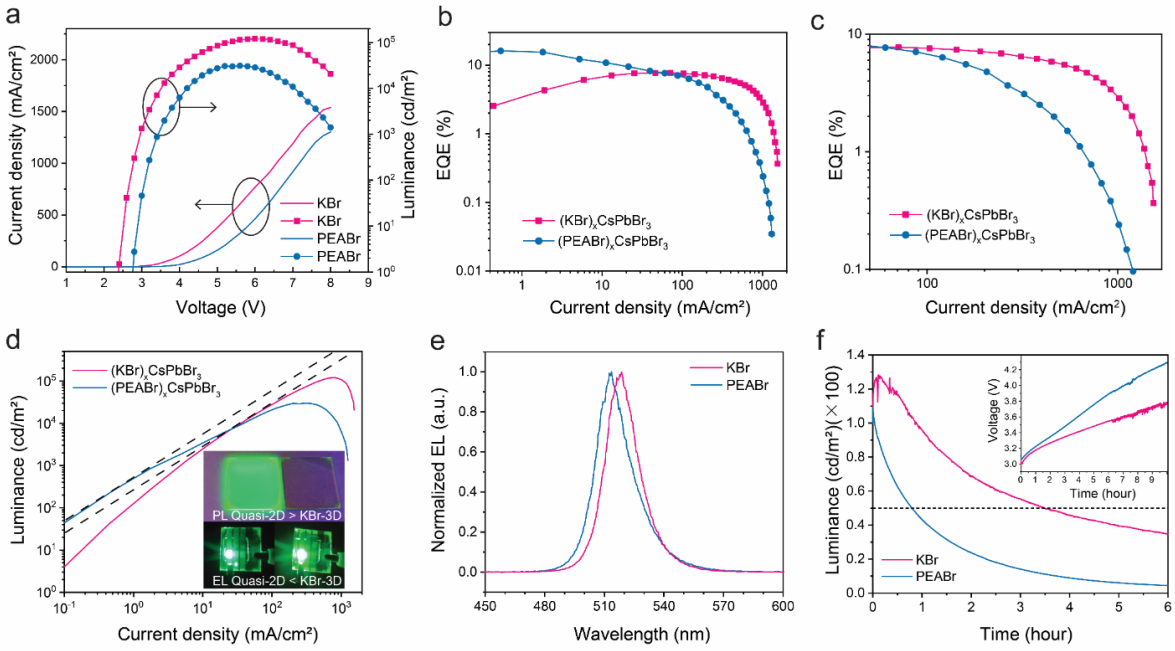

Figure 6.4. Performance comparison of PEABr- and KBr-based PeLEDs. (a) *L-J-V* data. (b) *EQE versus J*. (c) Efficiency roll-off comparison in high *J* region (50 to 1500 mA/cm^2). (d) *L-J* characteristics, the dashed lines indicate *L-J* curves without efficiency roll-off. The inset shows the real photos of PL and EL from PEABr- and KBr-based perovskite films. (e) EL spectra of PEABr- and KBr-based devices. (f) Luminance degradation with time, the initial luminance is 100 cd/m^2 for both devices. The inset shows the evolution of applied voltage during operation.

The KBr-based PeLEDs show higher *J* compared to PEABr-based counterparts (**Figure 6.4a**), which indicates the higher conductivity of KBr-based perovskite films as the additive KBr distrupts the 3D perovskite conduction much less than the incorporation of the large insulating cation of PEABr (and the formation of quasi-2D layers). The KBr-based PeLEDs also show a lower turn-on voltage of 2.4 V, which is the same as the bandgap of $CsPbBr_3$, consistent with barrier-free injection of charge carriers. In addition, compared to the PEABr-based devices, the

KBr-based PeLEDs exhibit suppressed luminance droop and approximately 4-fold luminance enhancement.

The KBr-based PeLEDs show smaller EQEs in the low *J* region but then they exceed that of quasi-2D PeLEDs when $J > \sim 50$ mA/cm^2 (**Figure 6.4b**). Although the peak EQE of the KBr-based PeLEDs (7.7%) is lower than that of the quasi-2D counterparts (16.2%), we highlight that the KBr-based PeLEDs exhibit suppressed efficiency roll-off, allowing better performance at high drive current densities (**Figure 6.4c**). The EQE for the KBr-based LEDs at a high *J* of 1000 mA/cm^2 remains at ~3%, which is a 10-fold enhancement compared to the PEABr-based PeLEDs at such a high *J*. In **Figure 6.4(d)**, the black dashed lines represent simulated *L*-*J* curves that might be expected without efficiency roll-off. The *L*-*J* curve of the KBr-based PeLEDs overlaps more with the ideal curve. The maximum luminance for KBr- and PEABr-based PeLEDs is 120,187 and 31,012 cd/m^2 with the corresponding J_c of ~800 and 40 mA/cm^2, respectively. The detailed performance comparison is included in **Table 6.2**. It should be noted the PL intensity of the KBr-based 3D perovskites is much smaller than that of PEABr-based quasi-2D perovskites under the excitation from UV lamp (inset photograph of **Figure 6.4d**); however, the electroluminescence (EL) is 4-fold enhanced, suggesting even higher performance could possibly be achieved with higher-quality 3D perovskite samples. We will discuss these phenomena in more detail later.

Table 6.2. Performance comparison of quasi-2D and KBr-treated 3D PeLEDs

Film	***EQE*** **(%)**	***Luminance*** **(cd/m^2)**	J_c **(mA/cm^2)**
Quasi-2D	16.2	31 012	40
KBr-treated 3D	7.7	120 288	800

The EL spectrum of KBr-treated 3D PeLEDs shows a narrow FWHM of 19 nm with the peak wavelength located at 519 nm (**Figure 6.4e**), which is slightly red-shifted in contrast to that of quasi-2D PeLEDs (513 nm, FWHM 20 nm). The higher bandgap of quasi-2D perovskite is due to the formation of MQWs. Operational stability is an important parameter for evaluating PeLEDs,[228-230] we measured the evolution of luminance with time for both devices (**Figure 6.4f**). The initial luminance was kept at 100 cd/m^2, and the *J* was kept constant. It is clearly observed that the KBr-based PeLEDs show much slower luminance decay compared to PEABr-based PeLEDs. We introduce a key parameter T_{50} to quantitatively compare the operation stability of both devices, which is defined as the time it takes for the luminance to decrease to half of its initial value. The T_{50} values for PEABr- and KBr-based PeLEDs are 0.8 and 3 hours, respectively, showing better operation stability of KBr-based PeLEDs. The inset figure shows the applied voltage of both devices increases steadily with time to maintain a constant *J*. However, KBr-based PeLEDs show a slower voltage increase, which may be of help to suppress the ion migration across devices due to the reduced electric field.

6.4.3 *Carrier recombination dynamics of PEABr and KBr-based perovskite thin films.*

The charge carrier dynamics can be described with the following equation[231, 232]

$$\frac{dn(t)}{dt} = G - k_1 n - k_2 n^2 - k_3 n^3 \qquad (6.1)$$

Where *n* is the charge carrier density, *t* is the time, *G* is the generation rate, k_1 is the monomolecular recombination rate, k_2 is the bimolecular recombination rate and k_3 is the Auger recombination rate. In general, the monomolecular recombination can be divided into trap-assisted recombination, excitonic recombination, and pseudo-first order recombination of minority carriers at low injection levels. The former is nonradiative while the latter two can be radiative.[226] Bimolecular recombination is a radiative process which emits photons, while Auger recombination

is a nonradiative process which involves three or more charge carriers and converts energy to phonons.[231]

To analyze the different performance of PEABr- and KBr-based PeLEDs, we recorded the transient PL decays of both perovskite thin films under femtosecond pulsed excitation (λ = 365 nm). **Figure 6.5(a)** summarizes the PL_0 (the initial PL intensity, emitted in coincidence with the excitation laser pulse) as a function of carrier density for both samples. For the KBr-based perovskites, the quadratic power dependence of the PL_0 on the carrier density is consistent with radiative bimolecular recombination in competition with monomolecular nonradiative recombination. In contrast, for the PEABr-based perovskites, PL_0 increases linearly with the carrier density, indicating that PL originates from monomolecular recombination of bound excitons. This result is consistent with the formation of MQWs which provides confinement for the photo-excited geminate electron-hole pairs and thus increases the exciton binding energy.[32]

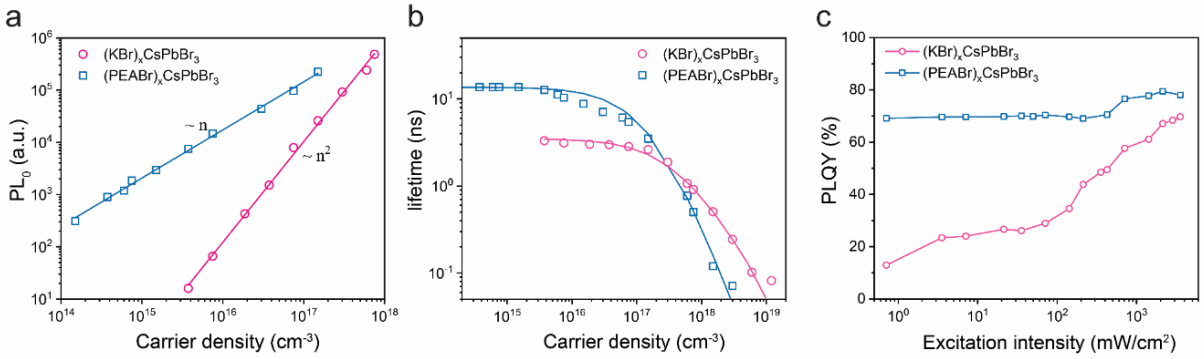

Figure 6.5. Investigation on carrier recombination dynamics of PEABr- and KBr-based perovskite films. (a) The dependence of PL_0 and (b) lifetime ($\tau_{1/e}$) on carrier density (n). (c) Internal PLQY as a function of incident excitation intensity.

The dependence of effective lifetime ($\tau_{1/e}$) as a function of carrier density for PEABr- and KBr-based perovskites is shown in **Figure 6.5(b)**. Such dependence can be well-fitted by equation (1), following the method proposed by Xing *et al.*[32] The fitted recombination coefficients are

presented in **Table 6.3**, which are consistent with previous reports.[163, 226, 231] Although the monomolecular recombination is mainly non-radiative in KBr-based perovskites, the k_2 value of KBr-based perovskites is slightly higher than that of PEABr-based perovskites, ensuring that the KBr-based perovskites can achieve comparably high PLQY as PEABr-based perovskites. In addition, it should be noted that k_3 for KBr-based perovskites is one order smaller than that of PEABr-based perovskites, indicating suppressed Auger recombination in KBr-based perovskites.[163]

Table 6.3. Fitted recombination coefficients from transient PL decay measurement for perovskite films of different compositions.

Film	k_1 (s^{-1})	k_2 (cm^3s^{-1})	k_3 (cm^6s^{-1})
$(PEABr)_x(CsPbBr_3)$	7.3×10^7 (excitonic)	$(1.7 \pm 0.3) \times 10^{-9}$	$(6.5 \pm 0.8) \times 10^{-27}$
$(KBr)_x(CsPbBr_3)$	2.9×10^8 (trap assisted & radiative pseudo-1st order recombination)	$(2.0 \pm 0.1) \times 10^{-9}$	$(2.9 \pm 0.4) \times 10^{-28}$

Figure 6.5(c) presents the internal PLQY of our PEABr- and KBr-based perovskite films measured under different continuous wave (CW) laser excitation intensity. The internal PLQY was calculated based on the light escape probability and measured external PLQY by a model accounting for photon recycling and light outcoupling effect (see details in Supplementary note 1, Supporting Information).[8, 227] The PEABr-based perovskite films show a nearly invariant internal PLQY as high as 70% at excitation intensities below 500 mW/cm^2, which is attributed to the first-order excitonic emission under low excitation density conditions. Under LED working conditions, where the carrier density is typically $<10^{15}$ cm^{-3} (corresponding to ~600 mW/cm^2), the nearly invariant high PLQY at low carrier density for PEABr-based perovskite films ensures the high

EQE of quasi-2D PeLEDs at low injected *J*. Above 500 mW/cm^2, The PLQY slightly increases as the radiative bimolecular recombination becomes effective. Unfortunately, we couldn't further increase the excitation intensity due to the limitation of maximum power provide by our CW laser. Therefore, the expected behavior that PLQY declines at higher excitation intensity was not observed. For KBr-based perovskite films, the PLQY starts at a relatively low value under low excitation intensity, which is consistent with high levels of non-radiative recombination in KBr-based perovskites. However, the PLQY increases significantly when the excitation intensity is above 100 mW/cm^2 as the radiative recombination from free electron-hole pairs starts to dominate. This observation clearly reveals that the EQE limitation for KBr-based PeLEDs at relatively low current density is from the non-radiative recombination losses, likely due to defect-mediated recombination. However, at the high excitation intensity region, the PLQY of KBr-based perovskite films is close to that of PEABr-based perovskite films. Therefore, defect passivation is likely desired to further improve the peak EQE of KBr-based 3D PeLEDs. Under steady-state excitation, the PLQY (η(n)) for 3D perovskites is given by[226]

$$\eta(n) = \frac{k_r + k_2 n}{k_1 + k_2 n + k_3 n^2} \tag{6.2}$$

Where k_r is the radiative "pseudo-monomolecular" decay coefficient due to the recombination of minority photoexcited carriers with intrinsic majority carriers at low fluence. The PLQY should be strongly dependent on *n*. It first increases with increasing *n* as the radiative biomolecular recombination gradually dominates over the nonradiative trap-assisted monomolecular recombination. At high carrier density, where the three-body Auger recombination becomes effective and dominates over the bimolecular recombination, the PLQY will in turn decrease with increasing *n*. In order to study the effect of individual rate constant on PLQY, we calculated carrier density dependent PLQY with two recombination coefficients fixed and one varied at some typical

values (**Figure A.10**). We found that a high-quality 3D perovskite film requires small k_1, k_3 and large k_2. Furthermore, for the purpose of suppressing the PLQY droop at high carrier density and enhancing the luminance of PeLEDs, only small k_3 and large k_2 are particularly required as k_1 almost only affects the PLQY at low carrier density. Since KBr-treated 3D perovskites show lower Auger recombination, we conclude that 3D perovskites are better suited for suppressing efficiency roll-off, the PeLEDs in the next parts of this work are all based on KBr-treated 3D perovskites.

6.4.4 *Thermal management for reducing Joule heat*

Another critical factor that contributes to the efficiency roll-off is Joule heating. At high *J*, due to the presence of leakage current and nonradiative Auger recombination, a large amount of energy is released in the form of heat, leading to the increase of device temperature.[215] The generation of joule heat could cause crystal distortions, surface traps and ion migration, thus deteriorating the PLQY and other optoelectronic properties of perovskite films. In addition, perovskite materials usually have poor thermal stability, devices could break down or even burn out at elevated temperatures.

To assess local heating, we measured the substrate temperature distributions of glass- and sapphire-based PeLEDs at various drive voltages using an infrared camera (**Figure 6.6a**). The temperature images were all captured after applying a specific voltage for 30 s. The glass substrate temperature rises rapidly with increasing voltage, reaching up to 113 ºC at 9 V. It should be noted that the temperature of the LED junction could be even higher than the observed surface temperature due to the low thermal conductivity of functional layers in PeLEDs. At such a high temperature, the perovskite active layer, as well as the injection layers, could be damaged or destroyed. We proposed that, by using transparent sapphire substrates as heat sinks, the Joule heating could be more effectively dissipated as sapphire has much higher thermal conductivity (46

$Wm^{-1}K^{-1}$) compared to glass (1.1 $Wm^{-1}K^{-1}$). **Figure 6.6(a)** confirms this hypothesis, with the substrate temperature of sapphire-based PeLEDs increasing only moderately from 22 ºC at 4 V to only 44 ºC at 9 V. We also note that the temperature distribution of the sapphire substrate is more uniform compared to the glass substrate, meaning that Joule heat can efficiently diffuse into the surroundings through the whole sapphire substrate as a result of the higher thermal conductivity.

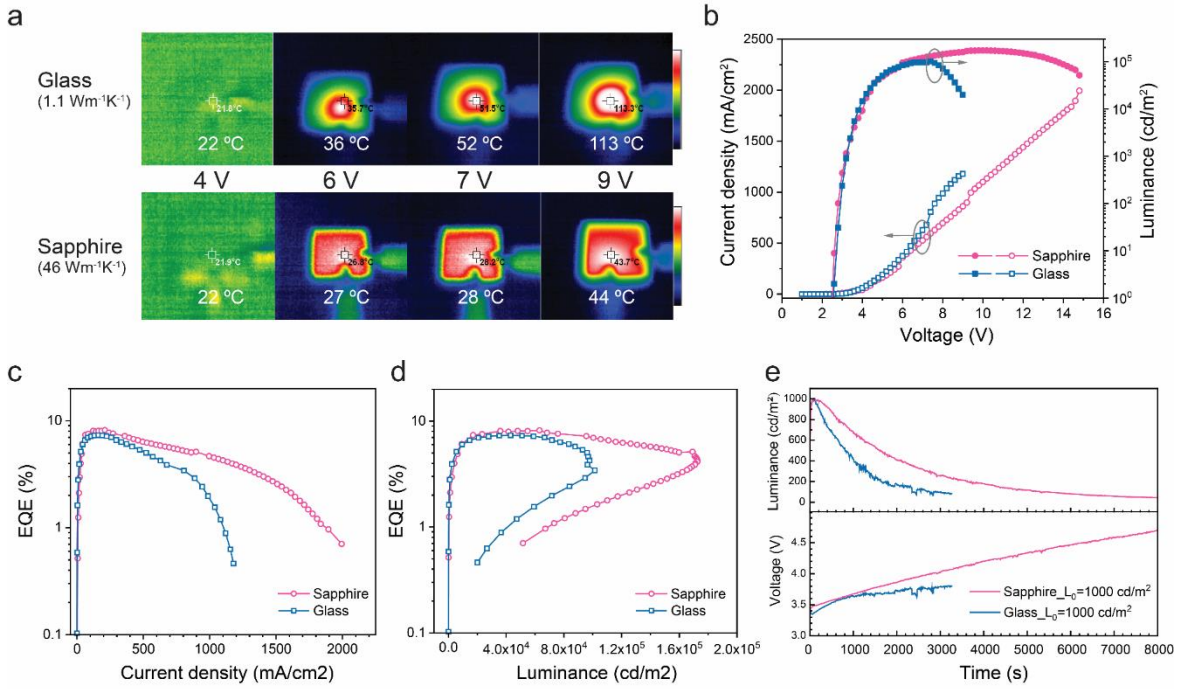

Figure 6.6. Replacing glass with sapphire substrates to reduce thermal-induced efficiency roll-off. (a) Surface temperature distributions of KBr-based PeLEDs based on glass and sapphire substrates at various voltages. (b) *L-J-V*, (c) *EQE-J* and (d) *EQE-L* characteristics of glass- and sapphire-based devices. (e) Evolution of luminance and voltage for both devices, the initial luminance is 1000 cd/m^2.

As the emission properties of perovskite materials are significantly affected by temperature,[233] the better thermal dissipation of sapphire substrates should both help PeLEDs survive at a higher *J* and suppress thermal-induced efficiency roll-off. To confirm this hypothesis, we compare the *L-*

J-V characteristics of PeLEDs on glass and sapphire substrates (**Figure 6.6b**). Both devices exhibit similar *J-V* characteristics at low voltage (<7 V). Nevertheless, the glass-based devices show a larger *J* than that of sapphire-based devices at higher voltage. This is because Joule heating can accelerate the hopping of charge carriers in perovskite materials, thus speeding up charge carrier injection and transport. For *L-V* characteristics, both devices exhibit a similar luminance rise with increasing voltage at the beginning (<7 V). However, the luminance of glass-based devices shows faster decline after 7 V. In contrast, sapphire-based devices are able to maintain a high luminance value with minor drop-off up to 15 V. Almost no EL can be detected from glass-based substrates at such a high voltage due to damage to perovskite layers.

Figure 6.6(c) shows *EQE-J* characteristics for PeLEDs on glass and sapphire substrates. It is clearly observed that efficiency roll-off is significantly suppressed for PeLEDs on sapphire substrates. The EQE for sapphire-based devices still maintains a high value of 2.6% at a high *J* of 1.5 A/cm^2. It should be also noted that sapphire-based devices achieve a higher peak EQE (8.2%) compared to glass-based ones (7.3%), which is attributed to higher light outcoupling efficiency of the former (see optical simulations in **Figure A.1**).[234] A more distinct comparison of efficiency roll-off can be acquired from the *EQE-L* characteristics (**Figure 6.6d**). The EQE of sapphire-based devices exhibits milder decline with increasing luminance in contrast to glass-based ones. Both devices show a cliff-like efficiency droop where the luminance achieves the maximum value and starts to decrease, which indicates both devices go through the destruction of the functional layers after applying a sufficiently large voltage or current density. However, the maximum luminance of sapphire-based devices is ~1.7-fold higher than that of glass-based devices, demonstrating better heat dissipation by using sapphire substrates.

We also compare the operation stability of PeLEDs on glass and sapphire substrates with a high initial luminance of 1000 cd/m^2 (**Figure 6.6e**). The sapphire-based devices show slower luminance decay. The T_{50} lifetime is 13 and 20 minutes for glass- and sapphire-based devices, respectively. The applied voltage of both devices goes up with time to maintain the constant J. For sapphire-based devices, the applied voltage increases from 3.7 V to 4.6 V after about 2-hour operation. However, the applied voltage of glass-based devices seems to become steady after ~20 minutes, indicating possible device failures.

6.4.5 *Applying the current-focusing architecture and pulsed current operation*

In addition to using sapphire substrates for thermal management, we also apply a small-area current aperture strategy to help mitigate Joule heating. This strategy is effective because the generated Joule heat can diffuse from the current flow regions to the surrounding insulating layer which act as heat sinks, thus improving the performance of PeLEDs at high J.[235, 236] Devices were also driven by pulsed current to further minimize the impact of Joule heating and ion migration.[218, 237] The suppressed efficiency roll-off was first successfully demonstrated by managing joule heating using a micro-size current aperture structure (Φ = 200 μm) (**Figure A.11**). These devices show the highest $J \times EQE$ (0.41 A/cm^2) and luminance (1.5 Mcd/m^2) under pulsed current operation (pulse width 2 μs, duty cycle 0.2%), a 22-fold enhancement from reference devices (**Table 6.4**). Besides, J_c is improved to 7 A/cm^2, much higher than that of reference devices (0.8 A/cm^2). It is interesting to note that the EL response time for KBr-based devices is much shorter than that of PEABr-based devices under pulsed current operation (pulse width 2 μs), consistent the improved carrier mobility for KBr-treated 3D perovskite films (**Figure A.12**).

Table 6.4. Performance comparison of current-focusing and reference devices (KBr-treated 3D perovskites)

Structure and operation mode	*EQE* (%)	$J \times EQE$ (A/cm^2)	*Luminance* (cd/m^2)	J_c (A/cm^2)
Reference (DC)	7.7	0.019	70,939	0.5
200 μm hole (DC)	8.0	0.063	232,805	1.5
200 μm hole (pulse)	9.3	0.41	1,491,583	7
100 nm Nanodot (DC)	7.2	0.39	1,417,312	9.5
100 nm Nanodot (pulse)	7.0	2.08	7,646,206	60

To further mitigate Joule heating, we downsized the diameter of our current apertures to hundreds of nanometers. **Figure 6.7(a)** schematically illustrates the architecture of PeLEDs with the nanopatterned injection area. A 60 nm-thick SiO_2 was deposited on an ITO electrode as an insulator layer, and a small circular hole (Φ = 100 nm) was defined by electron-beam lithography. HTL, perovskite, ETL and electrode layers are subsequently deposited onto the substrate. The current flows are confined in these nanodot-shaped current apertures, as schematically shown in **Figure 6.7(b)**. To allow the emission to be detected by a photodetector, we fabricated an array of nanodots instead of a single nanodot in the insulator layer. The atomic force microscope (AFM) image presents the surface morphology of the insulator layer, demonstrating the uniformity of the nanodot array (Φ = 100 nm) (**Figure 6.7c**). We also inspected EL emission from nanopatterned PeLEDs (Φ = 1 um) operated at 10 V by an optical microscope in dark field (**Figure 6.7d**). No EL

was observed in the insulating regions, demonstrating that current flow regions are successfully constrained inside the apertures. We enlarged current apertures here due to the diffraction limit of the optical microscope, which makes EL emission from 100 nm-diameter apertures not observable.

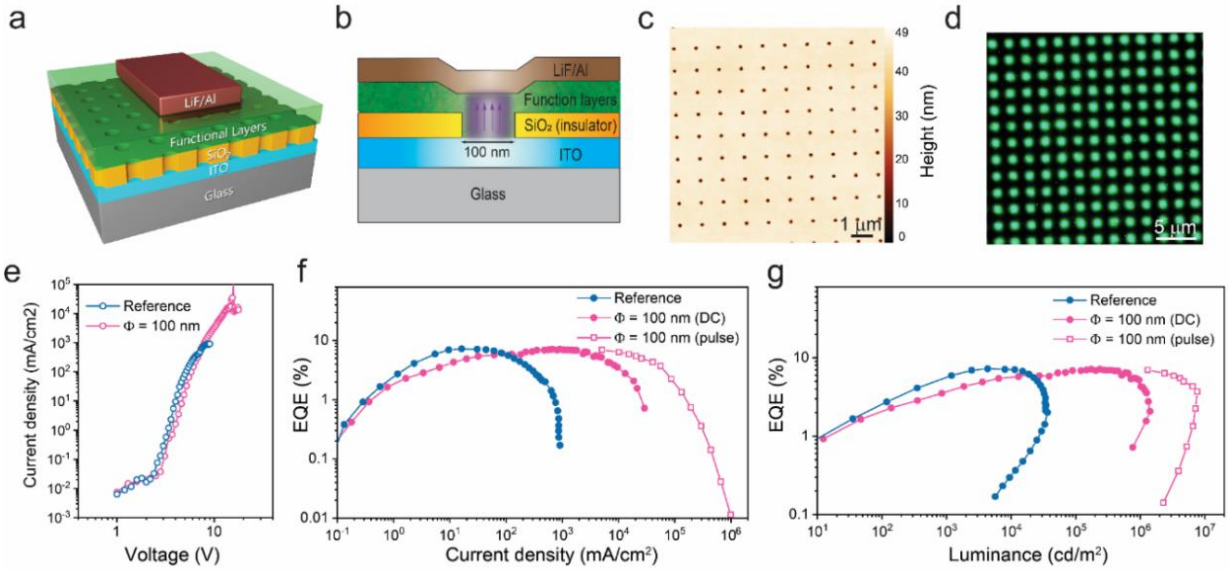

Figure 6.7. Suppressing Joule heating by nanopatterning current injection area. (a) Schematic device structure with nanodot-shaped current apertures in the SiO_2 (insulator) layer. (b) Schematic illustration of current flowing in nanopatterned PeLEDs. The functional layers include HTL, KBr-based perovskite and TPBi. (c) AFM image of the SiO_2 layer. (d) Dark-field optical microscope image of nanopatterned PeLEDs (Φ = 1 μm) under operation at 10 V, showing EL only from patterned current apertures. (e) *J-V* data for reference and nanopatterned PeLEDs (Φ = 100 nm). (f) *EQE-J* and (g) *EQE-L* characteristics for reference, nanopatterned PeLEDs in DC and pulsed current (pulse duration 2 μs, duty cycle 0.2%).

The *J-V* characteristics of nanopatterned and reference PeLEDs measured in DC mode are shown in **Figure 6.7(e)**. The reference devices show a maximum *J* (J_{max}) of ~1 A/cm^2 and voltage of ~9 V before device breakdown. In contrast, no obvious breakdown is observed in nanopatterned

PeLEDs (Φ = 100 nm) until 15 V, and J_{max} could be as high as 28.9 A/cm^2. The *EQE*-*J* and *EQE*-*L* characteristics (**Figure 6.7f, g**) clearly show efficiency roll-off is significantly suppressed for nanopatterned PeLEDs, especially operated in pulsed current mode. The nanopatterned PeLEDs driven by pulsed current achieve J_{max} up to ~1 KA/cm^2 without device failure. The maximum luminance of 7.6 Mcd/m^2 (corresponding to a $J \times EQE$ of 2.1 A/cm^2) is obtained at a J of ~56 A/cm^2, which, to the best of our knowledge, is a record luminance among PeLEDs. Besides, J_c is improved to 60 A/cm^2, a 75-fold enhancement from reference devices. More detailed characteristics are included in **Table 6.4**, and the performance comparisons between our devices in this work and other representative green-emission PeLEDs are summarized in **Table 6.5**. Further optimization of device performance should be achievable by adding the DC bias to the pulse train following the method proposed by Kim *et al.*[218]

We attribute the improved performance from KBr-treated 3D nanopatterned PeLEDs mainly to significantly mitigated Joule heating. However, in theory, this structure can further be used to reduce exciton-polaron annihilation for materials whose charge carrier recombination is dominated by bound excitons. When the current aperture size is close to exciton diffusion length, some excitons can diffuse outside the nanodot-shaped apertures and escape from current flow regions where charge carriers move directionally under electric field, thus suppressing the exciton-polaron interactions.[238, 239]

Table 6.5. Performance comparisons between our devices in this work and state-of art green perovskite LEDs.

EML materials	Voltage (V) at 10^3, 10^4 cd/m^2	L_{max}[a] (cd/m2)	*EQE* (%)	*C.E.*[b] (cd/A)	Publication date
$CsPbBr_3$ QDs	4.1, …	1 660	8.73	26.2	2017[240]
$CsPbBr_3$ NPs	4.1, …	8 353	17.4	54.6	2019[241]

$PEA_2(FAPbBr_3)_{n-1}PbBr_4$	3.6, …	9 120	14.36	62.4	2018[100]
$CsPbBr_3$ QDs	6.2, 10.5	10 206	4.63	8.73	2018[242]
$MA_xCs_{1-x}PbBr_3$	3.2, 4.3	14 000	20.3	78	2018[243]
2D PEABr-$CsPbBr_3$	3.4, 4.4	19 540	15.5	49.1	2018[163]
$MAPbBr_3$	5.55, 8.35	20 000	8.53	42.9	2015[178]
$CsPbBr_3$	3.75, 5	23 828	2.94	9.5	2017[244]
2D PEABr-$CsPbBr_3$	3.4, 4.2	31 012	16.2	50.2	This work
2D BABr-$CsPbBr_3$	3.85, 4.8	33 532	8.42	25.1	2018[245]
$CsPbBr_3$	4.2, 5.2	51 890	4.76	21.4	2017[246]
$CsPbBr_3$	3.1, 4.1	53 525	4.26	15.7	2016[247]
$MA_xCs_{1-x}PbBr_3$	4.8, 6.3	91 000	10.4	33.9	2017[248]
KBr-$CsPbBr_3$ (glass)	3.0, 3.6	120 287	7.7	28.4	This work
KBr-$CsPbBr_3$ (sapphire)	3.2, 4.0	172 650	8.2	30.1	This work
$CsPbBr_3$	2.5, 2.9	496 320	9.3	37	2019[88]
Current-focusing devices (100 nm apertures, DC)	5.5, 6.7	1 417 312	7.2	26.3	This work
Current-focusing devices (100 nm apertures, pulsed current)	NA (Measured in current mode)	7 646 245	7.0	25.6	This work

a. L_{max} means the maximum achieved luminance. b. C.E. means the current efficiency. This table is sorted by ascending the luminance of selected previous reports. Some data of the voltages at 10^3 and 10^4 cd/m^2 are estimated based on the *L-J-V* curves in relevant references. This table is adapted from ref.88 with the permission of AIP Publishing.

Our KBr-based perovskite films exhibit an ASE threshold of ~15 uJ/cm^2 (**Figure A.13**). Based on the extracted k_1, k_2 and k_3, we calculate that a $J \times EQE$ value of 95 A/cm^2 and a luminance of 350 M cd/m^2 are needed to realize electrically pumped lasing (**Figure 6.9**). Currently, the best $J \times EQE$ and luminance achieved here are still one order below the calculated lasing threshold.

However, incorporation of resonance cavities such as distributed feedback (DFB) structures are likely to reduce the lasing threshold, and as such, we believe the electrically pumped PeLDs should be within reach.[89, 212] At the same time, more work should be continued to optimize perovskite materials, heat management, pulse train operation and long-term stability.

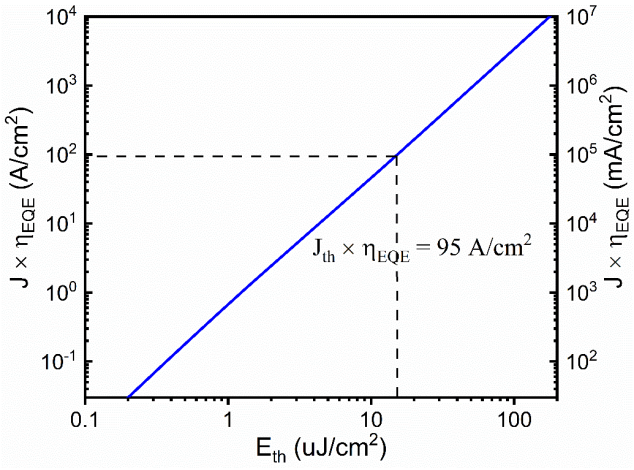

Figure 6.8. The required threshold of $J \times EQE$ under electrical pumping *versus* the ASE threshold under optical pumping.

6.5 CONCLUSION AND OUTLOOK

In summary, we have applied several strategies to suppress efficiency roll-off and improve brightness of PeLEDs. From the aspect of device engineering, we have designed an energy ladder to balance electron and hole injection. In terms of perovskite materials, we replaced quasi-2D perovskites by KBr-treated 3D $CsPbBr_3$ perovskite due to its lower Auger coefficient. From the aspect of heat management, we observed that Joule heating is a key factor leading to efficiency roll-off at high J, both by thermal imaging and by comparing the performance of glass- and sapphire-based devices. To further suppress the Joule heating of PeLEDs, we applied a current-focusing architecture with micro and nano-size current apertures. The nanopatterned PeLEDs

show a record luminance of 7.6 Mcd/m^2, furthermore, the devices can be operated at a high *J* up to 1 KA/cm^2. Our work provides a route to achieve efficient, high-brightness PeLEDs with low efficiency roll-off. It also demonstrates the potential of perovskites for realizing solution-processed laser diodes with further optimization of the materials and devices.

Chapter 7. CONCLUSION AND PROSPECTS

7.1 SUMMARY OF THIS DISSERTATION

Metal halide perovskites show remarkable optoelectronic properties, they are regarded as outstanding candidates not only for applications of solar cells, but also LEDs and lasers. We focus on light-emitting applications of hybrid perovskites in this dissertation. The high PLQY, good charge transport, tunable emission wavelength and narrow emission bandwidth stands out perovskites as an excellent solution-processed light-emitter. High-performance PeLEDs have been demonstrated by many groups, showing the robustness and reproducibility of fabrication techniques for perovskite optoelectronics. Up to now, the EQEs over 21%, 21%, 20% and 10% have been achieved for near infrared, red, green, blue emission PeLEDs. The development of perovskite materials has reach into a relative mature stage. The next step is to improve the stability especially operational stability of perovskite-based devices. Perovskite emitters also present great coherent emission properties, renewing people's hope for developing a solution-processed electrically driven laser diode. A great variety of optically pumped perovskite lasers under short-pulse pumping have been demonstrated in last several years. Recently, several CW-pumped perovskite lasers have also been demonstrated at cryostat temperature. Pump-induced thermal heat and photo-induced defects that increase nonradiative Shockley-Read-Hall rates may be the challenges to achieve CW lasing at room temperature. Based on the progress of optically pumped perovskite lasers, it will be very interesting to explore the possibility of perovskite emitters for electrically driven lasers.

In Chapter 2, we analyzed the optical energy losses in PeLEDs and found the light outcoupling efficiency of PeLEDs is restricted to 20-25% in current architectures. We believe the next step to boost the performance of PeLEDs should be focused on light extraction management, considering

the material development has been relatively sufficient. We demonstrate the orientation of transitional dipole moment plays an important role in determining the outcoupling efficiency. Horizontally orientated dipoles are preferred over vertically orientated dipoles in terms of maximizing light extraction. Besides the dipole orientation, the light outcoupling efficiency is also largely affected by the refractive index, thickness of the perovskite emitter. We found the outcoupling efficiency is more sensitive to refractive index for thick perovskite emitters compared to thin perovskite emitters. These findings can provide guidance on routes to design a high-efficiency PeLED through light extraction management.

In Chapter 3, I present our previous work on red-emission perovskite quantum dots. Compared to organic-inorganic hybrid perovskite such as $MAPbI_3$ and $FAPbI_3$, all-organic perovskite should be more stable as it is not easy for cesium cation to decompose and degrade, even at high temperature. However, it is difficult to keep $CsPbI_3$ bulk films in stable cubic phase in ambient conditions, presumably due to relatively small Goldschmidt's tolerance factor. To overcome this issue, the large surface tension of nanocrystal structure is utilized to keep $CsPbI_3$ in stable cubic phase. The synthesis procedures of $CsPbI_3$ nanocrystals are of importance in determining the environmental stability. Me(OAc) is selected to wash organic ligands and avoid aggregation of nanocrystals. The as-synthesized $CsPbI_3$ nanocrystals could maintain cubic phase for more than 2 months at ambient conditions. We further built up red-emission PeLEDs based on $CsPbI_3$ nanocrystal emissions. The devices show a decent EQE of 0.21% (compare to literatures in or before 2017) and good operational stability. The luminance drops to 50% of the initial value after 16 hours' continuous operation. The much difference between environmental stability and operational stability is due to different degradation mechanism. The ion migration is considered as the main factor in affecting operational stability. Under high electric field, halide vacancies can

migrate across entire device stack, leading to distortion of perovskite crystals, corrosion of metal electrodes and electrochemical reactions at the interfaces. In contrast, the moisture and oxygen exposures are main degradation pathways in terms of environment stability.

In Chapter 4, we developed a high-resolution photolithographic method to pattern multicolor perovskite films for LCD and mirco-LED displays. It is always of interest and profit to apply semiconductor emitters in displays, which requires discontinuous miniaturized pixels. Top-down photolithography is a preferred fabrication method in industry, which requires cost-effective manufacturing. However, patterning perovskite films is not easy considering the compatibility of perovskite with common polar solvents in photolithography. Therefore, we developed a dry lift-off method based on an intermediate layer (parylene) to avoid contacts between perovskite films and solvents. This approach can provide a high resolution with line features as small as 4 μm. In addition, this approach is very generic and can be applied to pattern many types of perovskites including quasi-2D, 3D, vacuum-deposited perovskites and perovskite QDs. Our method provides a generic route to pattern perovskite films, which may also be beneficial to laser applications, e.g. perovskite microdisks can be patterned using this approach to form WGM lasers.

In Chapter 5, optically pumped perovskite lasers based on DBR and DFB cavities are demonstrated. The facile solution processability make it easy to integrate perovskite films with various optical cavities. For the perovskite VCSEL, perovskite QD emitter was embedded between two highly reflective DBRs, which can provide a high quality factor. We compromised the conflict between thick gain medium and single-mode lasing, and finally achieved a low-threshold (0.39 $\mu J/cm^2$) perovskite VCSEL with single-mode emission. Besides, we characterized the temperature-dependent lasing threshold, which is consistent with empirical exponential relationship. In addition to the VCSEL structure, we spin coated a $MAPbBr_3$ film onto a SiO_2

grating to constitute a second-order DFB laser. The beam dose was optimized in electron beam lithography to fabricate a high-quality grating. K-space imaging technique was adopted to confirm polarized emissions from the perovskite DFB devices. Both perovskite VCSEL and DFB laser devices can be operated under nanosecond-pulse pumping, further optimization on thermal management and Auger recombination suppression are required to achieve CW-pumped lasing. This work on cavity-integrated perovskite laser under optical pumping provides helpful guidance and paves the way for designing an electrically driven perovskite laser.

In Chapter 6, we achieved a PeLED that could be operated at a high current density up to 1kA/cm^2. Most of previous reported PeLEDs show a peak EQE at a low current density (J < 1 mA/cm^2), then the EQE starts to decrease dramatically, which is a big obstacle towards electrically driven lasers. In this work, we significantly suppressed the efficiency roll-off after applying combined strategies including charge injection balance, Auger recombination reduction and thermal management. An extremely high $J \times EQE$ of 2.1 A/cm^2 has been demonstrated. Although this value is still one order lower than the theoretical threshold of 95 A/cm^2, we believe the electrical driven laser is within reach if we can integrate thermal sink to our devices for the purpose of improving heat dissipation and optimize the DFB cavity for the purpose of reducing required lasing threshold. Material optimization is also desired to make perovskites more stable and robust.

7.2 FUTURE WORK OUTLOOK

As an emerging candidate in solution-processed emitters, perovskites show even superior optoelectronic properties than previous leading contenders such as organic semiconductors and colloidal nanocrystals. Therefore, the continued development of perovskite light-emitting devices should be of great interest and importance for next-generation display and laser applications. In

this section, I will highlight some future research directions which I feel are very important in perovskite research community.

PeLED is still one of big and hot research topics for perovskite emitters. Considering the highest EQE achieved up to now has reached the theoretical limit, I want to emphasize the next step to improve the device efficiency should be focused on light extraction management. Designing and integrating photonic nanostructures with PeLED structures can increase the power fraction of outcoupled light, which is an effective method to improve PeLED efficiencies. Meanwhile, engineering the properties of perovskite emitters including the dipole orientation, refractive index and thickness can also bring in benefits. Among PeLEDs with various emission colors, the development of blue PeLEDs seems to lag behind green and red counterparts. The relatively low PLQY of blue perovskite emitters and inefficient charge injection due to deep valence band are two reasons accounting for the sluggish development of blue PeLEDs. Corresponding countermeasures should be carried out to improve device efficiency of blue PeLEDs, which is very important for developing multicolor display based on RGB primary colors. Besides continuing to boost device efficiency, PeLEDs must come out of aging. The operational stability needs to be significantly improved. Up to now, the half-lifetime of ~ 100 hours have been achieved with the initial luminance at 100 cd/m^2.[52] However, it still can't meet the standard of industry and daily applications. In the future, the PeLED lifetime should exceed at least 10^4 hours to compete with commercialized colloidal nanocrystals.

The applications of perovskite emitters in displays is of interest and full of promise. The facile bandgap tunability enables a broad emission spectral range covering from UV to NIR, leading to a wide color gamut (≈140%) that is broader than the National Television System Committee (NTSC) standard on a CIE chromaticity diagram. Perovskite emitters have narrow and symmetric

PL peaks (FWHM ≈ 12-40 nm, which is even better than traditional colloidal nanocrystals).[208] We have developed a generic photolithographic method to pattern perovskite films, which can be compatible with industrial manufacturing. Prototype perovskite LCD and micro-LED displays have been demonstrated and show considerable performance. We believe most of technical obstacles towards commercialized displays have been addressed. However, the perovskite micro-LED array shown in our work is still only a prototype. The shortcoming of this prototype display is that it can only display static images which are pre-patterned. For a real commercial display, each pixel should be able to turn on/off individually, comprising dynamic images. In future work, we plan to pattern the ITO electrode, the perovskite film and the top electrode in order to control LED pixels individually. In this case, patterning perovskite films will be vital to avoid crosstalk between individual pixels. In addition, RGB micro-LED pixels can be fabricated on the same substrate with the same ETL and EHL. The potential problem is the maximum efficiency and brightness of RGB pixels may not be uniform considering different energy levels of RGB perovskite films. However, the brightness of each pixel can be individually controlled by the amount of current flowing to that pixel, so strategies to achieve uniform RGB pixels and thus a high-quality RGB display should be within reach.

Researchers have been searching a solution-processed emitter that can be used to achieve electrically driven laser for almost three decades. In view of great optoelectronic properties including high optical gain, 'bright' triplet state and low defect density, perovskites renew people's hope for pursuing this long-standing goal. Achieving optically pumped lasing, especially under CW pumping is considered as an important step towards electrically pumped lasing. Contemporarily, there is no difficulty overseen in achieving perovskite lasers under short-pulse optical pumping. As for CW lasing of perovskites, even though several groups have reported it at

room temperature, they still need more evidence to support their findings.[20-22] Currently, it is still not very clear about the reasons that cause lasing death under CW pumping. However, it seems like triplet accumulation, which often happens in organic lasers, is not a big issue in perovskite materials.[249] Thermal management to reduce pump-induced joule heat, together with efforts on reducing required lasing threshold should be the next research direction to overcome the challenges for CW-pumped perovskite lasers at room temperature.

On the basis of our results on optically pumped perovskite DBR and DFB lasers, and progress on suppressing efficiency roll-off and injecting intense current to PeLEDs, we further plan to incorporate a well-designed optical cavity into the PeLED device architecture to build up an electrically driven laser device. For the VCSEL structure, the difficulties for the transition from optically pumped to electrically pumped lasers lie in the transparent (non-absorption) metal and deposition of the top DBR mirror. Two electrodes are required in the electrically driven VCSEL to inject electrons and holes. On the other hand, to ensure the gain exceed the loss inside the cavity, we need to minimize the light absorption of electrodes. Currently, we use ITO as bottom electrode and Al as top electrode. In this case, the thickness of top Al electrode should be reduced to minimize the loss when light pass through it. A 10nm-thick Al film may be desired. Besides, the deposition temperature for the top DBR mirror should be less than 100 ℃, otherwise, perovskite films may be degraded by thermal heat. However, a low-temperature deposition may deteriorate the quality of top DBR mirror. For electrically driven DBR laser, it seems easier to integrate the DFB grating with the PeLED structure. A layer of SiO_2 grating between ITO and HTL can work as the DFB resonant cavity and current aperture at the same time. The deposition procedures for other layers should not be affected. The grating depth, period and duty cycle should be designed

carefully to maximize the optical confinement factor in the perovskite layer, which increases the gain of light traveling inside the resonant cavity.

We have tried to incorporate a SiO_2 grating into the PeLED architecture to build up the electrically driven device (**Figure A.14**). However, only broad EL emissions were observed, no narrow lasing peaks emerged. There are many reasons accounting for this unsatisfied result. First, we believe the $J \times EQE$ value is still not high enough to surpass the lasing threshold, as we have mentioned above. The population inversion has not been built up. Second, the calculated lasing threshold under electrical pumping is based on the optically pumped threshold, which is measured under a short-pulse pump laser. However, the electrical pulse usually has a longer pulse duration, e.g. the shortest current pulse we can provide based on our equipment is 100 ns. Therefore, finding a perovskite material that can lase under long-pulse pumping (microsecond level) is very important for achieving electrically driven perovskite laser. For example, Adachi group first demonstrated an optically pumped BSBCz-based DFB laser under a long-pulse photoexcitation of 30 ms.[24] Based on this excellent emitter, they further successfully achieved a current-injection DFB laser under 400ns voltage pulse pumping.[250] Perovskite single crystals have very low defect densities (down to 10^9-10^{10} cm^{-3}), high carrier mobilities (hundreds of $cm^2V^{-1}s^{-1}$) and smooth surfaces that can reduce scattering loss, making them good candidates for lasing applications. However, although some works on optically pumped perovskite single crystal laser have been covered, LEDs based on perovskite single crystals have been rarely reported. More studies in this field are required to explore the potential of perovskite single crystals for electrically pumped lasing applications. At last, the ion migration could be very severe at high injection current, the stability thus become a big issue. It is possible that there are lasing events at the beginning (maybe first several pulses) and the lasing death occurs very quickly. Adachi group also found the lasing only happens in first

20 pulses and then disappear for their devices.[24] Therefore, we may need to synchronize the spectrometer to the pulse generator for the purpose of analyzing the emission spectra revolution with the number of electrical pulses.

In summary, from studies of fundamental properties, to the implementation in commercialized applications of next-generation LED and displays, or the technology breakthrough of solution-processed electrically driven perovskite lasers, there are endless possibilities for the exploration and future impact of these great perovskite emitters.

Appendix A. Supporting Information

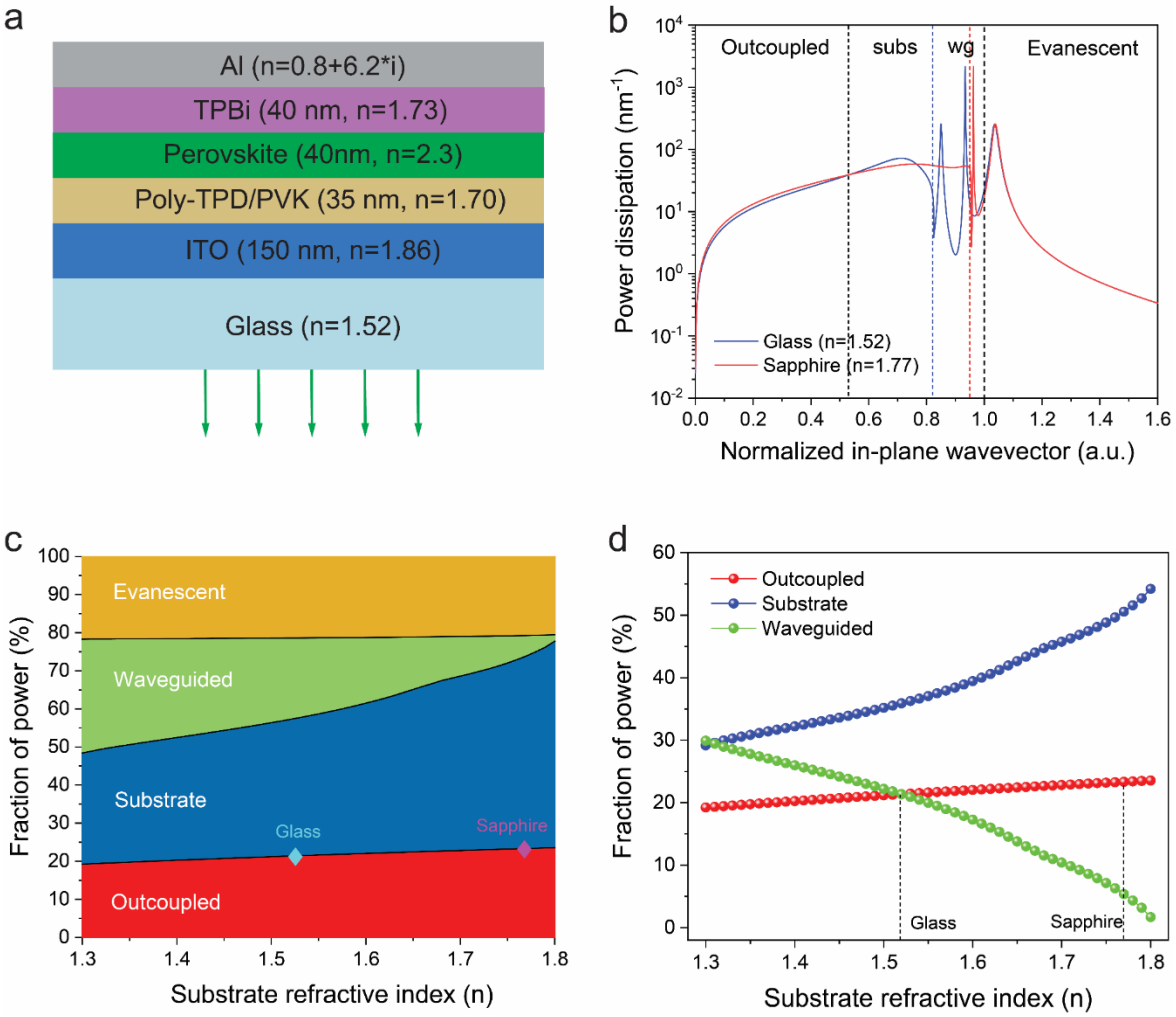

Figure A.1. The optical simulations of light outcoupling from PeLEDs. (a) The device structure of PeLEDs for simulation. The thickness and refractive index (n) of each layer are included. (b) Simulated power dissipation *versus* normalized in-plane wave vector (k_x) at λ = 513 nm for glass- (n = 1.52) and sapphire-based (n = 1.77) devices. The blue and red dashed lines represent the boundary between substrate and waveguided modes in glass- and sapphire-based devices. In outcoupled mode, it is clearly observed that power dissipation of sapphire-based device is slightly higher than that of glass-based devices (c) Power distribution in different optical modes with various refractive indices of the substrate. (d) The dependence of outcoupled, substrate and waveguided power proportions on the refractive index of the substrate.

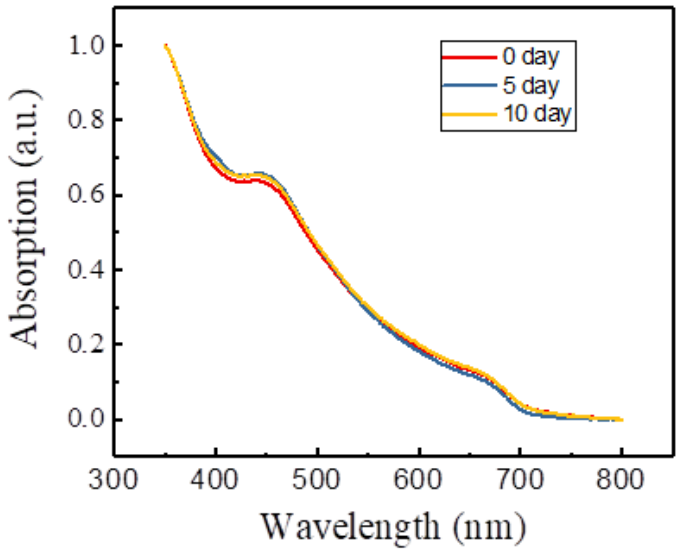

Figure A.2. Outstanding stability of $CsPbI_3$ QDs purified by Me(OAc). Ultraviolet-visible absorption spectra, normalized at 350 nm, of $CsPbI_3$ QDs synthesized at 170 °C and stored in ambient conditions for 5 and 10 days, respectively. There is no obvious change observed in the absorption spectra.

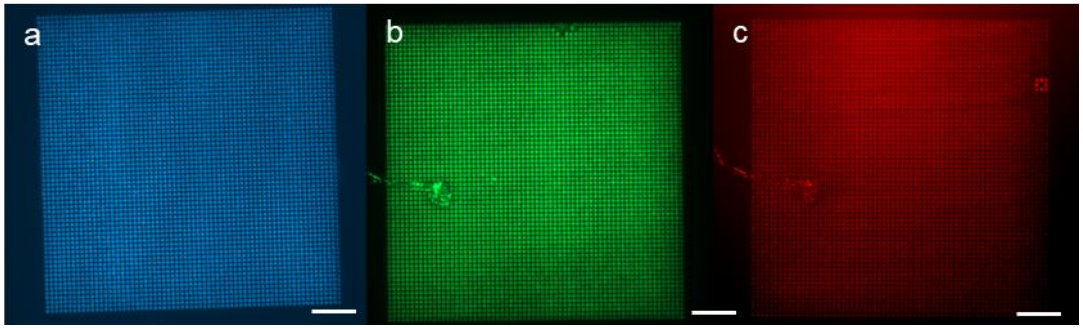

Figure A.3. 10 μm-diameter RGB perovskite circles. (a)-(c) Blue, green and red 10 μm-diameter perovskite circles (scale bar 200 μm)

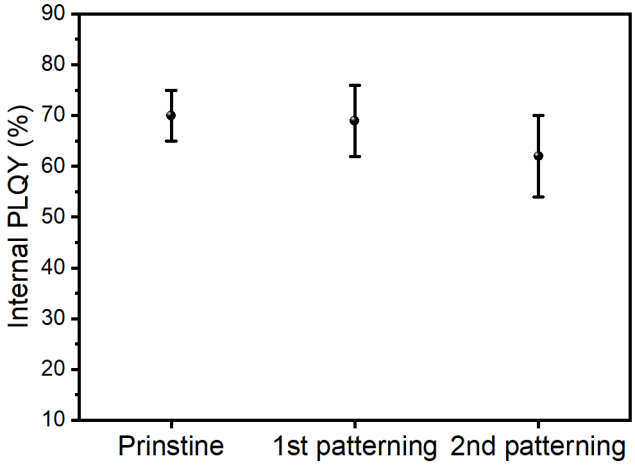

Figure A.4 PLQY evolution of quasi-2D green perovskite films before and after multicolor patterning.

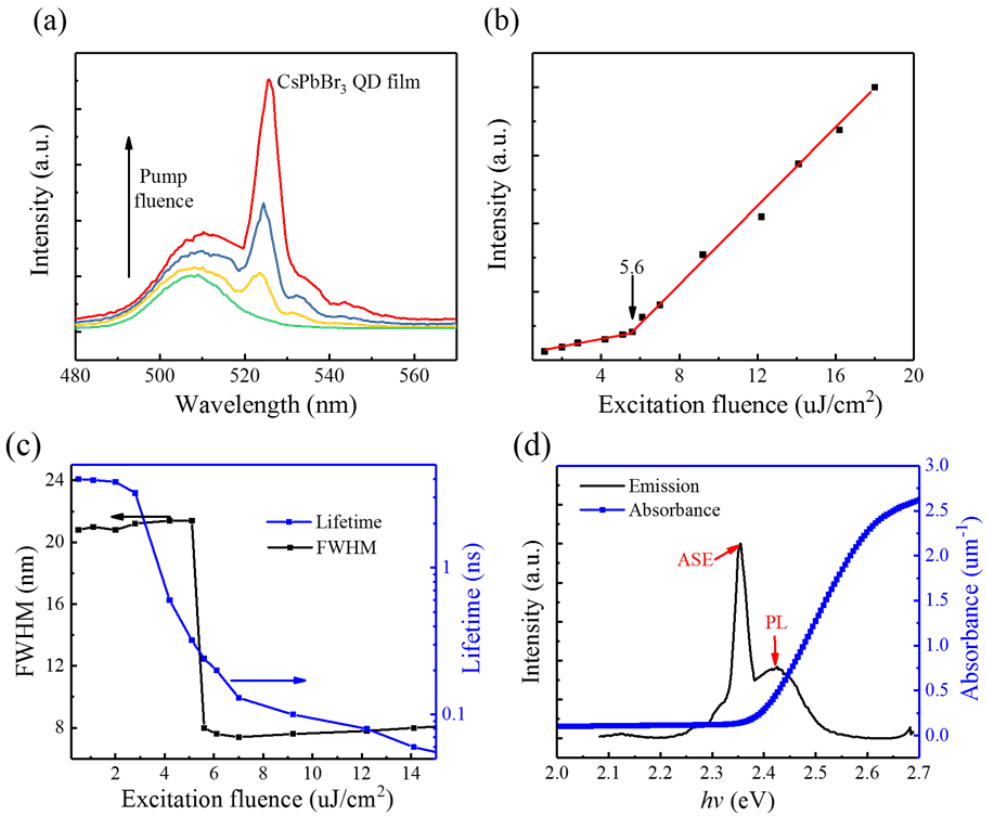

Figure A.5. ASE from the CsPbBr3 QD thin film under femtosecond excitation. (a) Evolution of emission spectra with increasing pump fluence. (b) Dependence of extracted emission intensity of the ASE peak on excitation fluence. (c) FWHM of the emission peak and average time-resolved PL lifetime as a function of the excitation fluence. (d) ASE emission spectrum and Tauc plot of direct-bandgap absorption.

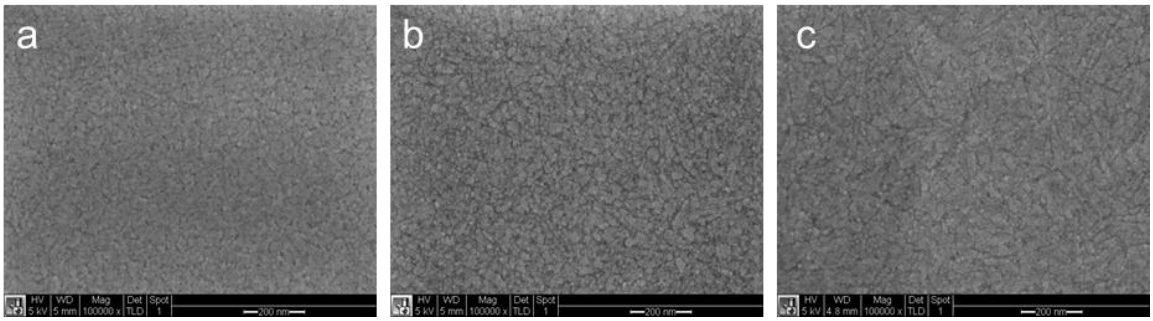

Figure A.6. The surface morphologies of quasi-2D perovskite films formed on different HTLs. (a) PEDOT:PSS, (b) PEDOT:PSS/TFB/PVK, and (c) poly-TPD/PVK. The scale bar is 200 nm. These films show similar surface morphologies without obvious pinholes, demonstrating smooth and continuous perovskite films were formed on different HTLs. We found these films exhibit small crystallite size because the presence of PEABr impedes the perovskite crystal growth, thus enhancing the exciton confinement.

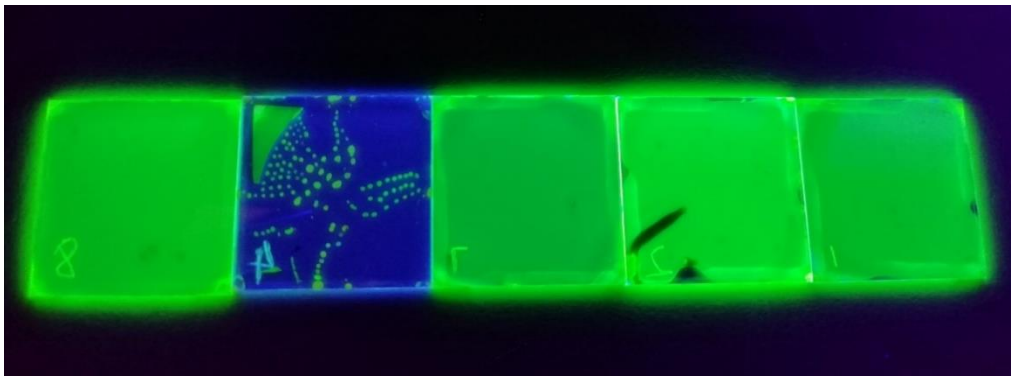

Figure A.7. The optical images of perovskite films prepared on different HTLs (from left to right): glass (reference), poly-TPD, O_2 plasma briefly treated poly-TPD, poly-TPD/PVK and PEDOT: PSS/TFB/PVK.

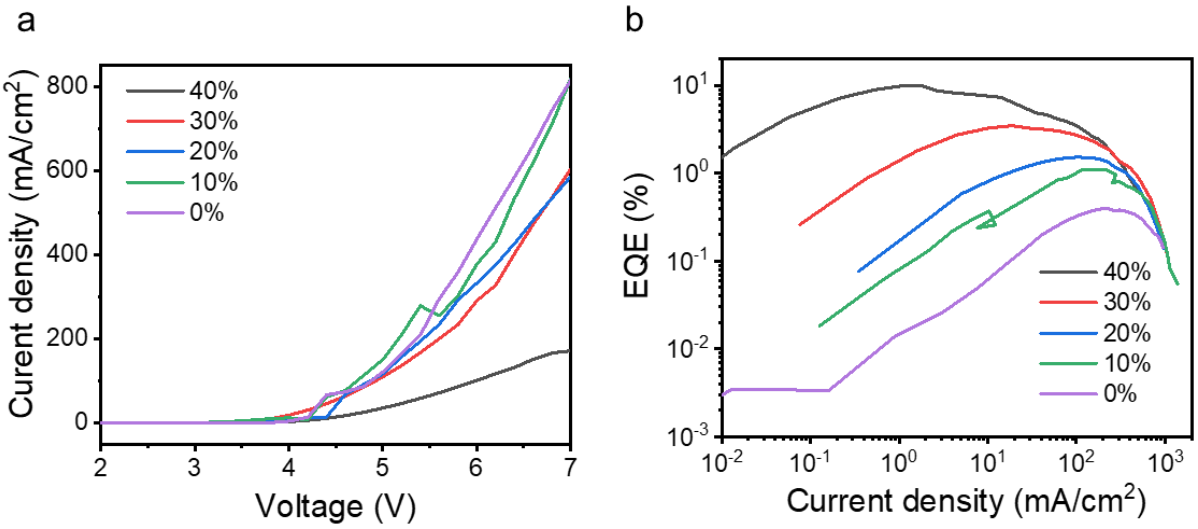

Figure A.8. The performance characterizations of quasi-2D PeLEDs $(PEABr)_x(CsPbBr_3)$ with the x value from 0 to 40% (x means the molar ratio of PEABr to $CsPbBr_3$). The HTL here is PEDOT:PSS. (a) *J-V* and (b) *EQE-J* characteristics. For quasi-2D perovskites $(PEABr)_x(CsPbBr_3)$, the x value ranges from 0 to 40%. It is observed that the electrical conductivity becomes worse when x increases, this is because the organic component PEABr is insulating. However, the EQE increase with increasing x value, which is due to better exciton confinement in the quantum wells. The EQE is almost the same for different x values at high current density, indicating that the exciton confinement effect diminishes at high current densities and possible joule heating damage to devices.

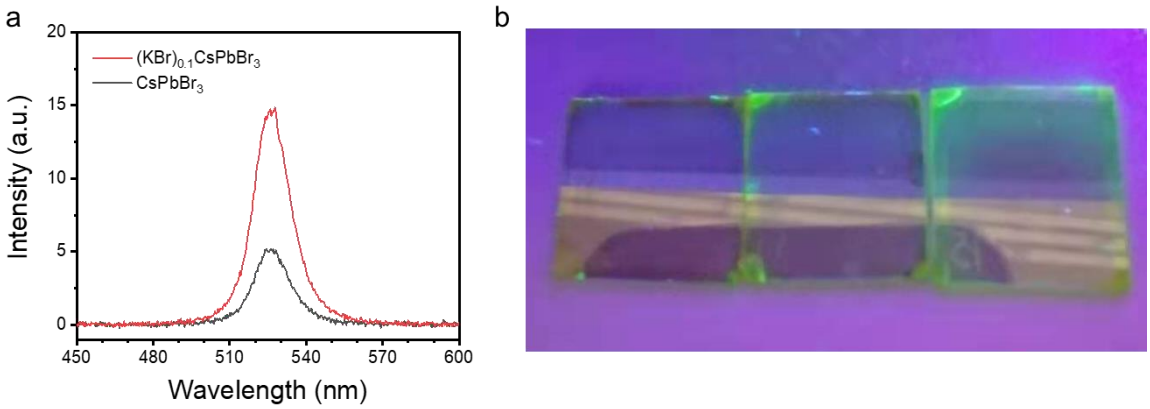

Figure A.9. (a) The PL spectra of $(KBr)_{0.1}CsPbBr_3$ and $CsPbBr_3$ films. Compared to pure $CsPbBr_3$, the additive of 10% KBr greatly enhances the PL. (b) The real photos of perovskite films under UV lamp excitation, the additive of KBr is 0, 5, and 10% from left to right.

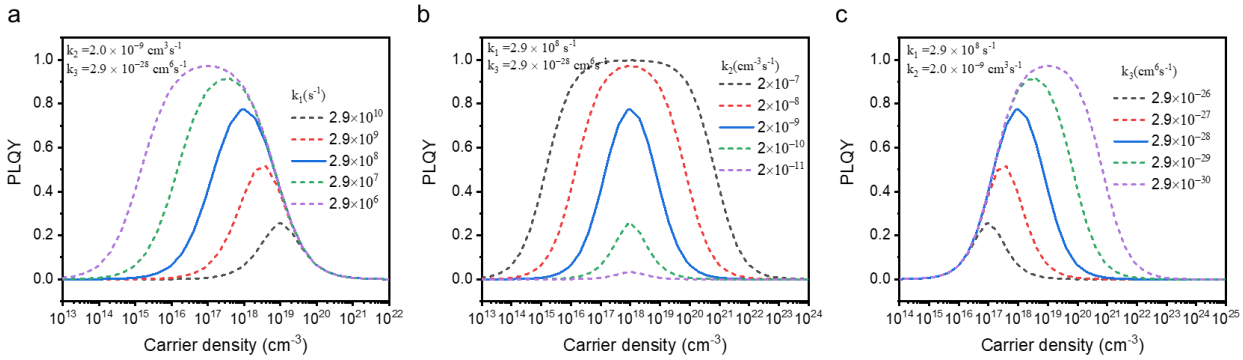

Figure A.10. The calculated internal PLQY of 3D perovskite films based on recombination rates fitted from transient PL decay. (a) The effect of k_1 on PLQY with k_2, k_3 fixed. (b) The effect of k_2 on PLQY with k_1, k_3 fixed. (c) The effect of k_3 on PLQY with k_1, k_2 fixed. To achieve high EQE at high current densities, we prefer k_2 to be large, k_1 and k_3 to be small for 3D perovskites.

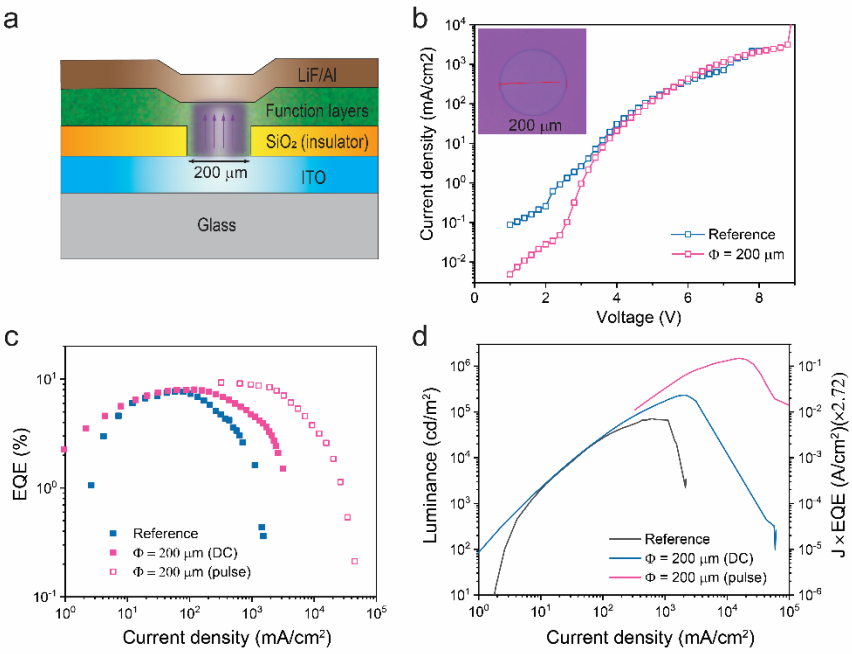

Figure A.11. Current-focusing devices with micro-size current aperture. (a) Schematic device structure, the functional layers include poly-TPD/PVK, KBr-treated 3D perovskite and TPBi. (b) *J-V* data for reference (active area 2 × 2 mm^2) and current-focusing devices (diameter Φ = 200 μm), measured in DC. (c) *EQE-J* and (d) *L-J×EQE-J* characteristics for reference devices, current-focusing devices in DC and pulsed current (pulse duration 2 μs, duty cycle 0.2%).

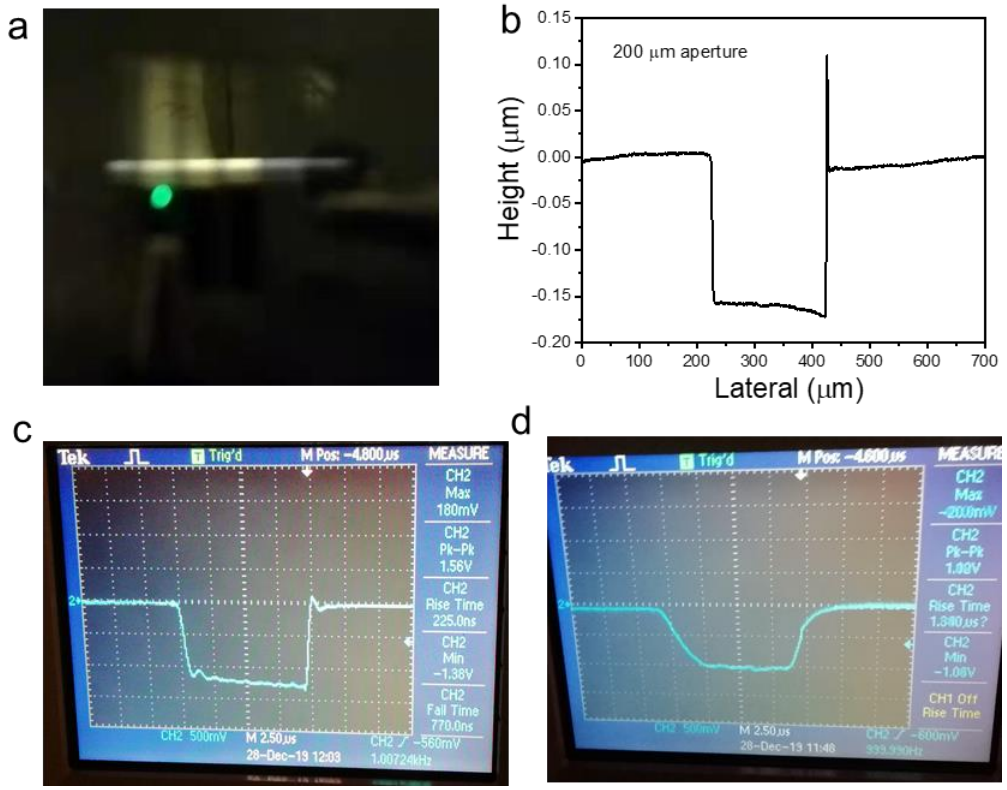

Figure A.12. (a) The real photo of micro-size current-focusing devices under operation. The green light comes from the current aperture, no EL was observed in the insulating area. (b) The profilometer data, showing the current aperture has a diameter of 200 μm and a height of ~ 150 nm. (c) The EL response under pulsed current (2 μs pulse width) for KBr-based and (d) PEABr-based PeLEDs. The response time is 0.225 μs for KBr-based devices, which is much shorter than that of PEABr-based devices (1.8 μs), this is consistent with the better electrical conductivity of KBr-treated 3D perovskite films.

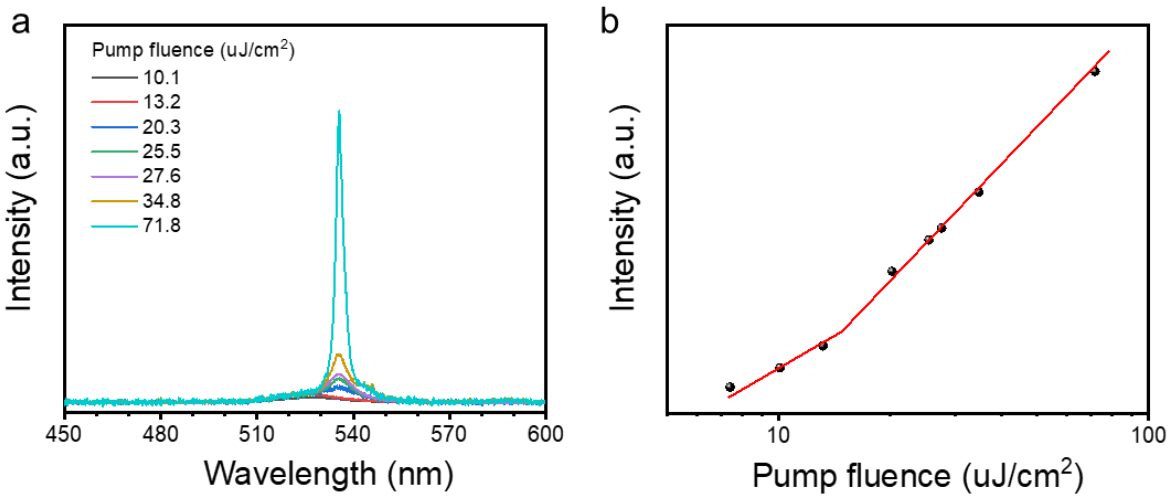

Figure A.13. The ASE characterization of KBr-treated 3D perovskite films. (a) The emission spectrum of perovskite films under different pump fluence. (b) The plot of emission intensity recorded at ASE peak (536 nm) as a function of pump fluence, the ASE threshold is about 15 uJ/cm^2.

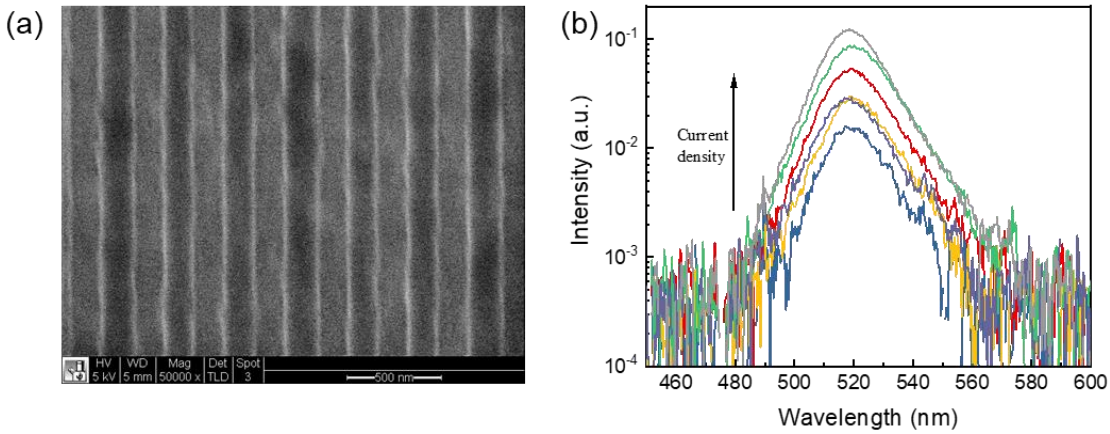

Figure A.14. Electrically driven perovskite DFB laser devices. (a) Planar SEM image of the second order SiO_2 grating. (b) EL spectra at increasing current densities, no lasing peaks were observed.

REFERENCES

(1) Dou, L. T.; Yang, Y.; You, J. B.; Hong, Z. R.; Chang, W. H.; Li, G.; Yang, Y. Solution-processed hybrid perovskite photodetectors with high detectivity. *Nat. Commun.* **2014,** *5*.
(2) Green, M. A.; Ho-Baillie, A.; Snaith, H. J. The emergence of perovskite solar cells. *Nat. Photonics* **2014,** *8*, 506-514.
(3) Veldhuis, S. A.; Boix, P. P.; Yantara, N.; Li, M.; Sum, T. C.; Mathews, N.; Mhaisalkar, S. G. Perovskite Materials for Light-Emitting Diodes and Lasers. *Adv. Mater.* **2016,** *28*, 6804-6834.
(4) Yang, W. S.; Park, B. W.; Jung, E. H.; Jeon, N. J.; Kim, Y. C.; Lee, D. U.; Shin, S. S.; Seo, J.; Kim, E. K.; Noh, J. H.; Seok, S. I. Iodide management in formamidinium-lead-halide-based perovskite layers for efficient solar cells. *Science* **2017,** *356*, 1376-1379.
(5) Cho, H.; Jeong, S. H.; Park, M. H.; Kim, Y. H.; Wolf, C.; Lee, C. L.; Heo, J. H.; Sadhanala, A.; Myoung, N.; Yoo, S.; Im, S. H.; Friend, R. H.; Lee, T. W. Overcoming the electroluminescence efficiency limitations of perovskite light-emitting diodes. *Science* **2015,** *350*, 1222-5.
(6) Yuan, M.; Quan, L. N.; Comin, R.; Walters, G.; Sabatini, R.; Voznyy, O.; Hoogland, S.; Zhao, Y.; Beauregard, E. M.; Kanjanaboos, P.; Lu, Z.; Kim, D. H.; Sargent, E. H. Perovskite energy funnels for efficient light-emitting diodes. *Nat Nanotechnol* **2016,** *11*, 872-877.
(7) Zheng, X.; Yuan, S.; Liu, J.; Yin, J.; Yuan, F.; Shen, W.-S.; Yao, K.; Wei, M.; Zhou, C.; Song, K.; Zhang, B.-B.; Lin, Y.; Hedhili, M. N.; Wehbe, N.; Han, Y.; Sun, H.-T.; Lu, Z.-H.; Anthopoulos, T. D.; Mohammed, O. F.; Sargent, E. H.*; et al.* Chlorine Vacancy Passivation in Mixed Halide Perovskite Quantum Dots by Organic Pseudohalides Enables Efficient Rec. 2020 Blue Light-Emitting Diodes. *ACS Energy Lett.* **2020,** *5*, 793-798.
(8) Abdi-Jalebi, M.; Andaji-Garmaroudi, Z.; Cacovich, S.; Stavrakas, C.; Philippe, B.; Richter, J. M.; Alsari, M.; Booker, E. P.; Hutter, E. M.; Pearson, A. J.; Lilliu, S.; Savenije, T. J.; Rensmo, H.; Divitini, G.; Ducati, C.; Friend, R. H.; Stranks, S. D. Maximizing and Stabilizing Luminescence from Halide Perovskites with Potassium Passivation. *Nature* **2018,** *555*, 497-501.
(9) Braly, I. L.; DeQuilettes, D. W.; Pazos-Outón, L. M.; Burke, S.; Ziffer, M. E.; Ginger, D. S.; Hillhouse, H. W. Hybrid Perovskite Films Approaching the Radiative Limit with over 90% Photoluminescence Quantum Efficiency. *Nat. Photonics* **2018,** *12*, 355-361.
(10) Zhao, B.; Bai, S.; Kim, V.; Lamboll, R.; Shivanna, R.; Auras, F.; Richter, J. M.; Yang, L.; Dai, L.; Alsari, M.; She, X.-J.; Liang, L.; Zhang, J.; Lilliu, S.; Gao, P.; Snaith, H. J.; Wang, J.; Greenham, N. C.; Friend, R. H.; Di, D. High-Efficiency Perovskite-Polymer Bulk Heterostructure Light-Emitting Diodes. *Nat. Photonics* **2018,** *12*, 783-789.
(11) Jia, Y.; Kerner, R. A.; Grede, A. J.; Brigeman, A. N.; Rand, B. P.; Giebink, N. C. Diode-pumped Organo-Lead Halide Perovskite Lasing in a Metal-clad Distributed Feedback Resonator. *Nano Lett.* **2016,** *16*, 4624-4629.
(12) Whitworth, G. L.; Harwell, J. R.; Miller, D. N.; Hedley, G. J.; Zhang, W.; Snaith, H. J.; Turnbull, G. A.; Samuel, I. D. Nanoimprinted Distributed Feedback Lasers of Solution Processed Hybrid Perovskites. *Opt. Express* **2016,** *24*, 23677-23684.
(13) Saliba, M.; Wood, S. M.; Patel, J. B.; Nayak, P. K.; Huang, J.; Alexander-Webber, J. A.; Wenger, B.; Stranks, S. D.; Hörantner, M. T.; Wang, J. T. W.; Nicholas, R. J.; Herz, L. M.; Johnston, M. B.; Morris, S. M.; Snaith, H. J.; Riede, M. K. Structured Organic–inorganic Perovskite Toward a Distributed Feedback Laser. *Adv. Mater.* **2016,** *28*, 923-929.

(14) Chen, S.; Roh, K.; Lee, J.; Chong, W. K.; Lu, Y.; Mathews, N.; Sum, T. C.; Nurmikko, A. A Photonic Crystal Laser from Solution Based Organo-lead Iodide Perovskite Thin Films. *ACS Nano* **2016,** *10*, 3959-3967.
(15) Cha, H.; Bae, S.; Lee, M.; Jeon, H. Two-dimensional Photonic Crystal Bandedge Laser with Hybrid Perovskite Thin Film for Optical Gain. *Appl. Phys. Lett.* **2016,** *108*, 181104.
(16) Chen, S. T.; Roh, K.; Lee, J.; Chong, W. K.; Lu, Y.; Mathews, N.; Sum, T. C.; Nurmikko, A. A Photonic Crystal Laser from Solution Based Organo-Lead Iodide Perovskite Thin Films. *Acs Nano* **2016,** *10*, 3959-3967.
(17) Evans, T. J. S.; Schlaus, A.; Fu, Y.; Zhong, X.; Atallah, T. L.; Spencer, M. S.; Brus, L. E.; Jin, S.; Zhu, X. Y. Continuous-Wave Lasing in Cesium Lead Bromide Perovskite Nanowires. *Adv. Opt. Mater.* **2018,** *6*.
(18) Brenner, P.; Bar-On, O.; Jakoby, M.; Allegro, I.; Richards, B. S.; Paetzold, U. W.; Howard, I. A.; Scheuer, J.; Lemmer, U. Continuous Wave Amplified Spontaneous Emission in Phase-Stable Lead Halide Perovskites. *Nat. Commun.* **2019,** *10*, 988.
(19) Jia, Y.; Kerner, R. A.; Grede, A. J.; Rand, B. P.; Giebink, N. C. Continuous-Wave Lasing in an Organic-Inorganic Lead Halide Perovskite Semiconductor. *Nat. Photonics* **2017,** *11*, 784-788.
(20) Li, Z.; Moon, J.; Gharajeh, A.; Haroldson, R.; Hawkins, R.; Hu, W.; Zakhidov, A.; Gu, Q. Room-Temperature Continuous-Wave Operation of Organometal Halide Perovskite Lasers. *ACS Nano* **2018,** *12*, 10968-10976.
(21) Wang, L.; Meng, L.; Chen, L.; Huang, S.; Wu, X.; Dai, G.; Deng, L.; Han, J.; Zou, B.; Zhang, C.; Zhong, H. Ultralow-Threshold and Color-Tunable Continuous-Wave Lasing at Room-Temperature from In Situ Fabricated Perovskite Quantum Dots. *J Phys Chem Lett* **2019,** *10*, 3248-3253.
(22) Tian, C.; Tong guo, T. g.; Zhao, S.; Zhai, W.; Ge, C.; Ran, G. Low-threshold room-temperature continuous-wave optical lasing of single-crystalline perovskite in a distributed reflector microcavity. *RSC Advances* **2019,** *9*, 35984-35989.
(23) Sutherland, B. R.; Sargent, E. H. Perovskite photonic sources. *Nat. Photonics* **2016,** *10*, 295-302.
(24) Sandanayaka, A. S.; Matsushima, T.; Bencheikh, F.; Yoshida, K.; Inoue, M.; Fujihara, T.; Goushi, K.; Ribierre, J.-C.; Adachi, C. Toward continuous-wave operation of organic semiconductor lasers. *Science advances* **2017,** *3*, e1602570.
(25) Grim, J. Q.; Christodoulou, S.; Di Stasio, F.; Krahne, R.; Cingolani, R.; Manna, L.; Moreels, I. Continuous-wave biexciton lasing at room temperature using solution-processed quantum wells. *Nat Nanotechnol* **2014,** *9*, 891-5.
(26) Fan, F.; Voznyy, O.; Sabatini, R. P.; Bicanic, K. T.; Adachi, M. M.; McBride, J. R.; Reid, K. R.; Park, Y. S.; Li, X.; Jain, A.; Quintero-Bermudez, R.; Saravanapavanantham, M.; Liu, M.; Korkusinski, M.; Hawrylak, P.; Klimov, V. I.; Rosenthal, S. J.; Hoogland, S.; Sargent, E. H. Continuous-wave lasing in colloidal quantum dot solids enabled by facet-selective epitaxy. *Nature* **2017,** *544*, 75-79.
(27) Yang, Z.; Pelton, M.; Fedin, I.; Talapin, D. V.; Waks, E. A room temperature continuous-wave nanolaser using colloidal quantum wells. *Nat Commun* **2017,** *8*, 143.
(28) Hu, H. W.; Salim, T.; Chen, B. B.; Lam, Y. M. Molecularly Engineered Organic-Inorganic Hybrid Perovskite with Multiple Quantum Well Structure for Multicolored Light-Emitting Diodes. *Scientific Reports* **2016,** *6*.

(29) Sum, T. C.; Righetto, M.; Lim, S. S. Quo vadis, perovskite emitters? *The Journal of Chemical Physics* **2020,** *152*, 130901.
(30) Tan, Z. K.; Moghaddam, R. S.; Lai, M. L.; Docampo, P.; Higler, R.; Deschler, F.; Price, M.; Sadhanala, A.; Pazos, L. M.; Credgington, D.; Hanusch, F.; Bein, T.; Snaith, H. J.; Friend, R. H. Bright light-emitting diodes based on organometal halide perovskite. *Nat. Nanotechnol.* **2014,** *9*, 687-92.
(31) Xu, W.; Hu, Q.; Bai, S.; Bao, C.; Miao, Y.; Yuan, Z.; Borzda, T.; Barker, A. J.; Tyukalova, E.; Hu, Z. Rational Molecular Passivation for High-Performance Perovskite Light-Emitting Diodes. *Nat. Photonics* **2019,** *13*, 418-424.
(32) Xing, G.; Wu, B.; Wu, X.; Li, M.; Du, B.; Wei, Q.; Guo, J.; Yeow, E. K.; Sum, T. C.; Huang, W. Transcending the Slow Bimolecular Recombination in Lead-Halide Perovskites for Electroluminescence. *Nat. Commun.* **2017,** *8*, 14558.
(33) Wang, N.; Cheng, L.; Ge, R.; Zhang, S.; Miao, Y.; Zou, W.; Yi, C.; Sun, Y.; Cao, Y.; Yang, R.; Wei, Y.; Guo, Q.; Ke, Y.; Yu, M.; Jin, Y.; Liu, Y.; Ding, Q.; Di, D.; Yang, L.; Xing, G.*; et al.* Perovskite light-emitting diodes based on solution-processed self-organized multiple quantum wells. *Nat. Photonics* **2016,** *10*, 699-704.
(34) Zou, W.; Li, R.; Zhang, S.; Liu, Y.; Wang, N.; Cao, Y.; Miao, Y.; Xu, M.; Guo, Q.; Di, D.; Zhang, L.; Yi, C.; Gao, F.; Friend, R. H.; Wang, J.; Huang, W. Minimising Efficiency Roll-Off in High-Brightness Perovskite Light-Emitting Diodes. *Nat. Commun.* **2018,** *9*, 608.
(35) Yang, M.; Wang, N.; Zhang, S.; Zou, W.; He, Y.; Wei, Y.; Xu, M.; Wang, J.; Huang, W. Reduced Efficiency Roll-Off and Enhanced Stability in Perovskite Light-Emitting Diodes with Multiple Quantum Wells. *J. Phys. Chem. Lett.* **2018,** *9*, 2038-2042.
(36) Yang, G.-L.; Zhong, H.-Z. J. C. C. L. Organometal halide perovskite quantum dots: synthesis, optical properties, and display applications. **2016,** *27*, 1124-1130.
(37) Li, X.; Wu, Y.; Zhang, S.; Cai, B.; Gu, Y.; Song, J.; Zeng, H. CsPbX3Quantum Dots for Lighting and Displays: Room-Temperature Synthesis, Photoluminescence Superiorities, Underlying Origins and White Light-Emitting Diodes. *Adv. Funct. Mater.* **2016,** *26*, 2435-2445.
(38) Song, J.; Fang, T.; Li, J.; Xu, L.; Zhang, F.; Han, B.; Shan, Q.; Zeng, H. Organic-Inorganic Hybrid Passivation Enables Perovskite QLEDs with an EQE of 16.48%. *Adv. Mater.* **2018,** *30*, 1805409.
(39) Swarnkar, A.; Marshall, A. R.; Sanehira, E. M.; Chernomordik, B. D.; Moore, D. T.; Christians, J. A.; Chakrabarti, T.; Luther, J. M. Quantum dot-induced phase stabilization of alpha-CsPbI3 perovskite for high-efficiency photovoltaics. *Science* **2016,** *354*, 92-95.
(40) Zhao, Q.; Hazarika, A.; Chen, X.; Harvey, S. P.; Larson, B. W.; Teeter, G. R.; Liu, J.; Song, T.; Xiao, C.; Shaw, L. J. N. c. High efficiency perovskite quantum dot solar cells with charge separating heterostructure. **2019,** *10*, 1-8.
(41) Li, J.; Xu, L.; Wang, T.; Song, J.; Chen, J.; Xue, J.; Dong, Y.; Cai, B.; Shan, Q.; Han, B.; Zeng, H. 50-Fold EQE Improvement up to 6.27% of Solution-Processed All-Inorganic Perovskite CsPbBr3 QLEDs via Surface Ligand Density Control. *Adv Mater* **2017,** *29*.
(42) Chiba, T.; Hayashi, Y.; Ebe, H.; Hoshi, K.; Sato, J.; Sato, S.; Pu, Y.-J.; Ohisa, S.; Kido, J. Anion-Exchange Red Perovskite Quantum Dots with Ammonium Iodine Salts for Highly Efficient Light-Emitting Devices. *Nat. Photonics* **2018,** *12*, 681-687.
(43) Zou, C.; Zheng, J.; Chang, C.; Majumdar, A.; Lin, L. Y. Nonvolatile Rewritable Photomemory Arrays Based on Reversible Phase-Change Perovskite for Optical Information Storage. *Adv. Opt. Mater.* **2019,** *7*, 1900558.

(44) Leyden, M. R.; Meng, L.; Jiang, Y.; Ono, L. K.; Qiu, L.; Juarez-Perez, E. J.; Qin, C.; Adachi, C.; Qi, Y. Methylammonium Lead Bromide Perovskite Light-Emitting Diodes by Chemical Vapor Deposition. *J Phys Chem Lett* **2017,** *8*, 3193-3198.
(45) Sutherland, B. R.; Hoogland, S.; Adachi, M. M.; Kanjanaboos, P.; Wong, C. T.; McDowell, J. J.; Xu, J.; Voznyy, O.; Ning, Z.; Houtepen, A. J.; Sargent, E. H. Perovskite thin films via atomic layer deposition. *Adv Mater* **2015,** *27*, 53-8.
(46) Park, M.-H.; Kim, J. S.; Heo, J.-M.; Ahn, S.; Jeong, S.-H.; Lee, T.-W. Boosting Efficiency in Polycrystalline Metal Halide Perovskite Light-Emitting Diodes. *ACS Energy Lett.* **2019,** *4*, 1134-1149.
(47) Xu, W.; Hu, Q.; Bai, S.; Bao, C.; Miao, Y.; Yuan, Z.; Borzda, T.; Barker, A. J.; Tyukalova, E.; Hu, Z.; Kawecki, M.; Wang, H.; Yan, Z.; Liu, X.; Shi, X.; Uvdal, K.; Fahlman, M.; Zhang, W.; Duchamp, M.; Liu, J.-M.*; et al.* Rational molecular passivation for high-performance perovskite light-emitting diodes. *Nat. Photonics* **2019,** *13*, 418-424.
(48) Liu, Q.-W.; Yuan, S.; Sun, S.-Q.; Luo, W.; Zhang, Y.-J.; Liao, L.-S.; Fung, M.-K. Interfacial Engineering for Highly Efficient Quasi-Two Dimensional Organic-Inorganic Hybrid Perovskite Light-Emitting Diodes. *J. Mater. Chem. C* **2019,** *7*, 4344-4349.
(49) Zou, Y.; Ban, M.; Yang, Y.; Bai, S.; Wu, C.; Han, Y.; Wu, T.; Tan, Y.; Huang, Q.; Gao, X.; Song, T.; Zhang, Q.; Sun, B. Boosting Perovskite Light-Emitting Diode Performance *via* Tailoring Interfacial Contact. *ACS Appl. Mater. Interfaces* **2018,** *10*, 24320-24326.
(50) Wang, J.; Wang, N.; Jin, Y.; Si, J.; Tan, Z. K.; Du, H.; Cheng, L.; Dai, X.; Bai, S.; He, H.; Ye, Z.; Lai, M. L.; Friend, R. H.; Huang, W. Interfacial control toward efficient and low-voltage perovskite light-emitting diodes. *Adv Mater* **2015,** *27*, 2311-6.
(51) Zhang, L.; Yang, X.; Jiang, Q.; Wang, P.; Yin, Z.; Zhang, X.; Tan, H.; Yang, Y. M.; Wei, M.; Sutherland, B. R.; Sargent, E. H.; You, J. Ultra-Bright and Highly Efficient Inorganic Based Perovskite Light-Emitting Diodes. *Nat. Commun.* **2017,** *8*, 15640.
(52) Lin, K.; Xing, J.; Quan, L. N.; de Arquer, F. P. G.; Gong, X.; Lu, J.; Xie, L.; Zhao, W.; Zhang, D.; Yan, C.; Li, W.; Liu, X.; Lu, Y.; Kirman, J.; Sargent, E. H.; Xiong, Q.; Wei, Z. Perovskite Light-Emitting Diodes with External Quantum Efficiency Exceeding 20 Per Cent. *Nature* **2018,** *562*, 245-248.
(53) Cao, Y.; Wang, N.; Tian, H.; Guo, J.; Wei, Y.; Chen, H.; Miao, Y.; Zou, W.; Pan, K.; He, Y.; Cao, H.; Ke, Y.; Xu, M.; Wang, Y.; Yang, M.; Du, K.; Fu, Z.; Kong, D.; Dai, D.; Jin, Y.*; et al.* Perovskite Light-Emitting Diodes Based on Spontaneously Formed Submicrometre-Scale Structures. *Nature* **2018,** *562*, 249-253.
(54) Shen, Y.; Cheng, L. P.; Li, Y. Q.; Li, W.; Chen, J. D.; Lee, S. T.; Tang, J. X. High-Efficiency Perovskite Light-Emitting Diodes with Synergetic Outcoupling Enhancement. *Adv Mater* **2019,** *31*, e1901517.
(55) You, J.; Meng, L.; Song, T. B.; Guo, T. F.; Yang, Y. M.; Chang, W. H.; Hong, Z.; Chen, H.; Zhou, H.; Chen, Q.; Liu, Y.; De Marco, N.; Yang, Y. Improved air stability of perovskite solar cells via solution-processed metal oxide transport layers. *Nat. Nanotechnol.* **2016,** *11*, 75-81.
(56) Yang, J.; Siempelkamp, B. D.; Mosconi, E.; De Angelis, F.; Kelly, T. L. Origin of the Thermal Instability in CH3NH3PbI3 Thin Films Deposited on ZnO. *Chemistry of Materials* **2015,** *27*, 4229-4236.
(57) Christians, J. A.; Miranda Herrera, P. A.; Kamat, P. V. Transformation of the excited state and photovoltaic efficiency of CH3NH3PbI3 perovskite upon controlled exposure to humidified air. *Journal of the American Chemical Society* **2015,** *137*, 1530-1538.

(58) Dong, Q.; Lei, L.; Mendes, J.; So, F. J. J. o. P. M. Operational stability of perovskite light emitting diodes. **2020,** *3*, 012002.
(59) Li, N.; Tao, S.; Chen, Y.; Niu, X.; Onwudinanti, C. K.; Hu, C.; Qiu, Z.; Xu, Z.; Zheng, G.; Wang, L.; Zhang, Y.; Li, L.; Liu, H.; Lun, Y.; Hong, J.; Wang, X.; Liu, Y.; Xie, H.; Gao, Y.; Bai, Y.*; et al.* Cation and anion immobilization through chemical bonding enhancement with fluorides for stable halide perovskite solar cells. *Nature Energy* **2019,** *4*, 408-415.
(60) Cegielski, P. J.; Giesecke, A. L.; Neutzner, S.; Porschatis, C.; Gandini, M.; Schall, D.; Perini, C. A. R.; Bolten, J.; Suckow, S.; Kataria, S.; Chmielak, B.; Wahlbrink, T.; Petrozza, A.; Lemme, M. C. Monolithically Integrated Perovskite Semiconductor Lasers on Silicon Photonic Chips by Scalable Top-Down Fabrication. *Nano Lett* **2018,** *18*, 6915-6923.
(61) Schlaus, A. P.; Spencer, M. S.; Miyata, K.; Liu, F.; Wang, X.; Datta, I.; Lipson, M.; Pan, A.; Zhu, X. Y. How lasing happens in CsPbBr3 perovskite nanowires. *Nat Commun* **2019,** *10*, 265.
(62) Zhu, H.; Fu, Y.; Meng, F.; Wu, X.; Gong, Z.; Ding, Q.; Gustafsson, M. V.; Trinh, M. T.; Jin, S.; Zhu, X. Y. Lead halide perovskite nanowire lasers with low lasing thresholds and high quality factors. *Nat Mater* **2015,** *14*, 636-42.
(63) Zhou, H.; Yuan, S.; Wang, X.; Xu, T.; Wang, X.; Li, H.; Zheng, W.; Fan, P.; Li, Y.; Sun, L.; Pan, A. Vapor growth and tunable lasing of band gap engineered cesium lead halide perovskite micro/nanorods with triangular cross section. *ACS Nano* **2017,** *11*, 1189-1195.
(64) Liu, Z.; Yang, J.; Du, J.; Hu, Z.; Shi, T.; Zhang, Z.; Liu, Y.; Tang, X.; Leng, Y.; Li, R. Robust Subwavelength Single-Mode Perovskite Nanocuboid Laser. *ACS Nano* **2018,** *12*, 5923-5931.
(65) Tang, B.; Dong, H.; Sun, L.; Zheng, W.; Wang, Q.; Sun, F.; Jiang, X.; Pan, A.; Zhang, L. Single-Mode Lasers Based on Cesium Lead Halide Perovskite Submicron Spheres. *ACS Nano* **2017,** *11*, 10681-10688.
(66) Liao, Q.; Hu, K.; Zhang, H.; Wang, X.; Yao, J.; Fu, H. Perovskite Microdisk Microlasers Self-Assembled from Solution. *Adv Mater* **2015,** *27*, 3405-10.
(67) Zhang, Q.; Ha, S. T.; Liu, X.; Sum, T. C.; Xiong, Q. Room-temperature near-infrared high-Q perovskite whispering-gallery planar nanolasers. *Nano Lett* **2014,** *14*, 5995-6001.
(68) Zhang, N.; Fan, Y.; Wang, K.; Gu, Z.; Wang, Y.; Ge, L.; Xiao, S.; Song, Q. All-optical control of lead halide perovskite microlasers. *Nat Commun* **2019,** *10*, 1770.
(69) Nguyen, V.-C.; Katsuki, H.; Sasaki, F.; Yanagi, H. Optically pumped lasing in single crystals of organometal halide perovskites prepared by cast-capping method. *Appl. Phys. Lett.* **2016,** *108*.
(70) Dong, H.; Zhang, C.; Liu, X.; Yao, J.; Zhao, Y. S. Materials chemistry and engineering in metal halide perovskite lasers. *Chem Soc Rev* **2020,** *49*, 951-982.
(71) Liu, P.; He, X.; Ren, J.; Liao, Q.; Yao, J.; Fu, H. Organic-Inorganic Hybrid Perovskite Nanowire Laser Arrays. *ACS Nano* **2017,** *11*, 5766-5773.
(72) He, X.; Liu, P.; Zhang, H.; Liao, Q.; Yao, J.; Fu, H. Patterning Multicolored Microdisk Laser Arrays of Cesium Lead Halide Perovskite. *Adv Mater* **2017,** *29*.
(73) Zhang, H.; Liao, Q.; Wu, Y.; Zhang, Z.; Gao, Q.; Liu, P.; Li, M.; Yao, J.; Fu, H. 2D Ruddlesden-Popper Perovskites Microring Laser Array. *Adv Mater* **2018,** *30*, e1706186.
(74) Zhizhchenko, A.; Syubaev, S.; Berestennikov, A.; Yulin, A. V.; Porfirev, A.; Pushkarev, A.; Shishkin, I.; Golokhvast, K.; Bogdanov, A. A.; Zakhidov, A. A.; Kuchmizhak, A. A.; Kivshar, Y. S.; Makarov, S. V. Single-Mode Lasing from Imprinted Halide-Perovskite Microdisks. *ACS Nano* **2019,** *13*, 4140-4147.

(75) Wang, S.; Liu, Y.; Li, G.; Zhang, J.; Zhang, N.; Xiao, S.; Song, Q. Lead Halide Perovskite Based Microdisk Lasers for On-Chip Integrated Photonic Circuits. *Adv. Opt. Mater.* **2018,** *6*.
(76) Deschler, F.; Price, M.; Pathak, S.; Klintberg, L. E.; Jarausch, D. D.; Higler, R.; Huttner, S.; Leijtens, T.; Stranks, S. D.; Snaith, H. J.; Atature, M.; Phillips, R. T.; Friend, R. H. High Photoluminescence Efficiency and Optically Pumped Lasing in Solution-Processed Mixed Halide Perovskite Semiconductors. *J Phys Chem Lett* **2014,** *5*, 1421-6.
(77) Chen, S.; Zhang, C.; Lee, J.; Han, J.; Nurmikko, A. High-Q, Low-Threshold Monolithic Perovskite Thin-Film Vertical-Cavity Lasers. *Adv Mater* **2017,** *29*.
(78) Chen, S.; Roh, K.; Lee, J.; Chong, W. K.; Lu, Y.; Mathews, N.; Sum, T. C.; Nurmikko, A. A Photonic Crystal Laser from Solution Based Organo-Lead Iodide Perovskite Thin Films. *ACS Nano* **2016,** *10*, 3959-67.
(79) Pourdavoud, N.; Wang, S.; Mayer, A.; Hu, T.; Chen, Y.; Marianovich, A.; Kowalsky, W.; Heiderhoff, R.; Scheer, H. C.; Riedl, T. Photonic Nanostructures Patterned by Thermal Nanoimprint Directly into Organo-Metal Halide Perovskites. *Adv. Mater.* **2017,** *29*, 1702902.
(80) Pourdavoud, N.; Haeger, T.; Mayer, A.; Cegielski, P. J.; Giesecke, A. L.; Heiderhoff, R.; Olthof, S.; Zaefferer, S.; Shutsko, I.; Henkel, A.; Becker-Koch, D.; Stein, M.; Cehovski, M.; Charfi, O.; Johannes, H. H.; Rogalla, D.; Lemme, M. C.; Koch, M.; Vaynzof, Y.; Meerholz, K.*; et al.* Room-Temperature Stimulated Emission and Lasing in Recrystallized Cesium Lead Bromide Perovskite Thin Films. *Adv Mater* **2019,** *31*, e1903717.
(81) Setoguchi, Y.; Adachi, C. Suppression of Roll-Off Characteristics of Electroluminescence at High Current Densities in Organic Light Emitting Diodes by Introducing Reduced Carrier Injection Barriers. *J. Appl. Phys.* **2010,** *108*, 064516.
(82) Razza, S.; Castro-Hermosa, S.; Di Carlo, A.; Brown, T. M. Research Update: Large-area deposition, coating, printing, and processing techniques for the upscaling of perovskite solar cell technology. *APL Mater.* **2016,** *4*, 091508.
(83) Swarnkar, A.; Marshall, A. R.; Sanehira, E. M.; Chernomordik, B. D.; Moore, D. T.; Christians, J. A.; Chakrabarti, T.; Luther, J. M. Quantum Dot-Induced Phase Stabilization of a-$CsPbI_3$ Perovskite for High-Efficiency Photovoltaics. *Science* **2016,** *354*, 92-95.
(84) Lin, Q.; Armin, A.; Burn, P. L.; Meredith, P. Filterless Narrowband Visible Photodetectors. *Nat. Photonics* **2015,** *9*, 687-694.
(85) Jin, Y.; Wang, Z. K.; Yuan, S.; Wang, Q.; Qin, C.; Wang, K. L.; Dong, C.; Li, M.; Liu, Y.; Liao, L. S. Synergistic Effect of Dual Ligands on Stable Blue Quasi-2D Perovskite Light-Emitting Diodes. *Adv. Funct. Mater.* **2020,** *30*, 1908339.
(86) Liu, Y.; Wu, T.; Liu, Y.; Song, T.; Sun, B. Suppression of Non-Radiative Recombination toward High Efficiency Perovskite Light-Emitting Diodes. *APL Mater.* **2019,** *7*, 021102.
(87) Zou, C.; Liu, Y.; Ginger, D. S.; Lin, L. Y. Suppressing Efficiency Roll-Off at High Current Densities for Ultra-Bright Green Perovskite Light-Emitting Diodes. *ACS Nano* **2020,** *14*, 6076-6086.
(88) Sim, K.; Jun, T.; Bang, J.; Kamioka, H.; Kim, J.; Hiramatsu, H.; Hosono, H. Performance Boosting Strategy for Perovskite Light-Emitting Diodes. *Appl. Phys. Rev.* **2019,** *6*, 031402.
(89) Huang, C.-Y.; Zou, C.; Mao, C.; Corp, K. L.; Yao, Y.-C.; Lee, Y.-J.; Schlenker, C. W.; Jen, A. K. Y.; Lin, L. Y. $CsPbBr_3$ Perovskite Quantum Dot Vertical Cavity Lasers with Low Threshold and High Stability. *ACS Photonics* **2017,** *4*, 2281-2289.

(90) Zhao, L.; Lee, K. M.; Roh, K.; Khan, S. U. Z.; Rand, B. P. Improved Outcoupling Efficiency and Stability of Perovskite Light-Emitting Diodes using Thin Emitting Layers. *Adv. Mater.* **2019,** *31*, 1805836.
(91) Shi, X.-B.; Liu, Y.; Yuan, Z.; Liu, X.-K.; Miao, Y.; Wang, J.; Lenk, S.; Reineke, S.; Gao, F. Optical Energy Losses in Organic-Inorganic Hybrid Perovskite Light-Emitting Diodes. *Adv. Opt. Mater.* **2018,** *6*, 1800667.
(92) Meng, S.-S.; Li, Y.-Q.; Tang, J.-X. Theoretical perspective to light outcoupling and management in perovskite light-emitting diodes. *Org. Electron.* **2018,** *61*, 351-358.
(93) Morgenstern, T.; Lampe, C.; Naujoks, T.; Jurow, M.; Liu, Y.; Urban, A. S.; Brütting, W. Elucidating the performance limits of perovskite nanocrystal light emitting diodes. *J. Lumin.* **2020,** *220*, 116939.
(94) Zhang, Q.; Tavakoli, M. M.; Gu, L.; Zhang, D.; Tang, L.; Gao, Y.; Guo, J.; Lin, Y.; Leung, S. F.; Poddar, S.; Fu, Y.; Fan, Z. Efficient metal halide perovskite light-emitting diodes with significantly improved light extraction on nanophotonic substrates. *Nat. Commun.* **2019,** *10*, 727.
(95) Shen, Y.; Cheng, L. P.; Li, Y. Q.; Li, W.; Chen, J. D.; Lee, S. T.; Tang, J. X. Perovskite Light-Emitting Diodes: High-Efficiency Perovskite Light-Emitting Diodes with Synergetic Outcoupling Enhancement. *Adv. Mater.* **2019,** *31*, 1970174.
(96) Jurow, M. J.; Morgenstern, T.; Eisler, C.; Kang, J.; Penzo, E.; Do, M.; Engelmayer, M.; Osowiecki, W. T.; Bekenstein, Y.; Tassone, C.; Wang, L. W.; Alivisatos, A. P.; Brutting, W.; Liu, Y. Manipulating the Transition Dipole Moment of CsPbBr3 Perovskite Nanocrystals for Superior Optical Properties. *Nano Lett.* **2019,** *19*, 2489-2496.
(97) Kim, S.-Y.; Jeong, W.-I.; Mayr, C.; Park, Y.-S.; Kim, K.-H.; Lee, J.-H.; Moon, C.-K.; Brütting, W.; Kim, J.-J. Organic Light-Emitting Diodes with 30% External Quantum Efficiency Based on a Horizontally Oriented Emitter. *Adv. Funct. Mater.* **2013,** *23*, 3896-3900.
(98) Zhu, R.; Luo, Z.; Wu, S. T. Light extraction analysis and enhancement in a quantum dot light emitting diode. *Opt. Express* **2014,** *22*, A1783-A1798.
(99) Fakharuddin, A.; Qiu, W.; Croes, G.; Devižis, A.; Gegevičius, R.; Vakhnin, A.; Rolin, C.; Genoe, J.; Gehlhaar, R.; Kadashchuk, A.; Gulbinas, V.; Heremans, P. Reduced Efficiency Roll-Off and Improved Stability of Mixed 2D/3D Perovskite Light Emitting Diodes by Balancing Charge Injection. *Adv. Funct. Mater.* **2019,** *29*, 1904101.
(100) Yang, X.; Zhang, X.; Deng, J.; Chu, Z.; Jiang, Q.; Meng, J.; Wang, P.; Zhang, L.; Yin, Z.; You, J. Efficient Green Light-Emitting Diodes Based on Quasi-Two-Dimensional Composition and Phase Engineered Perovskite with Surface Passivation. *Nat. Commun.* **2018,** *9*, 570.
(101) Chance, R. R.; Prock, A.; Silbey, R. Lifetime of an emitting molecule near a partially reflecting surface. *J. Chem. Phys.* **1974,** *60*, 2744-2748.
(102) Lu, M. H.; Sturm, J. C. External coupling efficiency in planar organic light-emitting devices. *Appl. Phys. Lett.* **2001,** *78*, 1927-1929.
(103) Brütting, W.; Frischeisen, J.; Schmidt, T. D.; Scholz, B. J.; Mayr, C. Device efficiency of organic light-emitting diodes: Progress by improved light outcoupling. *Phys. Status Solidi A* **2013,** *210*, 44-65.
(104) Schmidt, T. D.; Lampe, T.; Sylvinson M. R, D.; Djurovich, P. I.; Thompson, M. E.; Brütting, W. Emitter Orientation as a Key Parameter in Organic Light-Emitting Diodes. *Phys. Rev. Appl.* **2017,** *8*, 037001.

(105) Frischeisen, J.; Yokoyama, D.; Endo, A.; Adachi, C.; Brütting, W. Increased light outcoupling efficiency in dye-doped small molecule organic light-emitting diodes with horizontally oriented emitters. *Org. Electron.* **2011,** *12*, 809-817.
(106) Frischeisen, J.; Yokoyama, D.; Adachi, C.; Brütting, W. Determination of molecular dipole orientation in doped fluorescent organic thin films by photoluminescence measurements. *Appl. Phys. Lett.* **2010,** *96*, 29.
(107) van Mensfoort, S. L. M.; Carvelli, M.; Megens, M.; Wehenkel, D.; Bartyzel, M.; Greiner, H.; Janssen, R. A. J.; Coehoorn, R. Measuring the light emission profile in organic light-emitting diodes with nanometre spatial resolution. *Nat. Photonics* **2010,** *4*, 329-335.
(108) Jurow, M. J.; Lampe, T.; Penzo, E.; Kang, J.; Koc, M. A.; Zechel, T.; Nett, Z.; Brady, M.; Wang, L. W.; Alivisatos, A. P.; Cabrini, S.; Brutting, W.; Liu, Y. Tunable Anisotropic Photon Emission from Self-Organized CsPbBr3 Perovskite Nanocrystals. *Nano Lett.* **2017,** *17*, 4534-4540.
(109) Walters, G.; Haeberle, L.; Quintero-Bermudez, R.; Brodeur, J.; Kena-Cohen, S.; Sargent, E. H. Directional Light Emission from Layered Metal Halide Perovskite Crystals. *J. Phys. Chem. Lett.* **2020,** *11*, 3458-3465.
(110) Zhang, X.; Wu, G.; Fu, W.; Qin, M.; Yang, W.; Yan, J.; Zhang, Z.; Lu, X.; Chen, H. Orientation Regulation of Phenylethylammonium Cation Based 2D Perovskite Solar Cell with Efficiency Higher Than 11%. *Adv. Energy. Mater.* **2018,** *8*.
(111) Cho, C.; Zhao, B.; Tainter, G. D.; Lee, J. Y.; Friend, R. H.; Di, D.; Deschler, F.; Greenham, N. C. The role of photon recycling in perovskite light-emitting diodes. *Nat Commun* **2020,** *11*, 611.
(112) Kumawat, N. K.; Dey, A.; Narasimhan, K.; Kabra, D. Near infrared to visible electroluminescent diodes based on organometallic halide perovskites: structural and optical investigation. *ACS Photonics* **2015,** *2*, 349-354.
(113) Kim, Y. H.; Cho, H.; Heo, J. H.; Kim, T. S.; Myoung, N.; Lee, C. L.; Im, S. H.; Lee, T. W. Multicolored organic/inorganic hybrid perovskite light-emitting diodes. *Adv Mater* **2015,** *27*, 1248-54.
(114) Hoye, R. L.; Chua, M. R.; Musselman, K. P.; Li, G.; Lai, M. L.; Tan, Z. K.; Greenham, N. C.; MacManus-Driscoll, J. L.; Friend, R. H.; Credgington, D. Enhanced performance in fluorene-free organometal halide perovskite light-emitting diodes using tunable, low electron affinity oxide electron injectors. *Adv Mater* **2015,** *27*, 1414-9.
(115) Yu, J. C.; Kim, D. B.; Baek, G.; Lee, B. R.; Jung, E. D.; Lee, S.; Chu, J. H.; Lee, D. K.; Choi, K. J.; Cho, S.; Song, M. H. High-Performance Planar Perovskite Optoelectronic Devices: A Morphological and Interfacial Control by Polar Solvent Treatment. *Adv. Mater.* **2015,** *27*, 3492-500.
(116) Yantara, N.; Bhaumik, S.; Yan, F.; Sabba, D.; Dewi, H. A.; Mathews, N.; Boix, P. P.; Demir, H. V.; Mhaisalkar, S. Inorganic Halide Perovskites for Efficient Light-Emitting Diodes. *J. Phys. Chem. Lett.* **2015,** *6*, 4360-4.
(117) Ling, Y.; Tian, Y.; Wang, X.; Wang, J. C.; Knox, J. M.; Perez-Orive, F.; Du, Y.; Tan, L.; Hanson, K.; Ma, B.; Gao, H. Enhanced Optical and Electrical Properties of Polymer-Assisted All-Inorganic Perovskites for Light-Emitting Diodes. *Adv. Mater.* **2016,** *28*, 8983-8989.
(118) Swarnkar, A.; Marshall, A. R.; Sanehira, E. M.; Chernomordik, B. D.; Moore, D. T.; Christians, J. A.; Chakrabarti, T.; Luther, J. M. Quantum dot–induced phase stabilization of α-CsPbI3 perovskite for high-efficiency photovoltaics. *Science* **2016,** *354*, 92-95.

(119) Li, G.; Rivarola, F. W.; Davis, N. J.; Bai, S.; Jellicoe, T. C.; de la Pena, F.; Hou, S.; Ducati, C.; Gao, F.; Friend, R. H.; Greenham, N. C.; Tan, Z. K. Highly Efficient Perovskite Nanocrystal Light-Emitting Diodes Enabled by a Universal Crosslinking Method. *Adv. Mater.* **2016,** *28*, 3528-34.
(120) Zhang, X. L.; Xu, B.; Zhang, J. B.; Gao, Y.; Zheng, Y. J.; Wang, K.; Sun, X. W. All-Inorganic Perovskite Nanocrystals for High-Efficiency Light Emitting Diodes: Dual-Phase CsPbBr3-CsPb2Br5 Composites. *Adv. Funct. Mater.* **2016,** *26*, 4595-4600.
(121) Zhang, X.; Xu, B.; Wang, W.; Liu, S.; Zheng, Y.; Chen, S.; Wang, K.; Sun, X. W. Plasmonic Perovskite Light-Emitting Diodes Based on the Ag-CsPbBr3 System. *ACS Appl. Mater. Interfaces* **2017,** *9*, 4926-4931.
(122) Zhang, X.; Lin, H.; Huang, H.; Reckmeier, C.; Zhang, Y.; Choy, W. C.; Rogach, A. L. Enhancing the brightness of cesium lead halide perovskite nanocrystal based green light-emitting devices through the interface engineering with perfluorinated ionomer. *Nano Lett.* **2016,** *16*, 1415-1420.
(123) Wei, Z.; Perumal, A.; Su, R.; Sushant, S.; Xing, J.; Zhang, Q.; Tan, S. T.; Demir, H. V.; Xiong, Q. Solution-processed Highly Bright and Durable Cesium Lead Halide Perovskite Light-Emitting Diodes. *Nanoscale* **2016,** *8*, 18021-18026.
(124) Song, J.; Li, J.; Li, X.; Xu, L.; Dong, Y.; Zeng, H. Quantum Dot Light-Emitting Diodes Based on Inorganic Perovskite Cesium Lead Halides (CsPbX3). *Adv. Mater.* **2015,** *27*, 7162-7.
(125) Chiba, T.; Hoshi, K.; Pu, Y. J.; Takeda, Y.; Hayashi, Y.; Ohisa, S.; Kawata, S.; Kido, J. High-Efficiency Perovskite Quantum-Dot Light-Emitting Devices by Effective Washing Process and Interfacial Energy Level Alignment. *ACS Appl. Mater. Interfaces* **2017,** *9*, 18054-18060.
(126) Davis, N. J.; de la Pena, F. J.; Tabachnyk, M.; Richter, J. M.; Lamboll, R. D.; Booker, E. P.; Wisnivesky Rocca Rivarola, F.; Griffiths, J. T.; Ducati, C.; Menke, S. M.; Deschler, F.; Greenham, N. C. Photon Reabsorption in Mixed CsPbCl3:CsPbI3 Perovskite Nanocrystal Films for Light-Emitting Diodes. *J. Phys. Chem. C* **2017,** *121*, 3790-3796.
(127) Yassitepe, E.; Yang, Z.; Voznyy, O.; Kim, Y.; Walters, G.; Castañeda, J. A.; Kanjanaboos, P.; Yuan, M.; Gong, X.; Fan, F. Amine-Free Synthesis of Cesium Lead Halide Perovskite Quantum Dots for Efficient Light-Emitting Diodes. *Adv. Funct. Mater.* **2016,** *26*, 8757-8763.
(128) Li, Z.; Yang, M.; Park, J.-S.; Wei, S.-H.; Berry, J. J.; Zhu, K. Stabilizing perovskite structures by tuning tolerance factor: formation of formamidinium and cesium lead iodide solid-state alloys. *Chem. Mater.* **2015,** *28*, 284-292.
(129) Liu, X.; Hong, R.; Tian, C. Tolerance factor and the stability discussion of ABO3-type ilmenite. *J. Mater. Sci. Mater. Electron.* **2009,** *20*, 323.
(130) Protesescu, L.; Yakunin, S.; Kumar, S.; Bar, J.; Bertolotti, F.; Masciocchi, N.; Guagliardi, A.; Grotevent, M.; Shorubalko, I.; Bodnarchuk, M. I.; Shih, C. J.; Kovalenko, M. V. Dismantling the "Red Wall" of Colloidal Perovskites: Highly Luminescent Formamidinium and Formamidinium-Cesium Lead Iodide Nanocrystals. *ACS Nano* **2017,** *11*, 3119-3134.
(131) Li, J.; Xu, L.; Wang, T.; Song, J.; Chen, J.; Xue, J.; Dong, Y.; Cai, B.; Shan, Q.; Han, B.; Zeng, H. 50-Fold EQE Improvement up to 6.27% of Solution-Processed All-Inorganic Perovskite $CsPbBr_3$ QLEDs via Surface Ligand Density Control. *Adv. Mater.* **2017,** *29*, 1603885.
(132) Rose, A. Space-charge-limited currents in solids. *Phys. Rev.* **1955,** *97*, 1538.
(133) Dong, Q.; Fang, Y.; Shao, Y.; Mulligan, P.; Qiu, J.; Cao, L.; Huang, J. Electron-hole diffusion lengths> 175 μm in solution-grown CH3NH3PbI3 single crystals. *Science* **2015,** *347*, 967-970.

(134) Maculan, G.; Sheikh, A. D.; Abdelhady, A. L.; Saidaminov, M. I.; Haque, M. A.; Murali, B.; Alarousu, E.; Mohammed, O. F.; Wu, T.; Bakr, O. M. CH3NH3PbCl3 Single Crystals: Inverse Temperature Crystallization and Visible-Blind UV-Photodetector. *J. Phys. Chem. Lett.* **2015,** *6*, 3781-6.
(135) Chin, X. Y.; Cortecchia, D.; Yin, J.; Bruno, A.; Soci, C. Lead iodide perovskite light-emitting field-effect transistor. *Nat. Commun.* **2015,** *6*, 7383.
(136) Hetsch, F.; Zhao, N.; Kershaw, S. V.; Rogach, A. L. Quantum dot field effect transistors. *Mater. Today* **2013,** *16*, 312-325.
(137) Veldhuis, S. A.; Boix, P. P.; Yantara, N.; Li, M.; Sum, T. C.; Mathews, N.; Mhaisalkar, S. G. Perovskite Materials for Light-Emitting Diodes and Lasers. *Adv. Mater.* **2016,** *28*, 6804-34.
(138) Stoumpos, C. C.; Malliakas, C. D.; Kanatzidis, M. G. Semiconducting tin and lead iodide perovskites with organic cations: phase transitions, high mobilities, and near-infrared photoluminescent properties. *Inorg. Chem.* **2013,** *52*, 9019-38.
(139) Jaramillo-Quintero, O. A.; Sanchez, R. S.; Rincon, M.; Mora-Sero, I. Bright visible-infrared light emitting diodes based on hybrid halide perovskite with Spiro-OMeTAD as a hole-injecting layer. *The journal of physical chemistry letters* **2015,** *6*, 1883-1890.
(140) Liu, X.; Li, H.; Song, C.; Liao, Y.; Tian, M. Microcavity organic laser device under electrical pumping. *Opt. Lett.* **2009,** *34*, 503-5.
(141) Shi, Z.; Li, Y.; Zhang, Y.; Chen, Y.; Li, X.; Wu, D.; Xu, T.; Shan, C.; Du, G. High-Efficiency and Air-Stable Perovskite Quantum Dots Light-Emitting Diodes with an All-Inorganic Heterostructure. *Nano Lett.* **2017,** *17*, 313-321.
(142) Kim, T.-H.; Cho, K.-S.; Lee, E. K.; Lee, S. J.; Chae, J.; Kim, J. W.; Kim, D. H.; Kwon, J.-Y.; Amaratunga, G.; Lee, S. Y.; Choi, B. L.; Kuk, Y.; Kim, J. M.; Kim, K. Full-Colour Quantum Dot Displays Fabricated by Transfer Printing. *Nat. Photonics* **2011,** *5*, 176-182.
(143) Dai, X.; Deng, Y.; Peng, X.; Jin, Y. Quantum-Dot Light-Emitting Diodes for Large-Area Displays: Towards the Dawn of Commercialization. *Adv. Mater.* **2017,** *29*, 1607022.
(144) Wu, W.; Wang, X.; Han, X.; Yang, Z.; Gao, G.; Zhang, Y.; Hu, J.; Tan, Y.; Pan, A.; Pan, C. Flexible Photodetector Arrays Based on Patterned $CH_3NH_3PbI_{3-x}Cl_x$ Perovskite Film for Real-Time Photosensing and Imaging. *Adv. Mater.* **2019,** *31*, 1805913.
(145) Prins, F.; Kim, D. K.; Cui, J.; De Leo, E.; Spiegel, L. L.; McPeak, K. M.; Norris, D. J. Direct Patterning of Colloidal Quantum-Dot Thin Films for Enhanced and Spectrally Selective Out-Coupling of Emission. *Nano Lett.* **2017,** *17*, 1319-1325.
(146) Lee, E. K.; Park, C. H.; Lee, J.; Lee, H. R.; Yang, C.; Oh, J. H. Chemically Robust Ambipolar Organic Transistor Array Directly Patterned by Photolithography. *Adv. Mater.* **2017,** *29*, 1605282.
(147) Park, J.-S.; Kyhm, J.; Kim, H. H.; Jeong, S.; Kang, J.; Lee, S.-e.; Lee, K.-T.; Park, K.; Barange, N.; Han, J. Alternative Patterning Process for Realization of Large-Area, Full-Color, Active Quantum Dot Display. *Nano Lett.* **2016,** *16*, 6946-6953.
(148) Lin, S.; Tan, G.; Yu, J.; Chen, E.; Weng, Y.; Zhou, X.; Xu, S.; Ye, Y.; Yan, Q. F.; Guo, T. Multi-Primary-Color Quantum-Dot Down-Converting Films for Display Applications. *Optics Express* **2019,** *27*, 28480-28493.
(149) Kim, Y. H.; Cho, H.; Heo, J. H.; Kim, T. S.; Myoung, N.; Lee, C. L.; Im, S. H.; Lee, T. W. Multicolored Organic/Inorganic Hybrid Perovskite Light-Emitting Diodes. *Adv. Mater.* **2015,** *27*, 1248-1254.
(150) Yang, X.; Wu, J.; Liu, T.; Zhu, R. Patterned Perovskites for Optoelectronic Applications. *Small Methods* **2018,** *2*, 1800110.

(151) Lyashenko, D.; Perez, A.; Zakhidov, A. High-Resolution Patterning of Organohalide Lead Perovskite Pixels for Photodetectors Using Orthogonal Photolithography. *Phys. Status Solidi A* **2017,** *214*, 1600302.
(152) Liu, Y.; Li, F.; Qiu, L.; Yang, K.; Li, Q.; Zheng, X.; Hu, H.; Guo, T.; Wu, C.; Kim, T. W. Fluorescent Microarrays of in Situ Crystallized Perovskite Nanocomposites Fabricated for Patterned Applications by Using Inkjet Printing. *ACS Nano* **2019,** *13*, 2042-2049.
(153) Wong, Y. C.; Wu, W. B.; Wang, T.; Ng, J. A.; Khoo, K. H.; Wu, J.; Tan, Z. K. Color Patterning of Luminescent Perovskites via Light-Mediated Halide Exchange with Haloalkanes. *Adv. Mater.* **2019,** *31*, 1901247.
(154) Shi, L.; Meng, L.; Jiang, F.; Ge, Y.; Li, F.; Wu, X. g.; Zhong, H. In Situ Inkjet Printing Strategy for Fabricating Perovskite Quantum Dot Patterns. *Adv. Funct. Mater.* **2019,** *29*, 1903648.
(155) Gu, Z.; Wang, K.; Li, H.; Gao, M.; Li, L.; Kuang, M.; Zhao, Y. S.; Li, M.; Song, Y. Direct-Writing Multifunctional Perovskite Single Crystal Arrays by Inkjet Printing. *Small* **2017,** *13*, 1603217.
(156) Wang, H.; Haroldson, R.; Balachandran, B.; Zakhidov, A.; Sohal, S.; Chan, J. Y.; Zakhidov, A.; Hu, W. Nanoimprinted Perovskite Nanograting Photodetector with Improved Efficiency. *ACS Nano* **2016,** *10*, 10921-10928.
(157) Mao, J.; Sha, W. E. I.; Zhang, H.; Ren, X.; Zhuang, J.; Roy, V. A. L.; Wong, K. S.; Choy, W. C. H. Novel Direct Nanopatterning Approach to Fabricate Periodically Nanostructured Perovskite for Optoelectronic Applications. *Adv. Funct. Mater.* **2017,** *27*, 1606525.
(158) Brittman, S.; Oener, S. Z.; Guo, K.; Āboliņš, H.; Koenderink, A. F.; Garnett, E. C. Controlling Crystallization to Imprint Nanophotonic Structures into Halide Perovskites Using Soft Lithography. *J. Mater. Chem. C* **2017,** *5*, 8301-8307.
(159) Kamminga, M. E.; Fang, H. H.; Loi, M. A.; Ten Brink, G. H.; Blake, G. R.; Palstra, T. T. M.; Ten Elshof, J. E. Micropatterned 2D Hybrid Perovskite Thin Films with Enhanced Photoluminescence Lifetimes. *ACS Appl. Mater. Interfaces* **2018,** *10*, 12878-12885.
(160) Lee, W.; Lee, J.; Yun, H.; Kim, J.; Park, J.; Choi, C.; Kim, D. C.; Seo, H.; Lee, H.; Yu, J. W.; Lee, W. B.; Kim, D. H. High-Resolution Spin-on-Patterning of Perovskite Thin Films for a Multiplexed Image Sensor Array. *Adv. Mater.* **2017,** *29*, 1702902.
(161) Lin, C. H.; Zeng, Q.; Lafalce, E.; Yu, S.; Smith, M. J.; Yoon, Y. J.; Chang, Y.; Jiang, Y.; Lin, Z.; Vardeny, Z. V.; Tsukruk, V. V. Large-Area Lasing and Multicolor Perovskite Quantum Dot Patterns. *Adv. Opt. Mater.* **2018,** *6*, 1800474.
(162) Harwell, J.; Burch, J.; Fikouras, A.; Gather, M. C.; Di Falco, A.; Samuel, I. D. W. Patterning Multicolor Hybrid Perovskite Films *via* Top-Down Lithography. *ACS Nano* **2019,** *13*, 3823-3829.
(163) Ban, M.; Zou, Y.; Rivett, J. P. H.; Yang, Y.; Thomas, T. H.; Tan, Y.; Song, T.; Gao, X.; Credgington, D.; Deschler, F.; Sirringhaus, H.; Sun, B. Solution-Processed Perovskite Light Emitting Diodes with Efficiency Exceeding 15% through Additive-Controlled Nanostructure Tailoring. *Nat. Commun.* **2018,** *9*, 3892.
(164) DeFranco, J. A.; Schmidt, B. S.; Lipson, M.; Malliaras, G. G. Photolithographic Patterning of Organic Electronic Materials. *Org. Electron.* **2006,** *7*, 22-28.
(165) Sun, D.; Böhringer, K. F. EWOD-Aided Droplet Transport on Texture Ratchets. *Appl. Phys. Lett.* **2020,** *116*, 093702.
(166) Wang, Z.; Wang, F.; Sun, W.; Ni, R.; Hu, S.; Liu, J.; Zhang, B.; Alsaed, A.; Hayat, T.; Tan, Z. a. Manipulating the Trade-off Between Quantum Yield and Electrical Conductivity for

High-Brightness Quasi-2D Perovskite Light-Emitting Diodes. *Adv. Funct. Mater.* **2018,** *28*, 1804187.
(167) Li, Z.; Chen, Z.; Yang, Y.; Xue, Q.; Yip, H. L.; Cao, Y. Modulation of Recombination Zone Position for Quasi-Two-Dimensional Blue Perovskite Light-Emitting Diodes with Efficiency Exceeding 5%. *Nat. Commun.* **2019,** *10*, 1027.
(168) Liu, M.; Johnston, M. B.; Snaith, H. J. Efficient Planar Heterojunction Perovskite Solar Cells by Vapour Deposition. *Nature* **2013,** *501*, 395-398.
(169) Xing, G.; Mathews, N.; Sun, S.; Lim, S. S.; Lam, Y. M.; Grätzel, M.; Mhaisalkar, S.; Sum, T. C. Long-Range Balanced Electron- and Hole-Transport Lengths in Organic-Inorganic $CH_3NH_3PbI_3$. *Science* **2013,** *342*, 344-347.
(170) Zuo, F.; Williams, S. T.; Liang, P. W.; Chueh, C. C.; Liao, C. Y.; Jen, A. K. Y. Binary-Metal Perovskites Toward High-Performance Planar-Heterojunction Hybrid Solar Cells. *Adv. Mater.* **2014,** *26*, 6454-6460.
(171) Yang, W. S.; Noh, J. H.; Jeon, N. J.; Kim, Y. C.; Ryu, S.; Seo, J.; Seok, S. I. High-performance Photovoltaic Perovskite Layers Fabricated through Intramolecular Exchange. *Science* **2015,** *348*, 1234-1237.
(172) Ponseca, C. S.; Savenije, T. J.; Abdellah, M.; Zheng, K.; Yartsev, A.; Pascher, T.; Harlang, T.; Chabera, P.; Pullerits, T.; Stepanov, A.; Wolf, J.-P.; Sundström, V. Organometal Halide Perovskite Solar Cell Materials Rationalized: Ultrafast Charge Generation, High and Microsecond-Long Balanced Mobilities, and Slow Recombination. *JACS* **2014,** *136*, 5189-5192.
(173) De Wolf, S.; Holovsky, J.; Moon, S.-J.; Löper, P.; Niesen, B.; Ledinsky, M.; Haug, F.-J.; Yum, J.-H.; Ballif, C. Organometallic Halide Perovskites: Sharp Optical Absorption Edge and Its Relation to Photovoltaic Performance. *The Journal of Physical Chemistry Letters* **2014,** *5*, 1035-1039.
(174) Yin, W.-J.; Shi, T.; Yan, Y. Unusual Defect Physics in $CH_3NH_3PbI_3$ Perovskite Solar Cell Absorber. *Appl. Phys. Lett.* **2014,** *104*, 063903.
(175) Stranks, S. D.; Snaith, H. J. Metal-halide Perovskites for Photovoltaic and Light-emitting Devices. *Nature Nanotechnology* **2015,** *10*, 391-402.
(176) Colella, S.; Mazzeo, M.; Rizzo, A.; Gigli, G.; Listorti, A. The Bright Side of Perovskites. *The Journal of Physical Chemistry Letters* **2016,** *7*, 4322-4334.
(177) Tan, Z.-K.; Moghaddam, R. S.; Lai, M. L.; Docampo, P.; Higler, R.; Deschler, F.; Price, M.; Sadhanala, A.; Pazos, L. M.; Credgington, D.; Hanusch, F.; Bein, T.; Snaith, H. J.; Friend, R. H. Bright Light-emitting Diodes Based on Organometal Halide Perovskite. *Nature Nanotechnology* **2014,** *9*, 687-692.
(178) Cho, H.; Jeong, S.-H.; Park, M.-H.; Kim, Y.-H.; Wolf, C.; Lee, C.-L.; Heo, J. H.; Sadhanala, A.; Myoung, N.; Yoo, S. Overcoming the Electroluminescence Efficiency Limitations of Perovskite Light-Emitting Diodes. *Science* **2015,** *350*, 1222-1225.
(179) Pan, J.; Sarmah, S. P.; Murali, B.; Dursun, I.; Peng, W.; Parida, M. R.; Liu, J.; Sinatra, L.; Alyami, N.; Zhao, C. Air-stable Surface-passivated Perovskite Quantum Dots for Ultra-robust, Single-and Two-photon-induced Amplified Spontaneous Emission. *The journal of physical chemistry letters* **2015,** *6*, 5027-5033.
(180) Stranks, S. D.; Wood, S. M.; Wojciechowski, K.; Deschler, F.; Saliba, M.; Khandelwal, H.; Patel, J. B.; Elston, S. J.; Herz, L. M.; Johnston, M. B. Enhanced Amplified Spontaneous Emission in Perovskites Using a Flexible Cholesteric Liquid Crystal Reflector. *Nano Lett.* **2015,** *15*, 4935-4941.

(181) Yakunin, S.; Protesescu, L.; Krieg, F.; Bodnarchuk, M. I.; Nedelcu, G.; Humer, M.; De Luca, G.; Fiebig, M.; Heiss, W.; Kovalenko, M. V. Low-threshold Amplified Spontaneous Emission and Lasing from Colloidal Nanocrystals of Caesium Lead Halide Perovskites. *Nature Communications* **2015,** *6*, 8056.
(182) Liu, X.; Ha, S. T.; Zhang, Q.; de la Mata, M.; Magen, C.; Arbiol, J.; Sum, T. C.; Xiong, Q. Whispering Gallery Mode Lasing from Hexagonal Shaped Layered Lead Iodide Crystals. *ACS Nano* **2015,** *9*, 687-695.
(183) Xing, G.; Mathews, N.; Lim, S. S.; Yantara, N.; Liu, X.; Sabba, D.; Grätzel, M.; Mhaisalkar, S.; Sum, T. C. Low-temperature Solution-processed Wavelength-tunable Perovskites for Lasing. *Nature materials* **2014,** *13*, 476-480.
(184) Deschler, F.; Price, M.; Pathak, S.; Klintberg, L. E.; Jarausch, D.-D.; Higler, R.; Hüttner, S.; Leijtens, T.; Stranks, S. D.; Snaith, H. J.; Atatüre, M.; Phillips, R. T.; Friend, R. H. High Photoluminescence Efficiency and Optically Pumped Lasing in Solution-Processed Mixed Halide Perovskite Semiconductors. *The Journal of Physical Chemistry Letters* **2014,** *5*, 1421-1426.
(185) Shi, Z.-F.; Sun, X.-G.; Wu, D.; Xu, T.-T.; Tian, Y.-T.; Zhang, Y.-T.; Li, X.-J.; Du, G.-T. Near-infrared Random Lasing Realized in a Perovskite $CH_3NH_3PbI_3$ thin film. *Journal of Materials Chemistry C* **2016,** *4*, 8373-8379.
(186) Zhu, H.; Fu, Y.; Meng, F.; Wu, X.; Gong, Z.; Ding, Q.; Gustafsson, M. V.; Trinh, M. T.; Jin, S.; Zhu, X. Lead Halide Perovskite Nanowire Lasers with Low Lasing Thresholds and High Quality Factors. *Nature Materials* **2015,** *14*, 636-642.
(187) Niu, G.; Guo, X.; Wang, L. Review of Recent Progress in Chemical Stability of Perovskite Solar Cells. *Journal of Materials Chemistry A* **2015,** *3*, 8970-8980.
(188) Rong, Y.; Liu, L.; Mei, A.; Li, X.; Han, H. Beyond Efficiency: The Challenge of Stability in Mesoscopic Perovskite Solar Cells. *Advanced Energy Materials* **2015,** *5*, 1501066.
(189) Yang, Z.; Rajagopal, A.; Jo, S. B.; Chueh, C.-C.; Williams, S.; Huang, C.-C.; Katahara, J. K.; Hillhouse, H. W.; Jen, A. K.-Y. Stabilized Wide Bandgap Perovskite Solar Cells by Tin Substitution. *Nano Lett.* **2016,** *16*, 7739-7747.
(190) Sanehira, E. M.; Tremolet de Villers, B. J.; Schulz, P.; Reese, M. O.; Ferrere, S.; Zhu, K.; Lin, L. Y.; Berry, J. J.; Luther, J. M. Influence of Electrode Interfaces on the Stability of Perovskite Solar Cells: Reduced Degradation Using MoO_x/Al for Hole Collection. *ACS Energy Letters* **2016,** *1*, 38-45.
(191) Song, J.; Li, J.; Li, X.; Xu, L.; Dong, Y.; Zeng, H. Quantum Dot Light-Emitting Diodes Based on Inorganic Perovskite Cesium Lead Halides ($CsPbX_3$). *Adv. Mater.* **2015,** *27*, 7162-7167.
(192) Wang, Y.; Li, X.; Song, J.; Xiao, L.; Zeng, H.; Sun, H. All-Inorganic Colloidal Perovskite Quantum Dots: A New Class of Lasing Materials with Favorable Characteristics. *Adv. Mater.* **2015,** *27*, 7101-7108.
(193) Zhang, X.; Lin, H.; Huang, H.; Reckmeier, C.; Zhang, Y.; Choy, W. C.; Rogach, A. L. Enhancing the Brightness of Cesium Lead Halide Perovskite Nanocrystal Based Green Light-Emitting Devices through the Interface Engineering with Perfluorinated Ionomer. *Nano Lett.* **2016,** *16*, 1415-1420.
(194) Ling, Y.; Tian, Y.; Wang, X.; Wang, J. C.; Knox, J. M.; Perez-Orive, F.; Du, Y.; Tan, L.; Hanson, K.; Ma, B. Enhanced Optical and Electrical Properties of Polymer-Assisted All-Inorganic Perovskites for Light-Emitting Diodes. *Adv. Mater.* **2016,** *28*, 8983-8989.

(195) Eaton, S. W.; Lai, M.; Gibson, N. A.; Wong, A. B.; Dou, L.; Ma, J.; Wang, L.-W.; Leone, S. R.; Yang, P. Lasing in Robust Cesium Lead Halide Perovskite Nanowires. *Proceedings of the National Academy of Sciences* **2016,** *113*, 1993-1998.
(196) Xu, Y.; Chen, Q.; Zhang, C.; Wang, R.; Wu, H.; Zhang, X.; Xing, G.; Yu, W. W.; Wang, X.; Zhang, Y. Two-photon-pumped Perovskite Semiconductor Nanocrystal Lasers. *J. Am. Chem. Soc.* **2016,** *138*, 3761-3768.
(197) Wang, Y.; Li, X.; Nalla, V.; Zeng, H.; Sun, H. Solution-Processed Low Threshold Vertical Cavity Surface Emitting Lasers from All-Inorganic Perovskite Nanocrystals. *Adv. Funct. Mater.* **2017,** *27*, 1605088.
(198) Chang-Hasnain, C. J. Tunable VCSEL. *IEEE Journal of Selected Topics in Quantum Electronics* **2000,** *6*, 978-987.
(199) Lidzey, D. G.; Bradley, D.; Skolnick, M.; Virgili, T.; Walker, S.; Whittaker, D. Strong Exciton–Photon Coupling in an Organic Semiconductor Microcavity. *Nature* **1998,** *395*, 53-55.
(200) Tessler, N.; Denton, G. J.; Friend, R. H. Lasing from Conjugated-Polymer Microcavities. *Nature* **1996,** *382*, 695.
(201) Dang, C.; Lee, J.; Breen, C.; Steckel, J. S.; Coe-Sullivan, S.; Nurmikko, A. Red, Green and Blue Lasing Enabled by Single-Exciton Gain in Colloidal Quantum Dot Films. *Nat Nano* **2012,** *7*, 335-339.
(202) Weng, G.; Mei, Y.; Liu, J.; Hofmann, W.; Ying, L.; Zhang, J.; Bu, Y.; Li, Z.; Yang, H.; Zhang, B. Low Threshold Continuous-Wave Lasing of Yellow-Green InGaN-QD Vertical-Cavity Surface-Emitting Lasers. *Opt. Express* **2016,** *24*, 15546-15553.
(203) Dang, C.; Lee, J.; Breen, C.; Steckel, J. S.; Coe-Sullivan, S.; Nurmikko, A. Red, green and blue lasing enabled by single-exciton gain in colloidal quantum dot films. *Nat. Nanotechnol.* **2012,** *7*, 335-9.
(204) Chen, S.; Zhang, C.; Lee, J.; Han, J.; Nurmikko, A. High-Q, Low-Threshold Monolithic Perovskite Thin-Film Vertical-Cavity Lasers. *Adv. Mater.* **2017**, 1604781.
(205) Boles, M. A.; Ling, D.; Hyeon, T.; Talapin, D. V. The Surface Science of Nanocrystals. *Nature Materials* **2016,** *15*, 141-153.
(206) Cadelano, M.; Sarritzu, V.; Sestu, N.; Marongiu, D.; Chen, F.; Piras, R.; Corpino, R.; Carbonaro, C. M.; Quochi, F.; Saba, M. Can Trihalide Lead Perovskites Support Continuous Wave Lasing? *Advanced Optical Materials* **2015,** *3*, 1557-1564.
(207) Milot, R. L.; Eperon, G. E.; Snaith, H. J.; Johnston, M. B.; Herz, L. M. Temperature-Dependent Charge-Carrier Dynamics in $CH_3NH_3PbI_3$ Perovskite Thin Films. *Adv. Funct. Mater.* **2015,** *25*, 6218-6227.
(208) Lu, M.; Zhang, Y.; Wang, S.; Guo, J.; Yu, W. W.; Rogach, A. L. Metal Halide Perovskite Light-Emitting Devices: Promising Technology for Next-Generation Displays. *Adv. Funct. Mater.* **2019,** *29*, 1902008.
(209) Xing, J.; Zhao, Y.; Askerka, M.; Quan, L. N.; Gong, X.; Zhao, W.; Zhao, J.; Tan, H.; Long, G.; Gao, L.; Yang, Z.; Voznyy, O.; Tang, J.; Lu, Z. H.; Xiong, Q.; Sargent, E. H. Color-Stable Highly Luminescent Sky-Blue Perovskite Light-Emitting Diodes. *Nat. Commun.* **2018,** *9*, 3541.
(210) Shang, Y.; Li, G.; Liu, W.; Ning, Z. Quasi-2D Inorganic CsPbBr3 Perovskite for Efficient and Stable Light-Emitting Diodes. *Adv. Funct. Mater.* **2018,** *28*, 1801193.
(211) Han, B.; Cai, B.; Shan, Q.; Song, J.; Li, J.; Zhang, F.; Chen, J.; Fang, T.; Ji, Q.; Xu, X. Stable, Efficient Red Perovskite Light-Emitting Diodes by (a, d)-$CsPbI_3$ Phase Engineering. *Adv. Funct. Mater.* **2018,** *28*, 1804285.

(212) Leyden, M. R.; Terakawa, S.; Matsushima, T.; Ruan, S.; Goushi, K.; Auffray, M.; Sandanayaka, A. S. D.; Qin, C.; Bencheikh, F.; Adachi, C. Distributed Feedback Lasers and Light-Emitting Diodes Using 1-Naphthylmethylamnonium Low-Dimensional Perovskite. *ACS Photonics* **2019,** *6*, 460-466.
(213) Murawski, C.; Leo, K.; Gather, M. C. Efficiency Roll-Off in Organic Light-Emitting Diodes. *Adv. Mater.* **2013,** *25*, 6801-6827.
(214) Shirasaki, Y.; Supran, G. J.; Tisdale, W. A.; Bulovic, V. Origin of Efficiency Roll-Off in Colloidal Quantum-Dot Light-Emitting Diodes. *Phys. Rev. Lett.* **2013,** *110*, 217403.
(215) Sun, Y.; Su, Q.; Zhang, H.; Wang, F.; Zhang, S.; Chen, S. Investigation on Thermally Induced Efficiency Roll-Off: Toward Efficient and Ultrabright Quantum-Dot Light-Emitting Diodes. *ACS Nano* **2019,** *13*, 11433-11442.
(216) Nakanotani, H.; Oyamada, T.; Kawamura, Y.; Sasabe, H.; Adachi, C. Injection and Transport of High Current Density over 1000 A/cm^2 in Organic Light Emitting Diodes under Pulse Excitation. *Jpn. J. Appl. Phys.* **2005,** *44*, 3659-3662.
(217) Giuri, A.; Yuan, Z.; Miao, Y.; Wang, J.; Gao, F.; Sestu, N.; Saba, M.; Bongiovanni, G.; Colella, S.; Esposito Corcione, C.; Gigli, G.; Listorti, A.; Rizzo, A. Ultra-Bright Near-Infrared Perovskite Light-Emitting Diodes with Reduced Efficiency Roll-off. *Sci. Rep.* **2018,** *8*, 15496.
(218) Kim, H.; Zhao, L.; Price, J. S.; Grede, A. J.; Roh, K.; Brigeman, A. N.; Lopez, M.; Rand, B. P.; Giebink, N. C. Hybrid Perovskite Light Emitting Diodes under Intense Electrical Excitation. *Nat. Commun.* **2018,** *9*, 4893.
(219) Wang, Y.; Teng, Y.; Lu, P.; Shen, X.; Jia, P.; Lu, M.; Shi, Z.; Dong, B.; Yu, W. W.; Zhang, Y. Low Roll-Off Perovskite Quantum Dot Light-Emitting Diodes Achieved by Augmenting Hole Mobility. *Adv. Funct. Mater.* **2020**, 1910140.
(220) DeQuilettes, D. W.; Koch, S.; Burke, S.; Paranji, R. K.; Shropshire, A. J.; Ziffer, M. E.; Ginger, D. S. Photoluminescence Lifetimes Exceeding 8 μs and Quantum Yields Exceeding 30% in Hybrid Perovskite Thin Films by Ligand Passivation. *ACS Energy Lett.* **2016,** *1*, 438-444.
(221) Byun, J.; Cho, H.; Wolf, C.; Jang, M.; Sadhanala, A.; Friend, R. H.; Yang, H.; Lee, T. W. Efficient Visible Quasi-2D Perovskite Light-Emitting Diodes. *Adv. Mater.* **2016,** *28*, 7515-20.
(222) Liu, Y.; Cui, J.; Du, K.; Tian, H.; He, Z.; Zhou, Q.; Yang, Z.; Deng, Y.; Chen, D.; Zuo, X.; Ren, Y.; Wang, L.; Zhu, H.; Zhao, B.; Di, D.; Wang, J.; Friend, R. H.; Jin, Y. Efficient Blue Light-Emitting Diodes Based on Quantum-Confined Bromide Perovskite Nanostructures. *Nat. Photonics* **2019,** *13*, 760-764.
(223) Straus, D. B.; Kagan, C. R. Electrons, Excitons, and Phonons in Two-Dimensional Hybrid Perovskites: Connecting Structural, Optical, and Electronic Properties. *J. Phys. Chem. Lett.* **2018,** *9*, 1434-1447.
(224) Kirkwood, N.; Singh, B.; Mulvaney, P. Enhancing Quantum Dot LED Efficiency by Tuning Electron Mobility in the ZnO Electron Transport Layer. *Adv. Mater. Interfaces* **2016,** *3*, 1600868.
(225) Straus, D. B.; Iotov, N.; Gau, M. R.; Zhao, Q.; Carroll, P. J.; Kagan, C. R. Longer Cations Increase Energetic Disorder in Excitonic 2D Hybrid Perovskites. *J. Phys. Chem. Lett.* **2019,** *10*, 1198-1205.
(226) Milot, R. L.; Eperon, G. E.; Green, T.; Snaith, H. J.; Johnston, M. B.; Herz, L. M. Radiative Monomolecular Recombination Boosts Amplified Spontaneous Emission in $HC(NH2)_2SnI_3$ Perovskite Films. *J. Phys. Chem. Lett.* **2016,** *7*, 4178-4184.
(227) Richter, J. M.; Abdi-Jalebi, M.; Sadhanala, A.; Tabachnyk, M.; Rivett, J. P. H.; Pazos-Outon, L. M.; Godel, K. C.; Price, M.; Deschler, F.; Friend, R. H. Enhancing Photoluminescence

Yields in Lead Halide Perovskites by Photon Recycling and Light Out-Coupling. *Nat. Commun.* **2016,** *7*, 13941.
(228) Cho, H.; Kim, Y. H.; Wolf, C.; Lee, H. D.; Lee, T. W. Improving the Stability of Metal Halide Perovskite Materials and Light-Emitting Diodes. *Adv. Mater.* **2018,** *30*, 1704587.
(229) Lee, H.; Ko, D.; Lee, C. Direct Evidence of Ion-Migration-Induced Degradation of Ultrabright Perovskite Light-Emitting Diodes. *ACS Appl. Mater. Interfaces* **2019,** *11*, 11667-11673.
(230) Zou, C.; Huang, C. Y.; Sanehira, E. M.; Luther, J. M.; Lin, L. Y. Highly Stable Cesium Lead Iodide Perovskite Quantum Dot Light-Emitting Diodes. *Nanotechnology* **2017,** *28*, 455201.
(231) Chen, Z.; Li, Z.; Zhang, C.; Jiang, X. F.; Chen, D.; Xue, Q.; Liu, M.; Su, S.; Yip, H. L.; Cao, Y. Recombination Dynamics Study on Nanostructured Perovskite Light-Emitting Devices. *Adv. Mater.* **2018,** *30*, 1801370.
(232) deQuilettes, D. W.; Frohna, K.; Emin, D.; Kirchartz, T.; Bulovic, V.; Ginger, D. S.; Stranks, S. D. Charge-Carrier Recombination in Halide Perovskites: Focus Review. *Chem. Rev.* **2019,** *119*, 11007-11019.
(233) Li, J.; Yuan, X.; Jing, P.; Li, J.; Wei, M.; Hua, J.; Zhao, J.; Tian, L. Temperature-Dependent Photoluminescence of Inorganic Perovskite Nanocrystal Films. *RSC Adv.* **2016,** *6*, 78311-78316.
(234) Koh, T.-W.; Spechler, J. A.; Lee, K. M.; Arnold, C. B.; Rand, B. P. Enhanced Outcoupling in Organic Light-Emitting Diodes *via* a High-Index Contrast Scattering Layer. *ACS Photonics* **2015,** *2*, 1366-1372.
(235) Lim, J.; Park, Y. S.; Klimov, V. I. Optical Gain in Colloidal Quantum Dots Achieved with Direct-Current Electrical Pumping. *Nat. Mater.* **2018,** *17*, 42-49.
(236) Matsushima, T.; Sasabe, H.; Adachi, C. Carrier Injection and Transport Characteristics of Copper Phthalocyanine Thin Films under Low to Extremely High Current Densities. *Appl. Phys. Lett.* **2006,** *88*, 033508.
(237) Xu, M.; Peng, Q.; Zou, W.; Gu, L.; Xu, L.; Cheng, L.; He, Y.; Yang, M.; Wang, N.; Huang, W.; Wang, J. A Transient-Electroluminescence Study on Perovskite Light-Emitting Diodes. *Appl. Phys. Lett.* **2019,** *115*, 041102.
(238) Hayashi, K.; Nakanotani, H.; Inoue, M.; Yoshida, K.; Mikhnenko, O.; Nguyen, T.-Q.; Adachi, C. Suppression of Roll-Off Characteristics of Organic Light-Emitting Diodes by Narrowing Current Injection/Transport Area to 50 nm. *Appl. Phys. Lett.* **2015,** *106*, 093301.
(239) Kuwae, H.; Nitta, A.; Yoshida, K.; Kasahara, T.; Matsushima, T.; Inoue, M.; Shoji, S.; Mizuno, J.; Adachi, C. Suppression of External Quantum Efficiency Roll-Off of Nanopatterned Organic-Light Emitting Diodes at High Current Densities. *J. Appl. Phys.* **2015,** *118*, 155501.
(240) Chiba, T.; Hoshi, K.; Pu, Y.-J.; Takeda, Y.; Hayashi, Y.; Ohisa, S.; Kawata, S.; Kido, J. High-Efficiency Perovskite Quantum-Dot Light-Emitting Devices by Effective Washing Process and Interfacial Energy Level Alignment. *ACS Appl. Mater. Interfaces* **2017,** *9*, 18054-18060.
(241) Chen, H.; Fan, L.; Zhang, R.; Liu, W.; Zhang, Q.; Guo, R.; Zhuang, S.; Wang, L. Sodium Ion Modifying *In Situ* Fabricated $CsPbBr_3$ Nanoparticles for Efficient Perovskite Light Emitting Diodes. *Adv. Opt. Mater.* **2019,** *7*, 1900747.
(242) Shi, Z.; Li, Y.; Li, S.; Li, X.; Wu, D.; Xu, T.; Tian, Y.; Chen, Y.; Zhang, Y.; Zhang, B. Localized Surface Plasmon Enhanced All-Inorganic Perovskite Quantum Dot Light-Emitting Diodes Based on Coaxial Core/Shell Heterojunction Architecture. *Adv. Funct. Mater.* **2018,** *28*, 1707031.

(243) Lin, K.; Xing, J.; Quan, L. N.; de Arquer, F. P. G.; Gong, X.; Lu, J.; Xie, L.; Zhao, W.; Zhang, D.; Yan, C. Perovskite Light-Emitting Diodes with External Quantum Efficiency Exceeding 20 Per Cent. *Nature* **2018,** *562*, 245-248.
(244) Wang, Z.; Luo, Z.; Zhao, C.; Guo, Q.; Wang, Y.; Wang, F.; Bian, X.; Alsaedi, A.; Hayat, T.; Tan, Z. a. Efficient and Stable Pure Green All-Inorganic Perovskite CsPbBr3 Light-Emitting Diodes with a Solution-Processed NiOx Interlayer. *J. Phys. Chem. C* **2017,** *121*, 28132-28138.
(245) Wang, Z.; Wang, F.; Sun, W.; Ni, R.; Hu, S.; Liu, J.; Zhang, B.; Alsaed, A.; Hayat, T.; Tan, Z. a. Manipulating the Trade-Off between Quantum Yield and Electrical Conductivity for High-Brightness Quasi-2D Perovskite Light-Emitting Diodes. *Adv. Funct. Mater.* **2018,** *28*, 1804187.
(246) Wu, C.; Zou, Y.; Wu, T.; Ban, M.; Pecunia, V.; Han, Y.; Liu, Q.; Song, T.; Duhm, S.; Sun, B. Improved Performance and Stability of All-Inorganic Perovskite Light-Emitting Diodes by Antisolvent Vapor Treatment. *Adv. Funct. Mater.* **2017,** *27*, 1700338.
(247) Ling, Y.; Tian, Y.; Wang, X.; Wang, J. C.; Knox, J. M.; Perez-Orive, F.; Du, Y.; Tan, L.; Hanson, K.; Ma, B. Enhanced Optical and Electrical Properties of Polymer-Assisted All-Inorganic Perovskites for Light-Emitting Diodes. *Adv. Mater.* **2016,** *28*, 8983-8989.
(248) Zhang, L.; Yang, X.; Jiang, Q.; Wang, P.; Yin, Z.; Zhang, X.; Tan, H.; Yang, Y. M.; Wei, M.; Sutherland, B. R.; Sargent, E. H.; You, J. Ultra-Bright and Highly Efficient Inorganic Based Perovskite Light-Emitting Diodes. *Nat. Commun.* **2017,** *8*, 15640.
(249) Gather, M. C. Continuous lasing for perovskites. *Nat. Photonics* **2017,** *11*, 745-747.
(250) Sandanayaka, A. S. D.; Matsushima, T.; Bencheikh, F.; Terakawa, S.; Potscavage, W. J.; Qin, C.; Fujihara, T.; Goushi, K.; Ribierre, J.-C.; Adachi, C. Indication of current-injection lasing from an organic semiconductor. *Applied Physics Express* **2019,** *12*.

VITA

Chen was born in Jiangxi province, China. He received bachelor's degree from Zhejiang University in 2011. His undergraduate major is Optical Engineering, starting from that, he became enthusiastic about optoelectronic devices. Besides the study in his major, Chen also participated in advanced honor class of engineering education in Chukochen Honors college. In September 2015, Chen started to pursue a Ph.D. in Electrical and Computer Engineering at the University of Washington under the supervisory of Prof. Lih Y. Lin. His research interests are very broad, covering from circuit design, photodetectors, transistors, memories, LEDs and lasers, during his Ph.D. career. His research focus is on perovskite light-emitting devices, which serves as the basis of his dissertation research. Chen was awarded clean energy fellowship at University of Washington in 2017, outstanding reviewer of Nanotechnology in 2018. After receiving his Ph.D. degree, Chen will join Prof. Osman Bakr's group as a postdoc at KAUST in Saudi Arabia. He will be continuing his research on high-performance perovskite light-emitting diodes and electrically pumped perovskite lasers.